Blended VIIRS and AMSR2 Sea Ice Concentration

Richard Dworak[1] (rdworak@ssec.wisc.edu), Yinghui Liu[2], and Jeffrey R. Key[2]

[1]Cooperative Institute for Meteorological Satellite Studies, University of Wisconsin–Madison

[2]NOAA/NESDIS Advanced Satellite Products Branch, Madison, WI

Introduction

This work aims at improving Sea Ice Concentration (SIC) estimates from space, providing a new product that gives SIC under all-weather conditions through optimal blending of high spatial resolution Visible Infrared Imaging Radiometer Suite (VIIRS) ice concentration with ice concentration from passive microwave observation from Advanced Microwave Scanning Radiometer-2 (AMSR2).

Validation of VIIRS and passive microwave-derived SIC has been done using high-resolution Landsat data from the U.S. Geological Survey (USGS). In each scene there is a visible and thermal channel observation at 30 meter spatial resolution form the Operational Land Imager (OLI) and the Thermal Infrared Sensor (TIRS) onboard Landsat-8. Each pixel at the original spatial resolution is identified as either snow/ice or water under clear conditions based on the visible channel reflectance and the derived Normalized-Difference Snow Index (NDSI). SIC at lower spatial resolutions of 1 and 10 km are calculated as the ratio of the number of snow/ice pixels to the number of all pixels inside a grid cell. For each of the Landsat scenes a corresponding granule of the Suomi NPP VIIRS SIC with a spatial resolution of 750 m is located with a time difference of less than 1 hour. A daily mean SIC product is also obtained from AMSR2 at 10 km. Bias and RMSE of SICs form VIIRS and AMSR2 are calculated with regard to SIC from Landsat.

Method

After both VIIRS and AMSR-2 SICs are remapped into 1-KM EASE-Grid, the Best Linear Unbiased Estimator (BLUE) is then applied to derive the final ice concentration under clear sky conditions.

$$ICE_{CONC} = (\sigma_1^2/\sigma_1^2+\sigma_2^2)\times(ICE\_CON_1-D_1) + (\sigma_2^2/\sigma_1^2+\sigma_2^2)\times(ICE\_CON_2-D_2)$$

where ICE_CONC_1 and ICE_CONC_2 are the optimized ice concentrations from the two products; D_1 and D_2 are measurement biases; σ_1 and σ_2 are the measurement precisions. For the pixels under cloudy conditions, the resulting SIC is determined as the ice concentration form the microwave observations with bias correction. Furthermore, ice cover is defined by pixels with SIC larger than 15%. The final product will have the same spatial resolution as VIIRS (1 km) with ice product from microwave observations interpolated to the VIIRS spatial resolution.

Example Sea Ice Concentrations

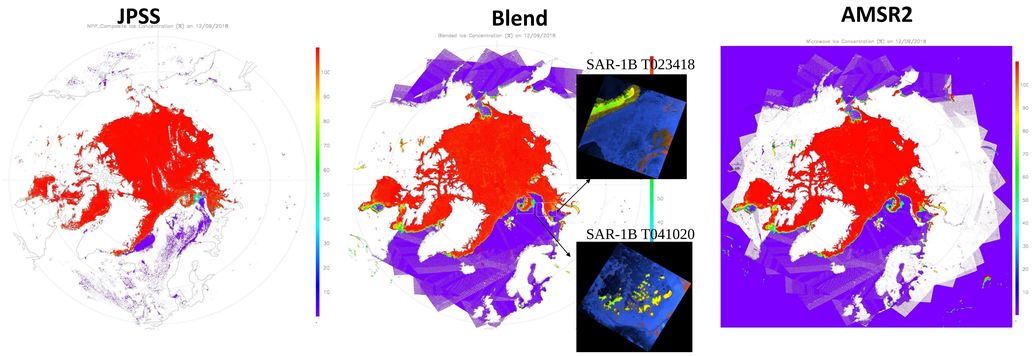

Figure 1: Examples of Daily Sea Ice Concentration Composite over Arctic on 09 Dec 2018. Left: SNPP-VIIRS, Middle: blended VIIRS and AMSR2, Right: AMSR2. SAR-1B images in boxed region over Franz Josef Land and Barents Sea

Validation Results:

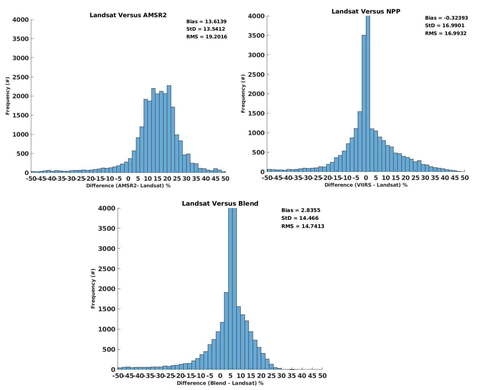

Figure 2: Histogram comparisons to Landsat from 12 Sea Ice Concentration scenes over Arctic from June 2019. Upper left is AMSR2, upper right S-NPP and lower middle is the Blended product.

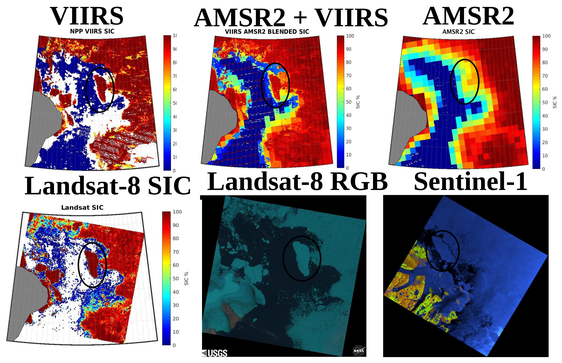

Figure 3: On August 1, 2019 in Greenland Sea off Greenland NE Coast. Top: VIIRS, Blended and AMSR2 SIC. Bottom: SIC, OLI/TIRS RGB from Landsat-8 and Sentinel-1 SAR image.

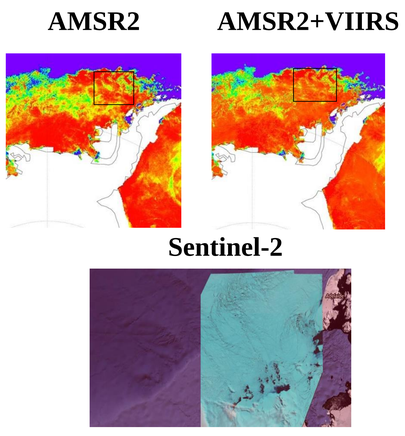

Figure 4: On 15 Oct 2017 over Bellingshausen Sea. Top: AMSR2 and Blended SIC; Bottom: Sentinel-2 RGB from the same day.

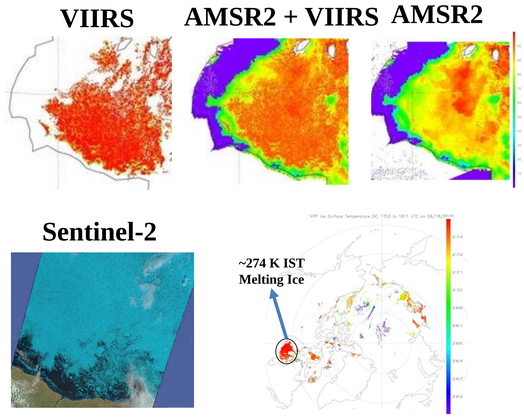

Figure 5: On 18 Jun 2018 over Southeast Hudson Bay.
Top: VIIRS, Blended and AMSR2 SIC .
Bottom: Sentinel-2 RGB from same day ~17 UTC , and NPP VIIRS IST at 260-275 K scale for same day ~18 UTC.

To the left is an example blending of the VIIRS and AMSR2 SIC from 09 December 2018. Notice the resultant SIC in Barents Sea, near Franz Josef Land and Canadian inland lakes. Next, validation results are shown from a dozen ice scenes analyzed from June 2019 with resultant statistics and histograms from cases (Figure 2). Overall, the blended SIC product reduces overall RMS error compared to VIIRS and AMSR2. A summer season case from 01 August 2019 over Greenland Sea (Figure 3) is shown where there were coinciding Landsat-8 and Synthetic Aperture Radar (SAR) imagery from Sentinel-1. Qualitative analysis indicates improvement when a blend of VIIRS plus AMSR2 SIC is utilized, with the AMSR2 SIC product noticeably missing a sea ice feature (circled). For this particular case both Standard Deviation and RMS errors (not shown) are reduced in blended product compared to VIIRS and AMSR2 SIC. Another case in the Antarctic region over the Bellingshausen Sea compared to Sentinel-2 RGB shown in Figure 4 gives further indication of AMSR2 SIC underestimation. A summer case on 18 June 2018 over Hudson Bay (Figure 5) gives additional indication that the AMSR2 retrieval has an underestimation of SIC when compared to Sentinel-2 RGB. Sensitivity in warm ice surface temperature environments, such as shown in southern Hudson Bay is a likely reason for the discernible underestimation of SIC in AMSR2.

Finally, Landsat and Sentinel 1-A and B SAR imagery that coincide with differences between the Blend and AMSR2 SIC during the 2017 March through June period were analyzed to see how often the NPP SIC improves upon the AMSR2 SIC in the Blend. These scenes where observed to have SICs that were anywhere from 25-75% difference in value. For Landsat a total of 117 images, of which only 11 occur in the Antarctic region. In total it was found to have a 75% success rate in having Blend improving the overall SIC field. For SAR comparisons, they are partitioned into Arctic and Antarctic, with 205 Arctic and 132 Antarctic scenes being analyzed, with Blend having a different SIC than AMSR2. It was found that the Blend had a success rate 85% over the Arctic and 82% over the Antarctic.

However, one caveat is that VIIRS still has some issues with ice cloud leakage. This is expected to be improved with the release of updated JPSS/VIIRS cloud products that provide cloud probabilities.

Conclusions

In summary, it has been shown that the higher resolution VIIRS data provides beneficial information to improve upon microwave (AMSR2) SIC under clear sky conditions. It was found that the AMSR2 retrieval suffers from low SIC bias in especially summer-time warmer ice conditions and the inclusion of VIIRS SIC mitigates that specific problem. For future work, to improve upon this product, we will include seasonally adjusted bias corrections.

Acknowledgements

Landsat images were obtained from the USGS Earth Explorer data portal. SAR images are from the University of Alaska Fairbanks, Alaska Satellite Facility data portal (Vertex). Sentinel-2 RGB images are from from European Space Agency, distributed via the USGS data portal. This project is supported by the NOAA JPSS Proving Ground and Risk Reduction Activity.

Enterprise Snow Cover Algorithm Migration

Aaron Letterly[1], Yinghui Liu[2], Peter Romanov[3], Jeff Key[2]

[1]Cooperative Institute for Meteorological Satellite Studies, University of Wisconsin–Madison

[2]NOAA/NESDIS Advanced Satellite Products Branch, Madison, WI

[3]NOAA Center for Earth System Sciences & Remote Sensing Technologies, the City College of New York, NY

Here we test, implement, and document the best **fractional snow cover (FSC) algorithm** for the **Advanced Baseline Imager (ABI)**. The current algorithm is called "GOES-R Snow Cover and Grain Size (GOESRSCAG)", which employs an optimized spectral unmixing analysis using 3 visible and 2 near-infrared bands. The operational snow fraction algorithm for the **Visible Infrared Imaging Radiometer Suite (VIIRS)**, which uses multiple bands for snow identification and a single reflectance band for snow fraction, is also being tested. Here we present some validation case studies with GOES-16 using the National Ice Center **Interactive Multisensor Snow and Ice Mapping System (IMS)** and **Landsat Normalized Difference Snow Index (NDSI)** as references.

Solar & Sensor Zenith Angle Dependencies

High sensor/solar zenith angles present can make accurate snow detection more difficult for both the VIIRS and GOESRSCAG algorithms. Below (left) is a bar plot showing the percentage of IMS pixels labelled as "snow" that were collocated with snow cover pixels from output using the VIIRS or the GOESRSCAG algorithms for six hours during March 17, 2019. The 4-panel figure (right) shows the observable snow cover south of Hudson Bay change abruptly as the solar zenith angle increases from 70º to 80º between 22:00 and 23:00 UTC.

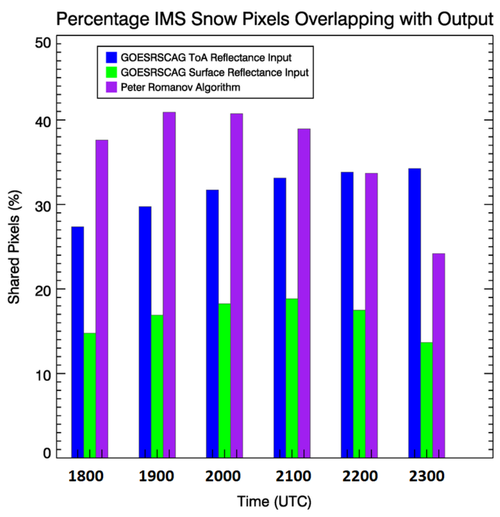

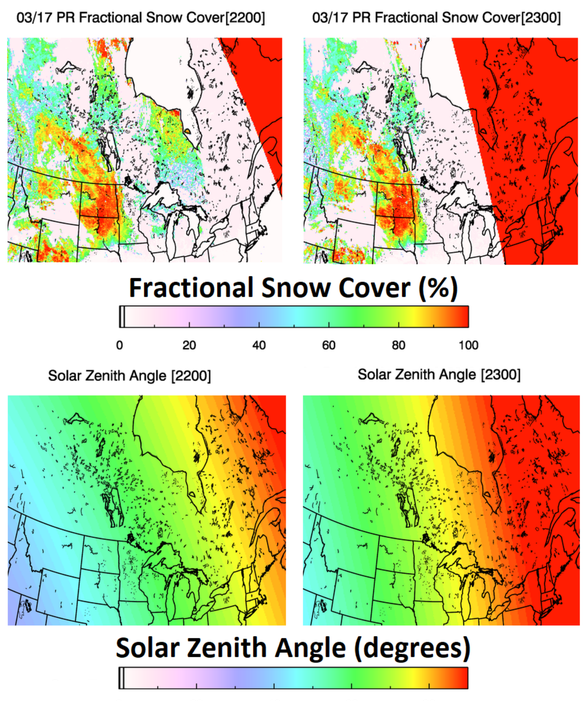

Shown below is a comparison of snow coverage from IMS and the VIIRS algorithm (labeled "PR" for its author) using GOES-17 (left) and GOES-16 (right) data for March 17 at 19:00 UTC. "Overlapping" means that both IMS and the VIIRS algorithm agree on the presence of snow. Snow pixels east of Hudson Bay from GOES-West are not detected due to the high sensor zenith angle near the edge of the disk, but are detected from GOES-East due to the lower sensor zenith angle.

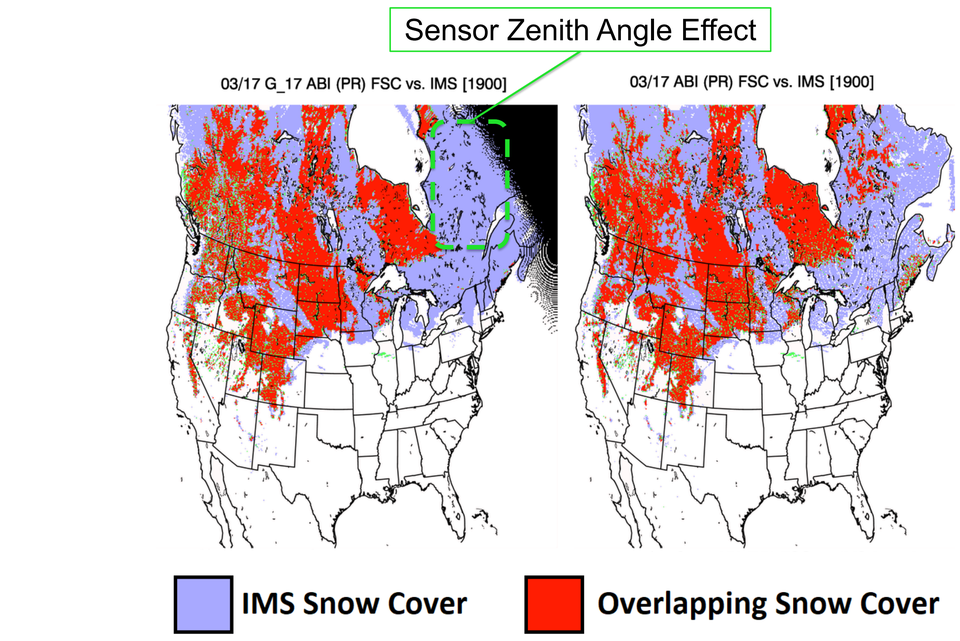

GOESRSCAG Screened by Snow Grain Size

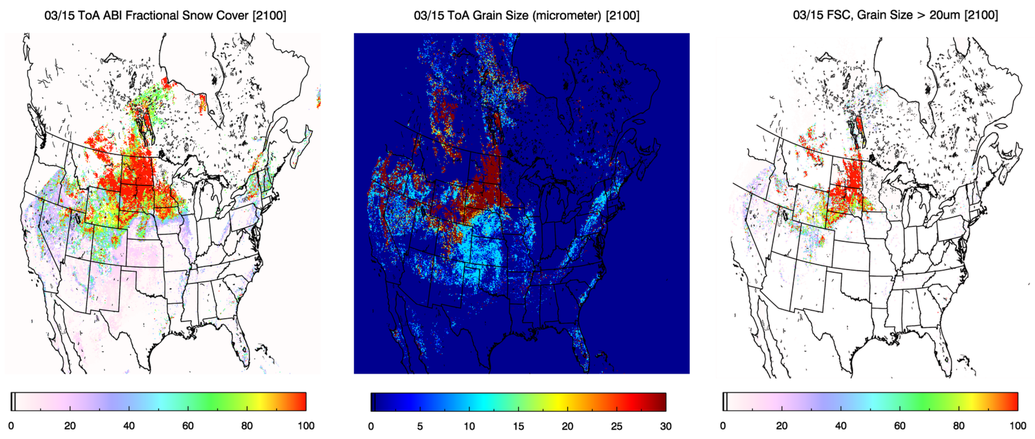

Filtering the operational product to ignore snow fraction where snow grain size is < 20μm removes much of the falsely-assigned snow in the southern United States. Above is the unfiltered FSC (left), snow grain size (center) and filtered FSC (right) on March 17, 2019.

GOES-16 Snow Cover Vs. IMS

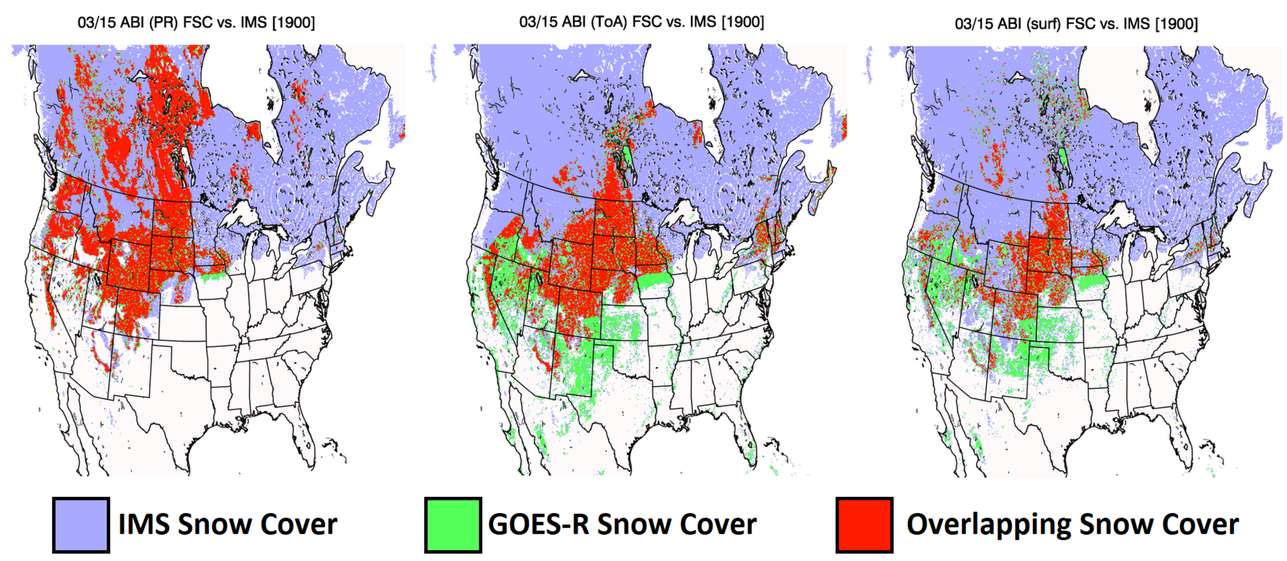

Shown above are the results of comparing the snow-covered pixels from IMS with output from (left) the VIIRS algorithm ("PR"), (center) GOESRSCAG algorithm using TOA reflectances as input, and (right) GOESRSCAG algorithm using surface reflectances as input for March 15 at 19:00 UTC. "Overlapping" means that both IMS and the VIIRS algorithm agree on the presence of snow.

GOES-16 Snow Cover Fraction Differences

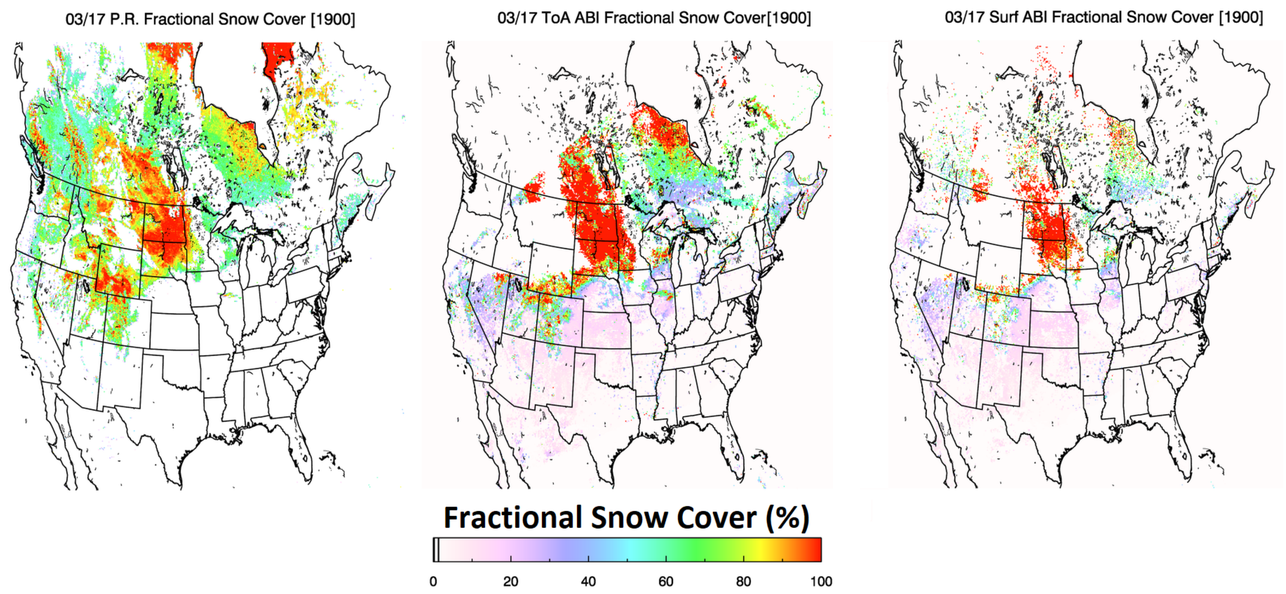

Fractional snow cover results from (left) the VIIRS algorithm ("P.R."), (center) GOESRSCAG algorithm using TOA reflectances as input, and (right) GOESRSCAG algorithm using surface reflectances as input for March 17 at 19:00 UTC.

Landsat Comparison and Validation

In many cases, snow cover from the VIIRS algorithm is more continuous than from the operational algorithm**.** Fractional snow cover shown here from Landsat NDSI (top left), the VIIRS algorithm (top right), GOESRSCAG algorithm using TOA reflectances as input (bottom left), and GOESRSCAG algorithm using surface reflectances as input (bottom right) for March 17 at 18:00 UTC. Landsat snow fraction data may have a positive bias due to the NDSI threshold used (0.55).

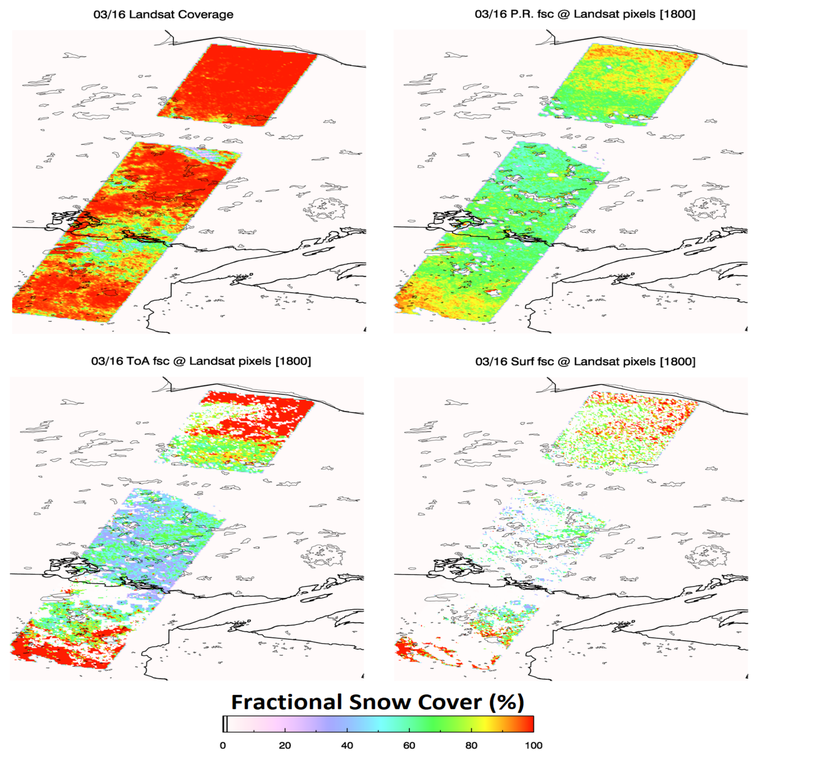

Conclusions and Future Work

GOES-16 snow cover from the VIIRS algorithm shows excellent agreement (where not cloudy) with IMS and Landsat.

GOESRSCAG snow cover is spatially inconsistent and occurs too far south unless snow grain size is used to filter the fractional snow cover.

Snow cover fraction output from the VIIRS algorithm is more continuous than GOESRSCAG snow cover output and has less intra-day variance.

Sun/sensor viewing geometry has some effect on snow cover identification in cases where solar/sensor zenith angle > 75º.

This work is supported by the NOAA PSDI/JPSS program.

Adaptation of MODIS Sea Ice Leads Detection Algorithm to VIIRS

Jay P. Hoffman[1], Steven A. Ackerman[1], Yinghui Liu[2],and Jeffrey R. Key[2]

[1]Cooperative Institute for Meteorological Satellite Studies / Space Science Engineering Center, University of Wisconsin-Madison

[2]NOAA/NESDIS Madison, WI

Background and Motivation

Leads are elongated fractures in the sea ice cover that form under stresses due to atmospheric winds and ocean currents. Leads provide a significant amount of heat and moisture to the Arctic atmosphere.

The purpose of this work is to extend the methodology developed to identify leads in MODIS to use VIIRS.

Algorithm Description

The method consists of the following steps:

- Acquire VIIRS level-1b imagery (SNPP & NOAA-20) from Band I5 (375m resolution 11 µm)
- Thermal contrast to identify potential sea ice leads (relatively large local brightness temperature standard deviation)
- Image processing to detect leads
- Derive object properties (length, area, width, orientation)

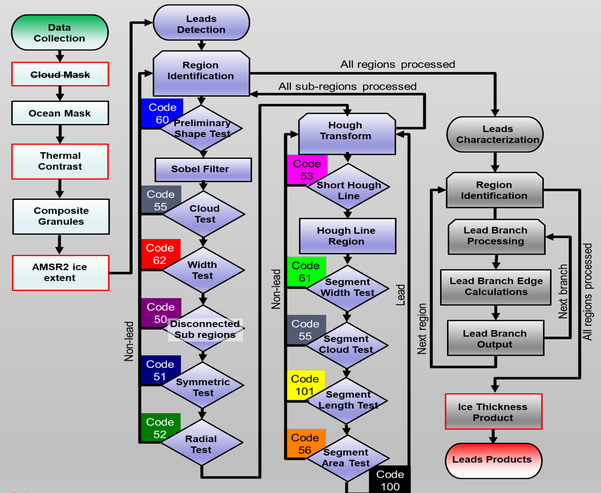

Notable Differences

- No cloud mask applied
- Require more than 4 observations with high thermal contrast
- Thermal contrast does not include absolute temperature range
- Use AMSR2 to establish ice edge
- Lead ice thickness included

Summary

- Routine product generation began late fall 2019
- Combined VIIRS and MODIS leads detections can offer greater confidence in leads location than from a single satellite
- Future work: investigate interaction of leads with other climate processes

Project website: www.ssec.wisc.edu/leads

Hoffman, Jay P.; Ackerman, Steven A.; Liu, Yinghui and Key, Jeffrey R. The detection and characterization of Arctic sea ice leads with satellite imagers. Remote Sensing. 2019, 11(5), 521; https://doi.org/10.3390/rs11050521

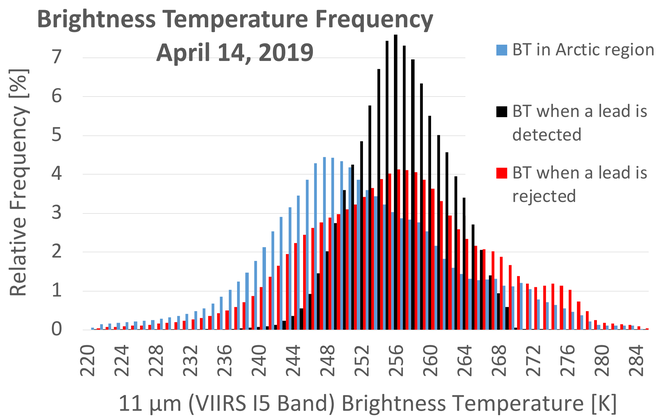

- Thermal contrast is the key to leads detection
- Brightness temperature alone is not a direct factor
- Leads brightness temperatures are usually below freezing
  - Pixels may include sea ice and water
  - Atmospheric path may include thin cloud
  - Leads may be new-ice

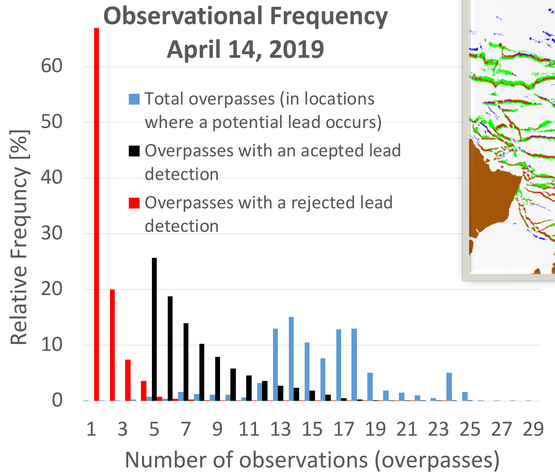

- The majority of the arctic receives more than 13 VIIRS overpasses in a day, more poleward locations receive twice as much coverage
- A VIIRS lead detection must have high thermal contrast in more than 4 overpasses. High thermal contrast is rarely detected in every (or even the majority) of the daily overpasses .
- The majority of high thermal contrast features that fail leads detection is due to infrequent repeat observations.
- Relatively few long-lasting thermal contrast features are leads are reject as leads (due to image processing for linear features)

Case Study

1km resolution 11 µm (Band 31) brightness temperature, warm features are dark

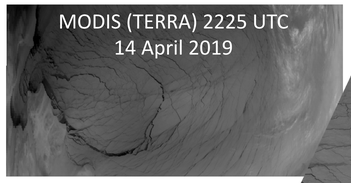

375m resolution 11 µm (I5) brightness temperature, warm features are dark

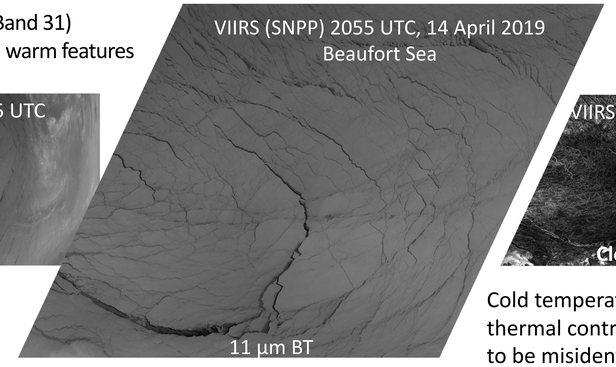

Leads apparent as high thermal contrast in atmospheric window brightness temperature

750m resolution Enterprise cloud probability, bright features are high cloud probably

Cold temperatures and high thermal contrast can cause leads to be misidentified as clouds

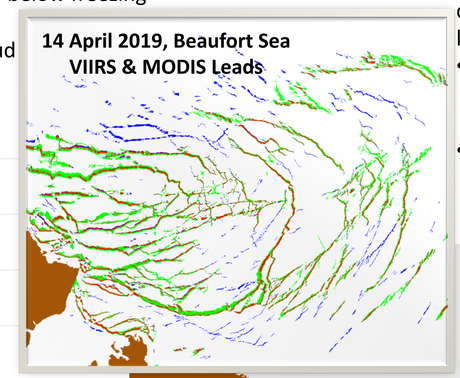

For the day, 40% of the MODIS leads area corresponds with a VIIRS lead; 70% of the VIIRS lead area is collocated with MODIS.

- Due to resolution differences, VIIRS leads detections are often thinner and encapsulated by a wider MODIS detection.
- Algorithm changes, instrument difference, overpass times, and clouds contribute to differences

In a mostly cloudy example over Laptev Sea, leads thermal contrast is observed through thin clouds

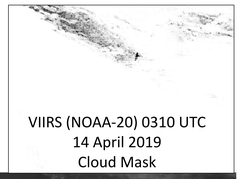

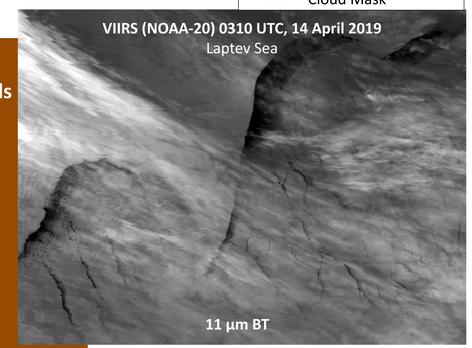

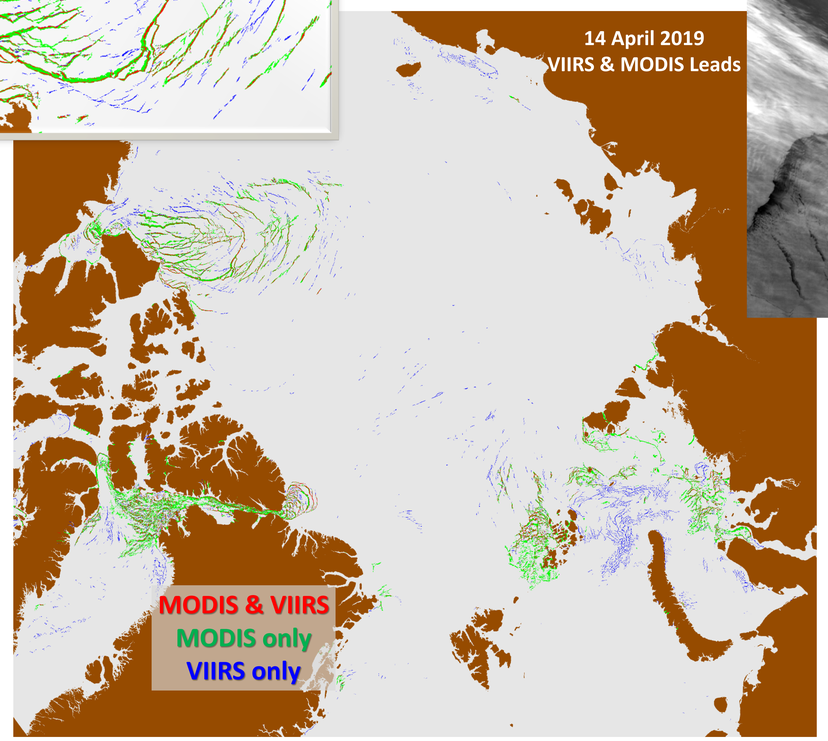

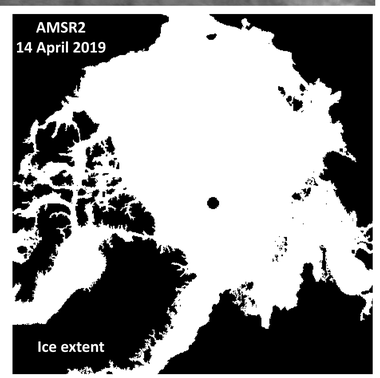

Lead detection search area is bound by AMSR2 ice extent

Acknowledgements: This work was supported by NASA grant #NNX14AJ42G & #80NSSC18K0786

Changes in Sea Ice Extent Will Outweigh Changes in Snow Cover in Future Arctic Climate Change

Aaron Letterly[1], Jeff Key[2], Yinghui Liu[2]

[1]Cooperative Institute for Meteorological Satellite Studies (CIMSS), University of Wisconsin, Madison, WI

[2]Center for Satellite Applications and Research, NOAA/NESDIS, Madison, WI

Introduction

Recent declines in Arctic sea ice and snow extent have led to an increase in solar energy absorption at the surface, resulting in additional heating and a further decline in snow and ice. Here we examine how changes in surface albedo over the ocean and land areas of the Arctic have separately affected shortwave absorption, and how the interplay between albedo and shortwave absorption may change in the future. **How do the trends in absorbed (net) solar radiation at the surface over land and ocean compare?** Based on these trends from the AVHRR Polar Pathfinder Extended (APP-x) dataset, we ask: what is the relative importance of the ice-albedo and snow-albedo feedbacks?

Trends in Absorbed Solar Radiation

The annual mean absorbed solar radiation at the Arctic surface has increased over the period 1982-2015, though the magnitude and rate were different over land and ocean. **Absorption over land increased 0.21 W m^{-2} yr^{-1}. Over ocean it increased 0.43 W m^{-2} yr^{-1}.**

This equates to an increase of 0.3% of the annual mean per year, resulting in a 10% increase over 34 years. Over land, the increase was 0.09% per year, increasing only 2.7% over the study period. The larger trend over ocean results from the larger albedo difference between sea ice and open water than between snow-covered and

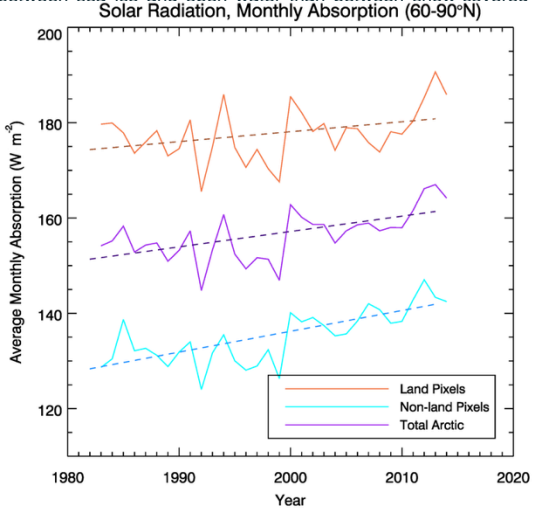

*Average monthly shortwave absorption per year (W m^{-2}), 60-90°N for combined land and ocean (**purple**), land only (**orange**), and ocean only (cyan). Dotted lines are linear trends.*

Absorbed Surface Radiation Trends, 1982-2015

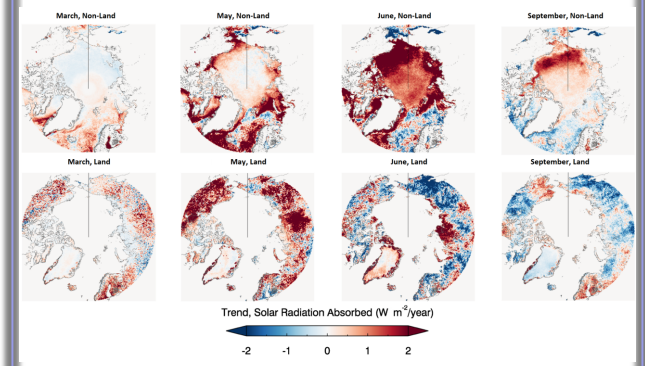

Trends in absorbed radiation for selected months over ocean (top) and land (bottom) in March, May, June, and September..

Surface Radiation vs. Cloud Trends, 1982-2015

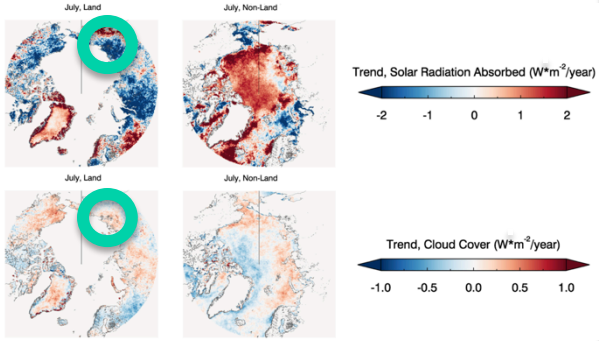

Trends in absorbed radiation (top) and cloud cover (bottom) for July 1982-2015.

Absorption Spatial Patterns

A strong increase in absorption due to decreasing springtime snow cover over land is seen in May. In June through October, the ocean area absorption rate increased faster than absorption over land. Changes in cloud cover also effect surface absorption. Over land, increasing (decreasing) cloud cover is associated with a decrease (increase) in surface absorption. The effects of cloud cover changes over ocean are muted due to the similar reflectivities of ice and cloud. Trends in absorbed radiation showed from APP-x agreed with trends in MERRA2 over the same time period.

Timing of Low-Albedo Threshold

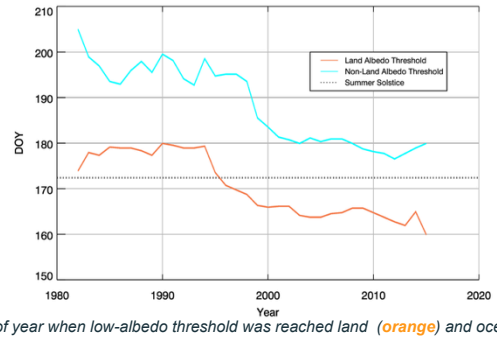

*Day of year when low-albedo threshold was reached land (**orange**) and ocean (cyan).*

In the first few years of the APP-x dataset (1982-1985), the minimum average albedo over the Arctic ocean was reached during the first two weeks of September. This value of 0.265 is used as the "ocean low-albedo threshold." A similar land "low-albedo threshold" was found to occur between June and July. The day-of year that these low-albedo thresholds were reached over land and ocean was determined for each year. **The low-albedo threshold was reached ~20 days earlier in 2015 than in 1982-1985 over ocean, and ~13 days earlier over land.** The regression of the low-albedo period towards earlier in the year results in lowered ocean albedo during the summer solstice a olstice.

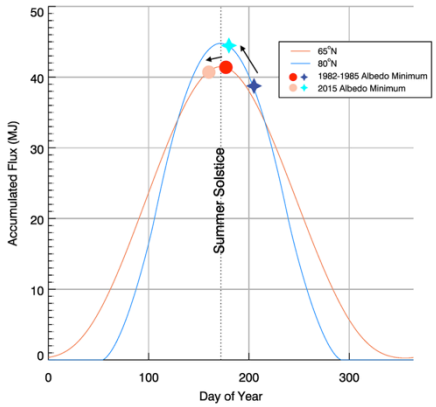

*Average TOA insolation at 14:00 Local Solar Time over **65°N** and **80°N** showing the regression of the low-albedo threshold between 2015 and 1982-1985.*

Reference: Letterly, A., J. Key, and Y. Liu, 2018, Arctic Climate: Changes in Sea Ice Extent Outweigh Changes in Snow Cover, The Cryosphere, 12, 3373–3382, https://doi.org/10.5194/tc-12-3373-2018.

Ice Products from NOAA Operational LEO and GEO Satellites

Xuanji Wang[1] (xuanjiwang@wisc.edu), Jeff Key[2], Yinghui Liu[2], Richard Dworak[1], Mark Tschudi[3], Aaron Letterly[1], and Sean Helfrich[2]

[1]Cooperative Institute for Meteorological Satellite Studies, University of Wisconsin–Madison
[2]NOAA/NESDIS Advanced Satellite Products Branch, Madison, WI
[3]University of Colorado-Boulder

Introduction

Ice on the ocean, lakes, and rivers is an important component of the global cryosphere that has significant impact on the local and global climate and environment. Sea, lake, and river ice exists not only in the polar regions, but also well into the midlatitudes. Ice macrophysical properties, including ice cover, temperature, concentration, thickness, and motion, play an important role in climate and environment changes, and are also critical for climate monitoring and modeling, weather forecasting, shipping and navigation, fisheries, and hazard mitigation. Therefore, accurate and prompt information on floating ice is important for Earth observation, weather prediction, and the Blue Economy. With NOAA's operational Low Earth Orbit (LEO) and geostationary (GEO) satellites, the global cryosphere can be monitored frequently in time and widely in space. NOAA "Enterprise" algorithms have been developed for a suite of ice parameters including ice surface temperature, concentration, thickness, and motion. These Enterprise products are now operational for the Visible Infrared Imaging Radiometer Suite (VIIRS) on NOAA-20 and S-NPP, and AMSR2 on GCOM-W1. They will soon be operational for the GOES-16 and -17 Advanced Baseline Imager (ABI). Validation studies of these ice products have been performed against in-situ, field campaign, and other satellite measurements from buoys, IceBridge aircraft campaigns, ICESat, and CryoSat-2. Results show that their performance meets the measurement accuracy requirements. This presentation illustrates these ice products and demonstrates their suitability, validity, and applicability.

Ice Concentration

Ice Products - LEO

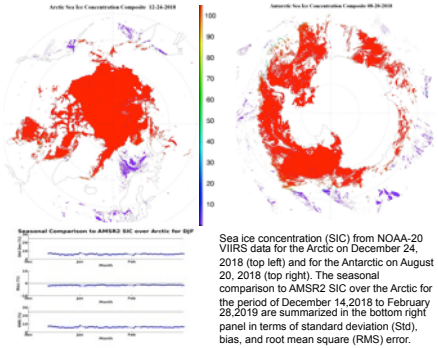

Sea ice concentration (SIC) from NOAA-20 VIIRS data for the Arctic on December 24, 2018 (top left) and for the Antarctic on August 20, 2018 (top right). The seasonal comparison to AMSR2 SIC over the Arctic for the period of December 14,2018 to February 28,2019 are summarized in the bottom right panel in terms of standard deviation (Std), bias, and root mean square (RMS) error.

Ice Products - GEO

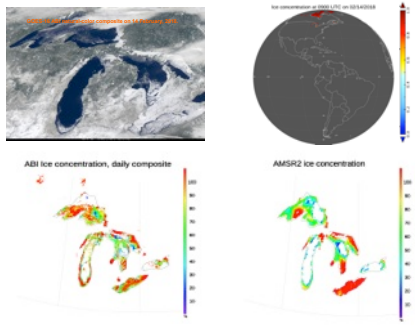

Ice concentration (IC) from GOES-R ABI data (lower left) and AMSR-2 (lower right) in the great Lakes, and full-disc IC (top right) and the GOES-16 ABI true color composite image (top left) on February 14, 2018.

Ice Temperature

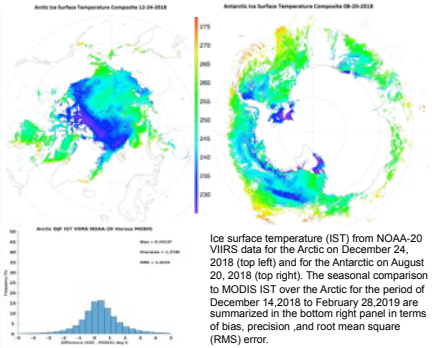

Sea ice surface temperature (IST) from NOAA-20 VIIRS data for the Arctic on December 24, 2018 (top left) and for the Antarctic on August 20, 2018 (top right). The seasonal comparison to MODIS IST over the Arctic for the period of December 14,2018 to February 28,2019 are summarized in the bottom right panel in terms of bias, precision ,and root mean square (RMS) error.

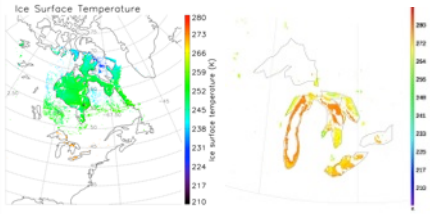

Validation of the ice surface temperature (IST) from GOES-R ABI is challenging due to the lack of in-situ measurements. A nearly identical IST retrieval algorithm for the Visible Infrared Imaging Radiometer Suite (VIIRS) onboard the Suomi National Polar-Orbiting Partnership (S-NPP) and NOAA-20 satellites has been validated against in-situ IST measurements from the NASA IceBridge Campaign over the period of 2013-2017. The validation studies give an overall bias (also called accuracy) of 0.1 K and root-mean-squared error (RMSE, also called precision) less than 1.0 K.

Ice surface temperature from GOES-R ABI in the area including Hudson Bay and the Great Lakes on February 24,2017 (left), and in the Great Lakes on February 14,2018 (right).

Ice Thickness

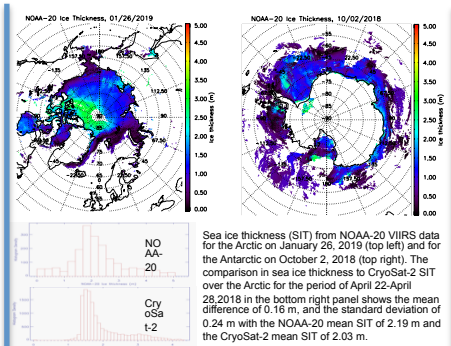

Sea ice thickness (SIT) from NOAA-20 VIIRS data for the Arctic on January 26, 2019 (top left) and for the Antarctic on October 2, 2018 (top right). The comparison in sea ice thickness to CryoSat-2 SIT over the Arctic for the period of April 22-April 28,2018 in the bottom right panel shows the mean difference of 0.16 m, and the standard deviation of 0.24 m with the NOAA-20 mean SIT of 2.19 m and the CryoSat-2 mean SIT of 2.03 m.

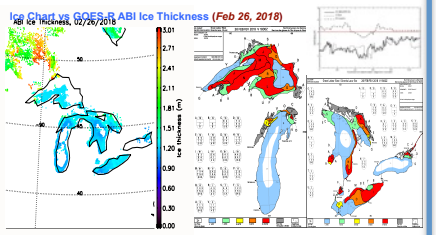

Ice charts report about ~70 cm ice for Great Lakes everywhere, and basically no ice for Lake Michigan except the far northern part and Green Bay, while GOES-R ABI shows about ~1 m ice in Lake Michigan, Lake Huron, and Lake Erie, and about 1.20 m ice in Lake Superior, Lake Ontario, Georgian Bay, and northern part of Lake Erie.

Ice thickness (daily composite) from GOES-R ABI data (left) and corresponding ice chart estimates in the Great Lakes on February 26, 2018 (right), and validation information shown in the top right corner.

Ice Motion

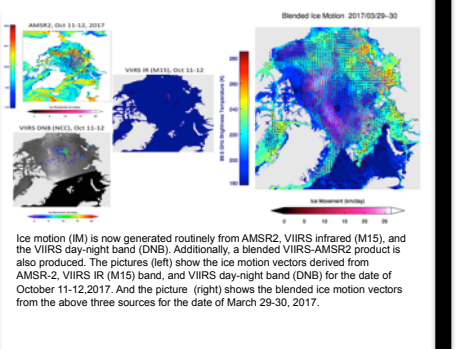

Ice motion (IM) is now generated routinely from AMSR2, VIIRS infrared (M15), and the VIIRS day-night band (DNB). Additionally, a blended VIIRS-AMSR2 product is also produced. The pictures (left) show the ice motion vectors derived from AMSR-2, VIIRS IR (M15) band, and VIIRS day-night band (DNB) for the date of October 11-12,2017. And the picture (right) shows the blended ice motion vectors from the above three sources for the date of March 29-30, 2017.

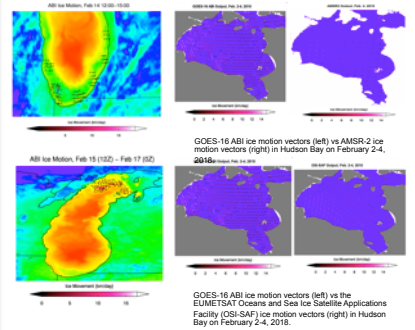

GOES-16 ABI ice motion vectors (left) vs AMSR-2 ice motion vectors (right) in Hudson Bay on February 2-4, 2018.

GOES-16 ABI ice motion vectors (left) vs the EUMETSAT Oceans and Sea Ice Satellite Applications Facility (OSI-SAF) ice motion vectors (right) in Hudson Bay on February 2-4, 2018.

Ice motion vectors from GOES-16 ABI data in the Great Lakes and the Hudson Bay (left), and validations against AMSR-2 and the EUMETSAT Oceans and Sea Ice Satellite Applications Facility (OSI-SAF) ice motion vectors (right).

A TROPOMI- and GLM-based Estimate of NO_x Production by Lightning over the U.S.

Dale Allen[1], Kenneth Pickering[1], Eric Bucsela[2], Jos van Geffen[3], Henk Eskes[3], Nickolay Krotkov[4], William Koshak[5], Pepijn Veefkind[3], and Jeff Lapierre[6]

[1]University of Maryland, [2]SRI International, [3]Royal Netherlands Meteorological Institute, [4]NASA Goddard Space Flight Center, [5]NASA Marshall Space Flight Center, [6]Earth Networks

Introduction

- Lightning produces NO because the extreme temperatures (>20000 K) in lightning channels dissociate molecular O_2 and molecular N_2, which then combine to form NO which quickly reacts with O_3 to form NO_2. Lightning is responsible for 10-15% of NO_x emissions globally. This is 2 – 8 Tg N a^{-1} (*Schumann and Huntrieser*, 2007) or 100 to 400 mol per flash. Much of the uncertainty stems from limited knowledge of lightning NO_x production per flash (LNO_x PE) or per unit flash length.

- Most LNO_x is injected into mid- and upper-troposphere where away from deep convection its lifetime is long relative to lower troposphere NO_x. NO_x in this region enhances the concentrations of upper tropospheric NO_y, OH, and O_3 & contributes to positive radiative forcing by O_3 and negative forcing by CH_4.

- We have previously used OMI NO_2 to obtain estimates of LNO_x production per flash over the Gulf of Mexico (*Pickering et al.,* 2016, *JGR*), in convective events during NASA's TC4 field program (*Bucsela et al.*, 2010, *JGR*), and over broad regions of the tropics *(Allen et al., 2019, JGR*) and midlatitudes *(Bucsela et al., 2019, JGR).* In the latter studies, we obtained PE values of 170 ± 100 mol flash and 180 ± 100 mol flash, respectively.

TROPOMI LNO_x PE Algorithm

$$PE = [V_{tropLNOx} \times \Sigma \text{ Area}] / [N_A \times \Sigma (\text{Flashes} \times \exp(-t / \tau))]$$

PE ≡ LNO_x Production Efficiency (moles NO_x/flash)
$V_{tropLNOx}$ ≡ Median vertical column density (VCD) of LNO_x over good quality (qa_value > 0.50) or good/fair quality (qa_value > 0.16[1]) pixels within ROI[2] that satisfy the DCC[3].
Area ≡ Area of pixels within ROI that satisfy the DCC or have P < 500 hPa and undefined cloud-fractions
N_A ≡ Avogadro's Number
Flashes ≡ Number of GLM or ENLN flashes[4] within ROI during 5 hour period before TROPOMI overpass[5]
t ≡ Age of individual flashes at the time of the overpass
τ ≡ Lifetime of NO_x in near field of convection (2, 3 (best guess), or 12 hours)

[1] Fair quality pixels have retrievals issues including in many cases AMF_{trop} / AMF_{geo} < 0.1
[2] Region of interest (ROI) ≡ Latitude-longitude region encompassing deep convective system
[3] Deep convective constraint (DCC) ≡ Cloud fraction[6] > 0.95 and cloud pressure[7] < 500 hPa
[4] GLM DE assumed to equal 78%. ENTLN DE for CG (IC) flashes assumed to equal 100 (79%)
[5] Overpass time ≡ Time TROPOMI exited ROI
[6] Cloud Fraction ≡ cloud_fraction_crb_nitrogendioxide_window variable from TROPOMI NO_2data
[7] Cloud pressure ≡ cloud_pressure_crb variable from TROPOMI support data

$V_{tropLNOx}$ = Median ($V_{tropNOx}$) – $V_{tropbkgn}$

$V_{tropNOx}$ = [S_{NO2} – avg ($V_{stratNO2} \times AMF_{strat}$)] / AMF_{LNOx} [avg over all pixels within ROI satisfying DCC]

S_{NO2} ≡ NO_2 Slant Column Density (SCD) for individual DCC pixels within ROI
$V_{stratNO2}$ ≡ Stratospheric VCD of NO_2 for DCC pixels within ROI
AMF_{strat} ≡ Stratospheric air mass factor for DCC pixels within ROI
AMF_{LNOx} ≡ AMF converting tropospheric slant column of NO_2 to vertical column of LNO_x.
$V_{tropbkgn}$ is estimated using 3 different methods
$V_{tropbkgn10}$ ($V_{tropbkgn40}$) ≡ 20th (40th) % of $V_{tropNOx}$ for non-flashing pixels within ROI satisfying DCC.
$V_{tropbcli}$ ≡ Mean value of $V_{tropNOx}$ for v1.3.x pixels satisfying the DCC within ROI on low-flash days between May 1 & Aug 22, 2019 (see Figure 1 below).

GOES-R GLM (*Goodman et al.*, 2013) is near-IR optical transient detector that detects lightning from changes in optical scene due to release of electromagnetic radiation
It is one of several instruments that are part of the payloads for NOAA's GOES-R series that includes GOES-16, operational at 75.2° W, and GOES-17, operational at 137.2°.

- Fig. 2 shows coverage region for GLM. GLM measures total number of CG & IC flashes with a spatial resolution of 8 km at nadir & 14 km at edge. Mean DE exceeds 70% but may be suppressed over inverted polarity storms, severe storms, and/or storms with deep liquid water path (*Koshak et al*., 2018).
- This study uses flashes from GOES-16 GLM.

Fig. 1. $V_{tropbcli}$; Values obtained by applying 5° box car smoother to 1° x 1° gridded values of $V_{tropNOx}$ obtained using pixels on low-flash days (< 10000 GLM flashes in domain during 5-hour period preceding TROPOMI overpass) that are more than ~50 km distant from lightning.

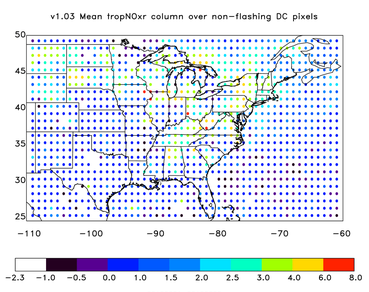

Fig. 2. Idealized representation of GLM flashes Observed by GLM-17 (left region) and GLM-16 (right region) from *Goodman et al.* [2013]

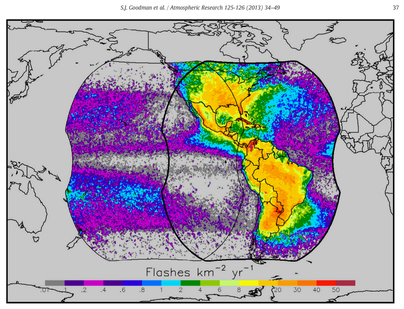

TROPOMI

Tropospheric Monitoring Instrument (TROPOMI) (*Veefkind et al*., 2012) onboard the Copernicus Sentinel-5 Precursor satellite retrieves numerous trace gases including NO_2 and cloud products such as cloud fraction and cloud top pressure. The TROPOMI NO_2 processing system (*van Geffen et al*., 2019, ATBD) is an improved version of the KNMI DOMINO system that retrieves 1) slant columns from Level 1b radiances using DOAS; 2) separates the tropospheric and stratospheric slant columns based on data from the TM5 model and assimilation system (*Huijnen et al*., 2010); and 3) converts the tropospheric and stratospheric slant columns to vertical columns by application of air mass factors (AMF) which include daily information on NO_2 vertical distributions from the TM5 model at 1° x 1° resolution. The horizontal resolution of the NO_2 products at nadir are approximately 3.6 km (cross track) × 7.2 km (along-track) prior to August 6, 2019 and 3.6 × 5.6 km after August 6, 2019. The TROPOMI NO_2 retrieval uses cloud-pressures from the FRESCO-S algorithm, which is based on the FRESCO+ algorithm described in *Wang et al.* (2008). Cloud fraction information is retrieved from the NO_2 spectral window and accounts for Rayleigh scattering.

This study uses TROPOMI products from TROPOMI v1.01, v1.3.x (processor version 1.03), and v.2.1_test where the latter is a modified Copernicus Sentinel data product created for this study that includes spike removal to better deal with saturation and blooming effects in the radiance spectra allowing for increased data coverage over bright (flashing) scenes. Overexposure of CCDs (saturation) is common for TROPOMI scenes affected by lightning. Blooming occurs when the influence of saturation spreads to neighboring wavelengths and pixels.

Figures 4a-f show GLM and TROPOMI (v2.1_test) products over deep convection observed on April 4, 2019 (upper left), April 13, 2019 (upper right), May 6, 2019 (center-left), July 8, 2019 (center-right), July 22, 2019 (lower-left), and August 9, 2019 (lower right). For each day, the upper left panels show GLM flashes during the 5-hour period preceding the time of the TROPOMI overpass. nF (nF_a) gives the total flashes before (after) adjusting for chemical decay assuming a 3-hour lifetime. The upper right panels show the cloud pressure and also its mean over pixels satisfying the DCC. The mid-left panels show the cloud fraction in the NO_2 window and also give the area of pixels satisfying the DCC. The mid-right panels show S_{NO2} and give the number of DCC pixels for which S_{NO2} is defined. The lower-left panels show $V_{tropNOx}$ for good quality pixels (quality flag > 0.50). The mean value of $V_{tropNOx}$ and the number of pixels for which it is available are also shown. The lower-right panels also show $V_{tropNOx}$ but for good- and fair-quality pixels (quality flag > 0.16).

Fig. 4

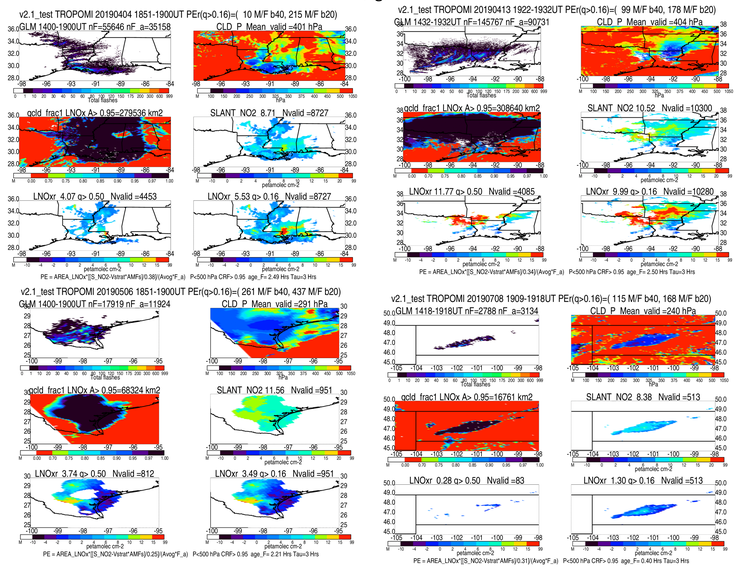

YYYYMMDD	Region	Area	Nflashes	Age_Fl	Nflash_a	A_LNOx	VLNOxr	VLNOx_b40	VLNOx_b20	VLNOx_bkm	LNOxPEb40	LNOxPEb20	LNOxPEcli	NPTS
20180721c	86W-81W 28N-33N	81710	99561	2.71	43822	0.34	6.2	3.81	1.7	1.32	73	139	150	1715
20180723c	90W-82W 24N-30N	122176	37430	2.13	19944	0.33	11.77	10.69	7.11	0.25	109	473	1171	2738
20180726c	83W-79W 28N-31N	27874	40309	1.77	23947	0.36	3.01	3.1	2.26	0.23	-1	14	53	370
20190404c	98W-84W 28N-36N	279536	100829	2.48	49782	0.38	5.53	5.46	3.91	1.42	7	151	383	8727
20190413c	100W-88W 28N-38N	308640	225876	2.33	115778	0.34	9.99	8.23	6.84	1.03	77	139	396	10280
20190422c	98W-88W 38N-48N	22733	1083	2.86	430	0.62	1.24	0.84	-0.3	1.77	348	1347	-459	447
20190430c	105W-87W 33N-45N	287191	51190	1.91	30345	0.42	4.61	3.04	1.99	1.42	246	411	500	8101
20190505c	86W-78W 25N-31N	109140	90021	2.01	50770	0.33	4.43	0.78	-2.41	0.43	130	244	142	1733
20190506c1	102W-95W 38N-43N	49985	21858	1.7	13251	0.5	1.12	0.68	0.3	1.5	27	50	-24	1027
20190506c2	100W-95W 25N-30N	68324	42631	2.37	21087	0.25	3.49	0.74	-1.1	0.93	147	246	137	951
20190506c3	82W-73W 25N-31N	55903	21880	1.17	15552	0.47	-0.33	-1.46	-2.4	0.52	67	123	-50	1092
20190510c	98W-91W 25N-30N	60569	117907	2.74	52502	0.34	8.39	7.59	6.04	1.32	15	45	135	2173
20190528c	98W-88W 37N-43N	107665	56258	1.35	37303	0.52	1.67	0.77	-0.18	1.67	42	88	0	2578
20190531c	70W-60W 35N-40N	44355	53037	3.49	17637	0.53	3.65	2.01	0.92	1.09	68	114	106	845
20190608c	90W-78W 25N-35N	120395	110249	2.16	60204	0.36	2.7	2.39	1.32	1.15	10	45	51	3901
20190611c	87W-78W 25N-31N	45181	38536	1.36	25922	0.36	-0.18	-1.09	-2.8	0.44	26	75	-18	625
20190622c	102W-96W 40N-46N	31459	15192	2.62	6888	0.43	0.22	-0.18	-0.76	2.14	30	74	-145	999
20190623c	98W-88W 33N-38N	124840	102220	2.16	55823	0.29	1.9	2.03	0.95	0.97	-4	35	34	3070
20190630c	95W-87W 42N-48N	146174	155025	2.59	72248	0.5	2.71	1.75	0.3	1.83	32	81	29	3250
20190705c	99W-92W 36N-41N	88902	56078	2.31	28983	0.43	0.21	-0.29	-1.12	1.35	25	67	-58	1191
20190706c	88W-82W 27N-31N	74759	46214	1.89	26674	0.34	1.88	1.6	0.51	0.88	12	64	46	1038
20190708c	105W-98W 45N-50N	16761	13894	0.38	12280	0.31	1.3	0.01	-0.58	2.27	29	42	-21	513
20190713c	83W-77W 33N-36N	52490	75642	1.15	53282	0.4	1.96	0.94	-0.05	2.06	16	32	-1	788
20190716c1	96W-92W 41N-45N	19278	25152	2.55	11563	0.57	4.43	4.14	3.27	1.97	8	32	68	282
20190716c2	94W-88W 31N-36N	31520	15809	3.21	6180	0.44	3.31	0.57	-0.69	1.07	231	338	189	483
20190722c	92W-84W 34N-38N	56983	24726	1.69	14987	0.48	3.67	2.79	2.14	1.85	55	96	114	820
20190809c	77W-72W 30N-34N	30498	21612	1.7	13306	0.3	3.27	1	0.22	0.18	86	116	117	666
20190814c	92W-82W 28N-33N	82472	106588	1.46	69804	0.27	2.98	1.39	-0.15	1.64	31	61	26	3021
20190815c	100W-92W 38N-43N	56608	36756	2.59	17162	0.58	2.58	1.79	0.97	1.56	43	87	55	2191
All dates	All regions	89797	62192	2.1	33361	0.41	3.37	2.25	0.97	1.25	68	167	108	2262

Table 1. Details on the 29 case studies used to estimate LNO_x PE from GLM16 flashes and v2.1_test TROPOMI data. The table lists the date and location of each convective systems as well as details needed to estimate the LNO_x PE for each case.

In this table, area is given in km², the age of flashes (Age_Fl) is given in hours, VCDs of NO_x are given in peta molec cm^{-2}, and the PE is given in mol per flash. Nflashes gives the number of GLM flashes while Nflash_a is the number of flashes after adjusting for chemical decay assuming a chemical lifetime of 3 hours. Negative values of PE indicate that background columns over non-flashing grid boxes exceed the median columns in the region.

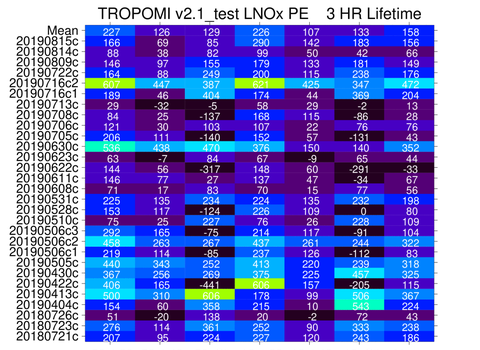

Table 2. LNOx PE assuming a 3-hour chemical lifetime for each of the 29 cases (y-axis) as derived using v2.1_test TROPOMI products and DE-adjusted GLM flashes for two TROPOMI quality flag thresholds (0.50 or 0.16) and three background assumptions (20%, 40%, or climatological).

The suffixes b20 and b40 indicate that the tropospheric background is day-specific and given by the 20th (40th)% column over non-flashing grid boxes within the footprint of the storm with CTPs < 500 hPa and cloud fractions > 0.95. The suffix Cli indicates that the mean background for flash-less deep-convective grid boxes over the summer of 2019 is used for that location.

The mean LNO_x PE over the 29 cases for the 6 approaches is 158 mol per flash. The mean PE for ENTLN flashes (not shown) is 112 mol per flash.

Tables 3 and 4 (below) show the mean LNO_x PE over the 29 cases as a function of lightning source (ENTLN or GLM), tropospheric background choice (climatological, b40, or b20), NO_x lifetime (2, 3, or 12 hours) and TROPOMI version (v1.3.x (left) and v2.1_test (right)). Colors show the standard deviations over the 29 cases.

LNO_x PE increases by more than a factor of two as assumed tropospheric background is decreased from 40 to 20%. Values for climatological background are in-between suggesting that the actual bkgn is between 20 and 40%.

LNO_x PE is ~50% greater for GLM flashes than ENTLN flashes suggesting that the assumed DE of 78% for GLM is too high or less likely that the assumed (100% for CG & 79% of IC flashes) DE for ENTLN is too low.

LNO_x PE decreases by approximately a factor of 2 as assumed lifetime varies between 2 and 12 hours.

LNO_x PE is ~20% higher for v2.1_test, which has fewer saturation issues, and consequently provides more robust estimates of LNO_x column and storm area.

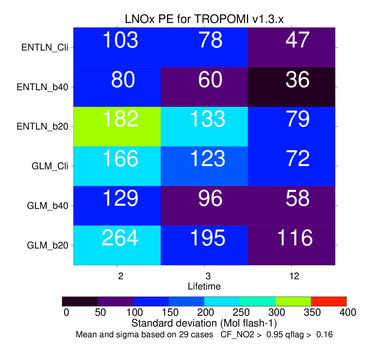

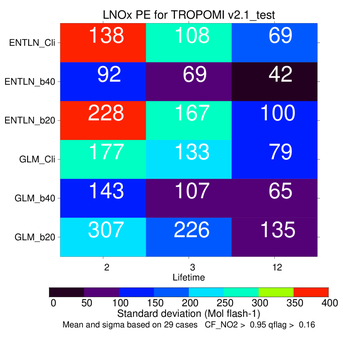

Figures 3a-c show GLM and TROPOMI products over deep convection. TROPOMI products are shown for v1.01, v1.3.x, and v2.1_test. See Figure 4 caption for details on individual plots. For this system over the panhandle of Florida, the number of valid good (fair or good) quality $VLNO_x$ retrievals over pixels influenced by deep convection and/or lightning increased from 810 (985) in v1.01, to 1031 (1193) in v1.3.x, to 1482 (1715) in v2.1_test leading to more robust estimates of LNO_x PE.

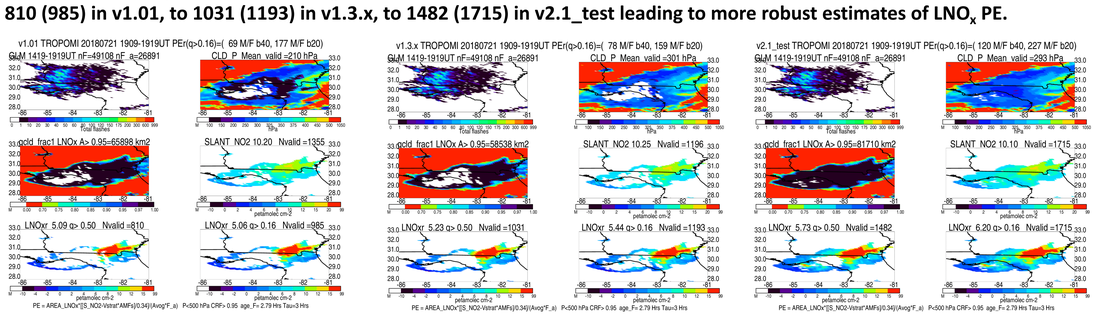

Uncertainties

- AMFs used to convert SCDs of NO_2 to VCDs of NO_x vary with viewing geometry, Rayleigh and Mie scattering, the vertical profile of NO_2, and the NO / NO_2 ratio within a deep convective system (e.g., *Silvern et al.*, 2018).
- NO_x τ in near field of convection is assumed to equal 3 hours; it varies from 2-12 hours depending on proximity to deep convection (e.g., *Nault et al.* (2016).
- LNOx PE is sensitive to the VCD of NOx due to sources other than recent lightning (e.g., *Allen et al*., 2019).
- DE for GLM flashes is assumed to equal 78%; which ignores storm-by-storm variations in DE. Comparison with ENTLN suggests this value is too high for these systems.
- TROPOMI columns are often missing due to saturation over bright regions where flashes and presumably $VLNO_x$ are large.
- Are these cases representative of deep convective systems over the United States and adjacent western Atlantic?

Summary

- LNO_x PE was estimated using GLM and ENTLN flashes and TROPOMI NO_2 columns for 29 convective systems observed during the spring- and summer of 2018-2019
- Mean LNO_x PE for a 3-hour lifetime ranged from 69 ± 83 mol per flash for ENTLN flashes and a 40% background to 226 ± 150 mol per flash for GLM flashes and a 20% background.
- Tropospheric NO_2 retrievals with TROPOMI are difficult over deep convective scenes due to small tropospheric AMFs, saturation of CCD pixels affected by lightning and blooming effects. However, tweaks to the processing algorithm allow more retrievals over these scenes.
- Future work will include refinement of the tropospheric background approach and analysis of the representativeness of these 29 cases.

- Acknowledgments: Much of this study is funded under the NASA Aura Science Team

NO_x Production by Lightning as Inferred Using NO_2 Slant Columns from GCAS during the GOES-R Validation Campaign

Kenneth Pickering[1], Dale Allen[1], Lok Lamsal[2], Scott Janz[3], Matthew Kowalewski[2], Mason Quick[4], Richard Blakeslee[5], William Koshak[5], Jeff Lapierre[6]

[1]University of Maryland, [2]USRA/GESTAR, [3]NASA Goddard Space Flight Center, [4]University of Alabama Huntsville, [5]NASA Marshall Space Flight Center, [6]Earth Networks

Introduction

- Lightning produces NO because the extreme temperatures in lightning channels dissociate O_2 and N_2, which then combine to form NO, which quickly reacts with O_3 to form NO_2.
- On average, each lightning flash produces 100 to 400 moles of NO_x or 2 – 8 Tg N yr^{-1} [Schumann and Huntrieser, 2007] for a global flash rate of ~45 flashes s^{-1}. Much of the uncertainty stems from limited knowledge of NO_x production per flash (LNOx PE) or per unit flash length.
- Most LNO_x is injected into middle and upper troposphere where away from deep convection it is relatively long-lived and enhances the concentrations of upper tropospheric NO_y, OH, and O_3 and contributes to positive radiative forcing by O_3 and negative forcing by CH_4.
- In this study, we estimate LNO_x PE using columns of NO_2 retrieved by the Geo-CAPE Airborne Simulator on board the NASA ER-2 aircraft during the GOES-R Validation Campaign during Spring 2017 and flash rates from the Geostationary Lightning Mapper (GLM), the Earth Networks Total Lightning Network (ENTLN), and the NASA Marshall Fly's Eye GLM Simulator (FEGS)

GOES-R Validation Campaign

The GOES-R Validation Campaign was conducted during March – May 2017 using the NASA ER-2 (Fig. 1) aircraft based at Palmdale, CA and Warner-Robins, GA. Its primary purpose was validation of the Advanced Baseline Imager (ABI) and Geostationary Lightning Mapper (GLM) satellite instruments aboard GOES-R. The NASA Goddard Geo-CAPE Airborne Simulator (GCAS) UV/Vis spectrometer piggybacked on the aircraft mission to allow observations of NO_2 simultaneously with lightning detection by the NASA Marshall Fly's Eye GLM Simulator (FEGS).

Table 1. Daytime GOES-R Campaign Flights with GCAS Data and Cloud Physics Lidar (CPL) Cloud Heights

Date	Location	Start Time (UT)	End Time (UT)
4/20/17	Toronto LMA	2330	0015
4/22/17	N. Alabama LMA	2030	0030
5/8/17	NE Colorado LMA	2145	0100
5/12/17	LA/MS/Gulf of Mex	1415	2015
5/14/17	Atlantic Ocean off FL	1315	1715

Figure 1

GOES-16 GLM, ENTLN, and TEMPO

- Geostationary Lightning Mapper (GLM) aboard GOES-16, a geostationary satellite launched on 19 Nov 2016, maps the distribution of lightning flashes at ~10 km spatial resolution with mean detection efficiencies (DEs) exceeding 70%. DEs for this campaign were obtained via comparison with flashes from FEGS.
- The Earth Networks Total Lightning Network (ENTLN) detects low frequency sferics in the 1-12 MHz range. The CG and IC DEs were ~100% for CG flashes and ~79% for IC flashes.
- When launched into a geostationary orbit in 2022, TEMPO will scan North America from east to west hourly measuring changes in NO_2, O_3, and other pollutants
- In the future, we plan on taking advantage of the synergy between the two geostationary instruments by using TEMPO NO_2 with GLM flashes to obtain estimates of NO_x production per flash.
- A demonstration of this future synergy was possible through the GOES-R validation suborbital campaign.

Airborne Instruments

- FEGS (Fig. 2, *Quick et al., 2017)* is an airborne array of multi-spectral radiometers optimized to study the optical emission from lightning through the cloud top. It provides a one to-one comparison to GLM observations. FEGS uses a 5 x 5 array of radiometers sensing at 777 nm. Each radiometer is pointed in a different direction, such that flashes can be continuously sensed in a ~10 x 10 km field of view as the ER-2 aircraft passes over a storm.
- GCAS (Fig. 3, *Kowalewski and Janz,* 2014) contains two spectrometers that provide imaging capabilities from the UV to NIR. This spectral range is separated into UV/VIS (300-490 nm) and VIS/NIR (480 – 900 nm) channels. The UV/VIS channel is used primarily for atmospheric trace gas measurements. Column amounts of atmospheric pollutants (e.g., NO_2, O_3, HCHO, and aerosols are retrieved from the high resolution (0.6 nm) UV/Vis spectrometer spectra.

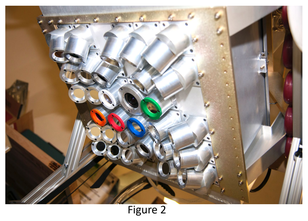

Figure 2

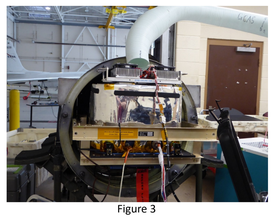

Figure 3

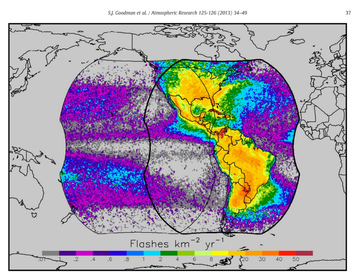

Combined FOV for GOES-17 and GOES-16 superimposed on climatological flash density from OTD-LIS (*Goodman et al.*, 2013)

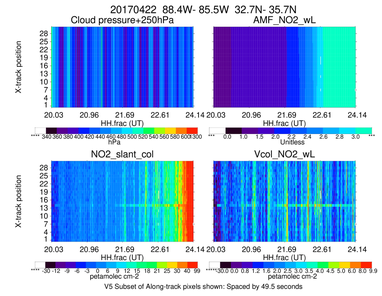

NO_2 vertical columns (lower right) are derived from slant columns (lower left) over pixels with CPL P < 300 hPa (upper left) using AMFs (upper right)

Algorithm

GCAS measures solar radiation backscattered from the surface and atmosphere (*Kowalewski and Janz*, 2014). NO_2 SCDs are derived by fitting a modeled spectrum to the observed spectrum using the QDOAS spectral fitting package.

GCAS is unable to obtain a solar reference spectra. Therefore, reference spectra required for trace gas retrievals are derived from nadir observations over a clean but cloudy region. The 2.5 minute period centered at 2213 UT May 8th was used during the GOES-R campaign.

SCDs are converted to tropospheric vertical column densities (VCDs) using air mass factors (AMFs) calculated with VLIDORT (*Lamsal et al.*, 2017) and tropopause pressures from MERRA-2.

NO_x and NO_2 profiles needed to convert NO_2 VCDs to LNO_x VCDs are obtained from GEOS-5 GMI-Replay simulations performed with and without lightning NO_x.

GCAS data retrieved in form of 250 m x 250 m pixels (31 pixels cross track with averaging along track).

Uncertainty exists as to how far into the storm cloud GCAS is able to detect NO_2. We assume a depth of 250 hPa, which is the mean difference between the cloud pressure obtained by the CPL aboard the ER-2 during the May 12th flight, which occurred near the overpass time of OMI, and the OMI optical centroid pressure (OCP).

LNO_x Production per Flash = $[VCD_{NO2(median)} \times$ Flash Area $\times rNO_x/NO_2] /$[Avogadro's_number $\times$ Nflashes]

rNO_x/NO_2 = Flight-track averaged ratio of upper tropospheric LNO_x to LNO_2 from GEOS-5 on date & time of flight

Nflashes = Number of GLM or ENTLN flashes adjusted for 3 hour lifetime of NOx in near field of convection

Thunderstorm Case Studies from the GOES-R Validation Campaign

NEXRAD Base Reflectivity and Flight Track | GCAS-derived VCD of NO2 | GLM Flashes | ENTLN flashes

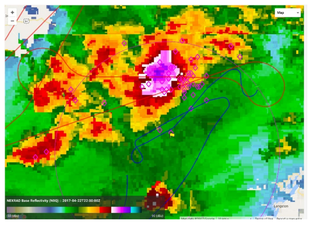

Figure 4

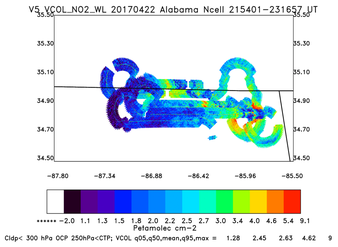

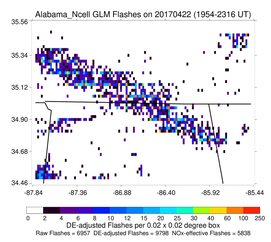

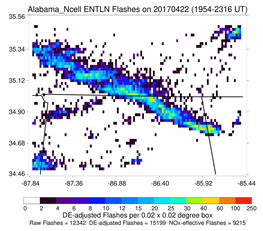

April 22, 2017 Alabama Storm: As a cold front approached from the west the ER-2 overflew two supercells, initially NW and W of Huntsville, AL over the period 2030 to 2310 UT. The primary focus was on the northern storm between 2150 and 2310 (Figure 4). After the northern storm weakened, the focus shifted to the southern storm, now southeast of Huntsville. It was overflown from 2320 to 0030 UT (Figure 5).

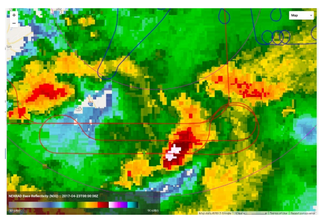

Figure 5

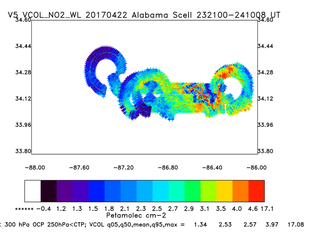

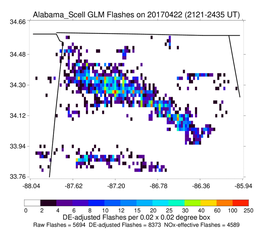

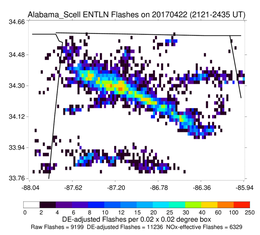

NO_2 VCD, GLM, and FEGS flashes as a f(t)

April 22, 2017 Alabama N storm

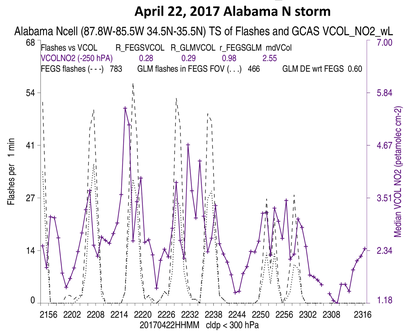

April 22, 2017 Alabama S storm

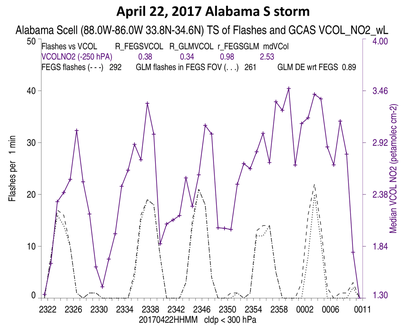

Uncertainties

- Are GCAS NO_2 columns in swaths along the flight tracks representative of the storm?
- How representative of background conditions is the GCAS reference column?
- Are modeled NO_x/NO_2 ratios representative of ratios observed in an actual convective system given uncertainties in UT NO_y chemistry (e.g., *Silvern et al.*, 2018) and the model simulation?
- ENTLN assumes a CG DE of 100% and IC DE of 79%. GLM DE is determined with respect to FEGS data. How accurate are GLM and ENTLN flash counts and what percentage of the flashes contribute to the observed columns?
- These calculations assume a NO_x lifetime of ~3 hrs in near-field of convection (Nault et al., 2016).

LNO_x PE is inversely correlated with flash density but uncorrelated with IC/CG ratio. If an IC flash made much less NO_x than a CG flash, would expect a negative correlation.

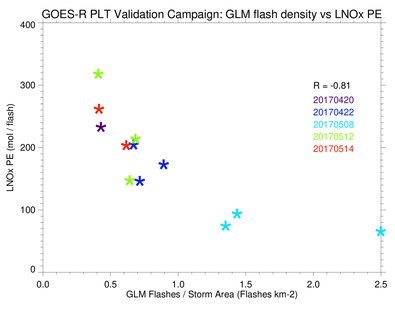

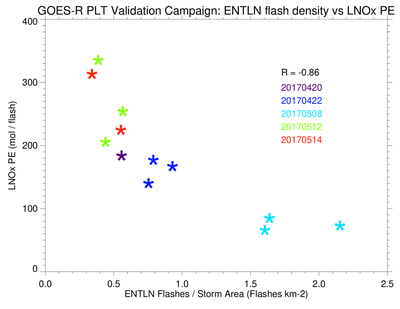

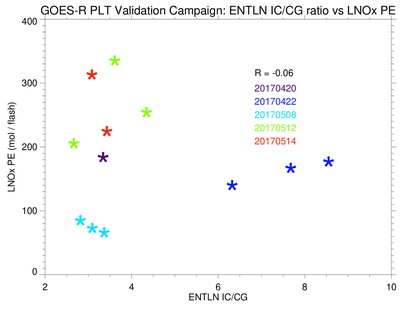

Storm	Date	Time	Location	VCD	Flash area	rLNOx / LNO2	GLM (ENTLN) Flashes	GLM (ENTLN) DE	GLM (ENTLN) LNOx PE
Lake Erie	Apr 20	2312-2352	41-43.5 N 82-77 W	2.55	13710 (23634)	2.15	8627 (21028)	0.76 (0.84)	211 (163)
AL_NS cells	Apr 22	2025-2147	34-36N 88.5-86.5 W	2.27	11989 (16616)	3.60	15045 (21758)	0.78 (0.81)	151 (145)
AL_Ncell	Apr 22	2154-2316	34.5-35.5N 87.8-85.5 W	2.45	8698 (11656)	3.03	9798 (15199)	0.71 (0.81)	183 (155)
AL_Scell	Apr 22	2321-2435	33.8-34.6 N 88-86 W	2.53	6400 (8378)	2.14	8373 (11236)	0.68 (0.82)	125 (119)
CO_South	May 08	2146-2300	39.75-40.0 N 105-104.2 W	2.12	1136 (1348)	3.18	4162 (4355)	0.45 (0.84)	44 (51)
CO_North	May 08	2146-2345	40-41 N 105-104.2W	2.22	3698 (4485)	3.00	7913 (11428)	0.53 (0.85)	72 (63)
CO_East	May 08	2353-2459	40-51 N 104-102.9 W	2.25	5137 (7029)	1.94	10281 (16630)	0.54 (0.84)	53 (45)
MS_AL_Line	May 12	1410-1509	29.5-32.5N 92-87 W	2.43	11923 (21884)	3.28	10834 (18644)	0.64 (0.83)	192 (233)
Gulf Line	May 12	1520-1640	28-29.25 N 93-90.5 W	1.32	2404 (2791)	3.71	2985 (2416)	0.48 (0.85)	126 (184)
Coastal Line	May 12	1653-2013	29-31 N 91-87.5 W	1.94	27023 (35628)	3.79	28071 (34734)	0.65 (0.84)	297 (314)
Atl_Ecell	May 14	1240-1359	29-31 N 75.5-72 W	2.06	17156 (25757)	3.29	16296 (24467)	0.70 (0.84)	182 (203)
Atl_Wcell	May 14	1419-1710	29.1-30.1 N 75.5-73.5 W	1.77	7545 (9056)	3.40	9007 (8828)	0.64 (0.84)	240 (292)
									157 ± 76 (164 ± 87)

Conclusions

- GCAS NO_2 columns were analyzed in relation to observed lightning during 12 storms overflown by the ER-2 aircraft on 5 flight days during the GOES-R Validation Campaign
- LNO_x PE was found to be ~160 ± 80 mol per flash approximately the same as the 180 ± 100 mol/flash found by Bucsela et al. (2019) for mid-latitude lightning through analysis of OMI NO_2 data.
- LNOx PE is similar using GLM and ENTLN, as a greater number of ENTLN flashes is accompanied by larger storm area
- LNO_x PE is negatively correlated with flash density (R=-0.81) consistent with belief that storms with high flash densities have smaller individual flash channel lengths and produce less NO_x per flash. However, it is uncorrelated with the IC/CG ratio.

Acknowledgments: Funding to S. Janz, GSFC PI, under the GEO-CAPE project (J. Al Saadi), with subaward to D. Allen, UMD PI. Thanks to Luke Oman for assistance in setting up the GMI replay simulations.

Operational Transition to the Enterprise GOES-R Rainfall Rate Algorithm

Robert J. Kuligowski, Center for Satellite Applications and Research, College Park MD
Yaping Li, I.M. Systems Group, Rockville, MD

What Does the GOES-R Rainfall Rate Provide?

- Retrievals of instantaneous rain rates..
  - …over the ABI full disk (but only validated for satellite zenith angle < 70°, latitude < 60 °)
  - …at a spatial resolution of the ABI IR bands (2 km at nadir)
  - …updated every 10 minutes (Mode 6) or 15 min (GOES-17 Mode 3)
  - …with a production delay of less than 4.5 minutes.
- Rain rates are derived from IR water vapor (WV) and window bands using relationships that are based on calibration against microwave rain rates
- The current operational algorithm will be replaced with an improved "Enterprise" version (currently expected in November 2020).

What Will Change with the Enterprise Version?

Current Operational Version (Kuligowski 2010)	Enterprise Version
Calibrated one time against NWS/CPC combined microwave (MWCOMB) data set (Joyce et al. 2004): • Discriminant analysis to select predictors and coefficients for rain / no rain discrimination. • Stepwise forward linear regression on the raining MW pixels to choose predictors and coefficients for rain rate retrieval. • Histogram matching adjusts the distribution of the retrieved rain rates to match MWCOMB	Same calibration procedure, but updated hourly to capture time variations in the relationships between the predictors and MW rain rates.
Three cloud types, based on brightness temperature differences (BTDs) between IR bands: • "Water cloud": $T_{7.34}<T_{11.2}$ and $T_{8.5}-T_{11.2}<-0.3$ K • "Ice cloud": $T_{7.34}<T_{11.2}$ and $T_{8.5}-T_{11.2}\geq-0.3$ K • "Cold-top convective cloud": $T_{7.34}\geq T_{11.2}$	Fourth cloud type added for when the GOES-17 ABI Focal Plane Module (FPM) heats up. For this "type", only band 14 (11.2 μm) and derived parameters is used. The reason: BTDs from the GOES-17 ABI are very noisy even when the FPM is relatively cool.
Separate calibrations for 30° latitude bands to account for spatial variability in rainfall climatology.	Smaller 15x15° lat / lon calibration regions better account for spatial variability in rainfall climatology. (Kuligowski et al. 2016)
Eight possible predictors, selected empirically from all possible ABI IR channels and channel differences; each predictor regressed against MW rain rates in log-log space to produce eight additional nonlinearly transformed predictors.	Added band 14 and its nonlinear transformation to the predictor list for all classes.
No adjustment evaporation of precipitation below cloud bottom.	Adjusts for evaporation of precipitation below cloud bottom using relative humidity (RH) values from the GFS. (Kuligowski et al. 2016)
No parallax adjustment.	Adjusts for parallax based on cloud-top heights derived by comparing limb-adjusted band 14 brightness temperatures to GFS temperature-height profiles.

DISCLAIMER: The contents of this poster are solely the opinions of the authors and do not constitute a statement of policy, decision, or position on behalf of NOAA or the U.S. Government.

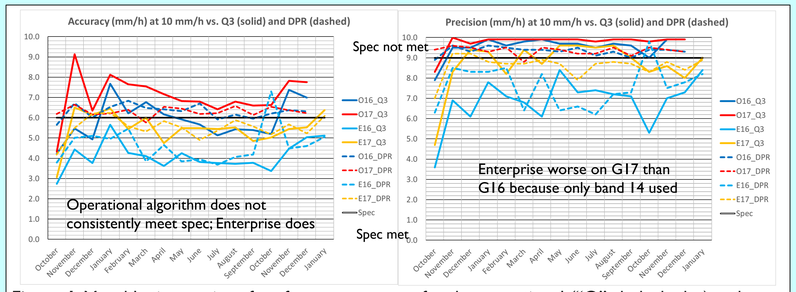

Figure 1. Monthly time series of performance vs. spec for the operational ("O", dark shades) and Enterprise ("E", light shades) rain rates vs. MRMS Q3 (solid lines) and GPM DPR (dashed lines) for GOES-16 and -17 from October 2018 – January 2020. Accuracy is mean error for retrieved rates of 10 mm/h; precision is 68th percentile of error for retrieved rates of 10 mm/h.

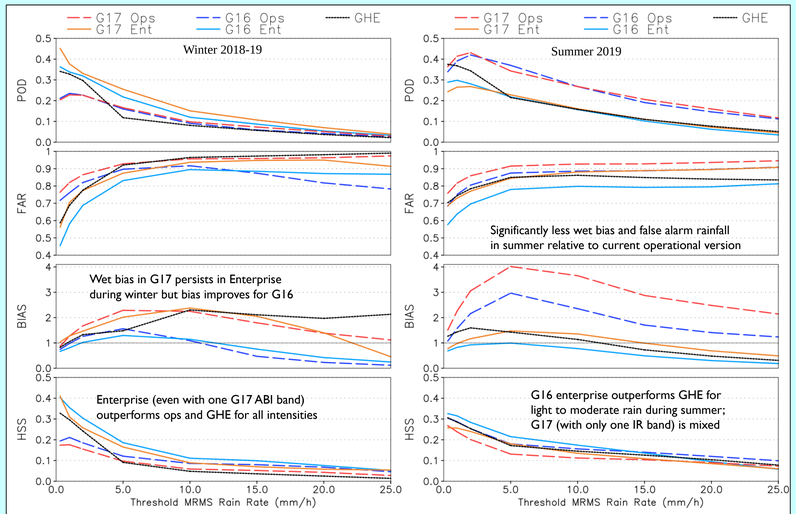

Figure 2. Probability of Detection (POD), False Alarm Rate (FAR), area bias ratio (BIAS), and Heidke Skill Score (HSS) vs. MRMS Q3 for the operational ("Ops") and Enterprise ("Ent") versions of the algorithm compared to the current operational Global Hydro-Estimator ("GHE") for DJF 2018-19 (left) and JJA (right) 2019.

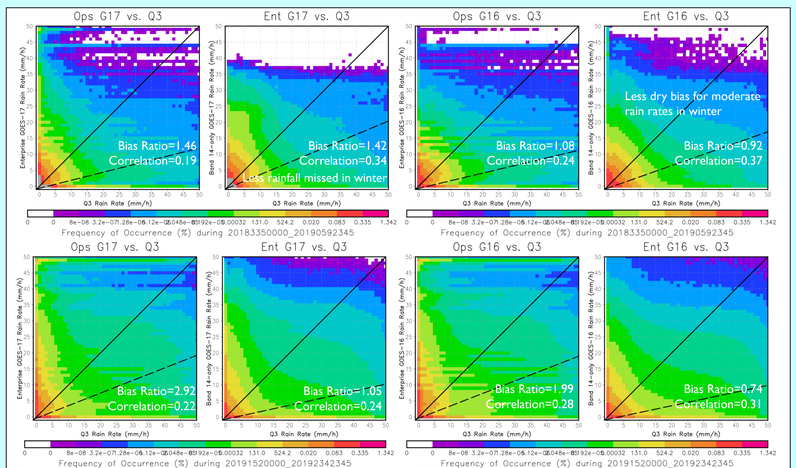

Figure 3. Scatterplots of instantaneous rain rate vs. MRMS Q3 for the operational ("Ops") and Enterprise ("Ent") rain rates for GOES-17 (left) and GOES-16 (right) for DJF 2018-19 and JJA 2019 (bottom). The dashed line is the best-fit regression line; the solid line is the 1:1 line.

Is the Enterprise Version Better?

- The algorithms are being validated against gauge-adjusted Multi-Radar Multi-Sensor (MRMS) Q3 over the CONUS and against Global Precipitation Measurement (GPM) Dual-frequency Precipitation Radar (DPR) over the full disk.
- The operational algorithm does not meet spec, but the Enterprise version consistently does for GOES-16 and mostly does for GOES-17 despite using only band 14 (Fig. 1).
- The Enterprise algorithm improves over the current operational version and the previous-generation Global Hydro-Estimator (GHE), particularly during the cool season (Fig. 2) and especially for GOES-16.
- Using only band 14 on GOES-17 degrades performance somewhat relative to GOES-16, particularly in the form of a strong wet bias for moderate to heavy precipitation during the cool season (Fig. 2).
- Rain rates from the Enterprise algorithm have better correlation and generally less bias than the current operational version (Fig. 3).

What Happens Next?

- Lightning (GLM) data will be added to improve the depiction of convective cores that are obscured by cirrus anvils.
- The matches between the IR and MW rain rates will be improved by using individual MW rain rate swaths in place of MWCOMB, which will allow the MW rain rates to be adjusted for parallax and allow closer matches in time with ABI IR.
- The RH adjustment will be improved--it currently reduces moderate to heavy rain rates too much (Figs. 2 and 3).
- The algorithm may start using at lease some fixed, AI-based calibration if it significantly outperforms the current calibration(see poster #8 next door)
- Will continue trying to develop / incorporate an adjustment with orography. However, existing schemes generally degrade skill because the enhanced / reduced rain rates are in the wrong places when validated at fine scales.

Who Paid for All This?

This work was supported by the GOES-R Program Office.

Whose Work Did We Cite Here?

Joyce, R. J. et al., 2004: CMORPH: A method that produces global precipitation estimates from passive microwave and infrared data at high spatial and temporal resolution. *J. Hydrometeor.*, **5**, 487-503.

Kuligowski, R. J., 2010: *GOES-R Advanced Baseline Imager (ABI) Algorithm Theoretical Basis Document for Rainfall Rate (QPE)*. Available at https://www.star.nesdis.noaa.gov/goesr/documents/ATBDs/Baseline/ATBD_GOES-R_Rainrate_v2.6_Oct2013.pdf

-----, Y. Li, Y. Hao, and Y. Zhang, 2016: Improvements to the GOES-R Rainfall Rate algorithm. *J. Hydrometeor.*, **17**, 1693-1704.

Enhancement to the JPSS Snowfall Rate Product

Huan Meng[1,2] (Huan.Meng@noaa.gov), Jun Dong[2], Yalei You[2], Cezar Kongoli[2], Ralph Ferraro[1,2], Banghua Yan[1], Limin Zhao[3]
[1]NOAA/NESDIS/STAR; [2]ESSIC/CISESS/University of Maryland; [3]NOAA/NESDIS/OSPO

Introduction

The NESDIS operational Snowfall Rate (SFR) product is retrieved from measurements from passive microwave sensors aboard polar-orbiting satellites (Meng *et al.*, 2017; Kongoli *et al*., 2015, 2018).

- **Sensors**: **ATMS**, AMSU/MHS, GMI, and SSMIS
- **Satellites**: **S-NPP, JPSS**, POES, Metop, GPM, and DMSP
- **Coverage**: Global land
- **Near real-time production from 10 satellites**; 20 snowfall rate estimates per day on average in mid-latitudes and more in high latitudes
- **Algorithm**:
  - ✓ Logistic regression model for snowfall detection
  - ✓ 1 DVAR-based snowfall rate retrieval

Bias Correction

- **Bias sources**

✓Uncertainties with radiative transfer model
✓Biases from NWP model predictions
✓Algorithm assumptions, e.g. ice water content profile follows linear distribution

- **Correction approach**

✓'Truth': Stage IV hourly radar and gauge combined precipitation analysis
✓Previous correction: histogram matching
✓New approach: Regression between SFR bias and a selected set of Tbs, retrieved parameters, and GFS predictions.

• Ferraro, R., H. Meng, B. Zavodsky, S. Kusselson, D. Kann, B. Guyer, A. Jacobs, S. Perfater, M. Folmer, J. Dong, C. Kongoli, B. Yan, N. Wang, and L. Zhao, 2018. Snowfall rates from satellite data help weather forecasters, Eos, 99, https://doi.org/10.1029/2018EO096715.

• Kongoli, C., H. Meng, J. Dong and R. Ferraro, 2018. A Hybrid snowfall detection method from satellite passive microwave measurements and global weather forecast models, Quarterly Journal of Royal meteorological Society, 144(S1), 120-132, DOI:10.2002/qj3270.

• Kongoli, C., H.Meng, J. Dong and R. Ferraro. 2015. A Snowfall detection algorithm over land utilizing high-frequency passive microwave measurements – Application to ATMS. *J. Geophys. Res. – Atmospheres*, 120(5), 1918-1932. DOI: 10.1002/2014JD022427.

• Meng, H., J., Dong, R., Ferraro, B., Yan, L., Zhao, C., Kongoli, N.-Y., Wang, and B., Zavodsky (2017), A 1DVAR-based snowfall rate retrieval algorithm for passive microwave radiometers, J. Geophys. Res. Atmos., 122, doi:10.1002/2016JD026325.

The support from the JPSS Proving Ground and Risk Reduction and NOAA/NESDIS/STAR JPSS was crucial to the development of the ATMS SFR algorithm. This research has been supported by NOAA and the JPSS Program through grant NA09NES4400006 (Cooperative Institute for Climate and Satellites-CICS) at the University of Maryland, Earth System Science Interdisciplinary Center (ESSIC). The views, opinions, and findings contained in this report are those of the authors and should not be construed as an official National Oceanic and Atmospheric Administration or U.S. Government position, policy, or decision.

S-NPP Bias Correction

Regression

Correlation Coeff.	0.71
Accuracy (mm/hr)	-0.04
Precision (mm/hr)	0.44

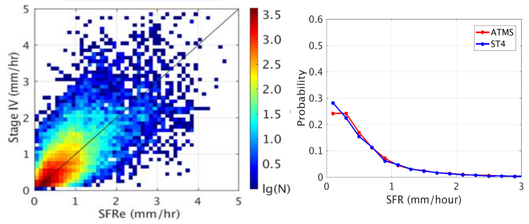

Histogram Matching

Correlation Coeff.	0.52
Accuracy (mm/hr)	-0.15
Precision (mm/hr)	0.63

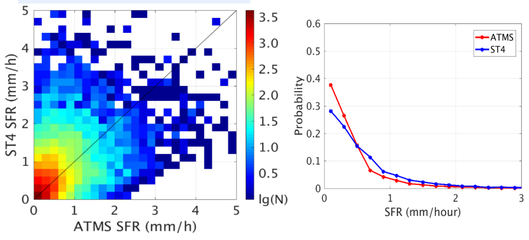

NOAA-20 Bias Correction

Regression

Correlation Coeff.	0.70
Accuracy (mm/hr)	-0.04
Precision (mm/hr)	0.48

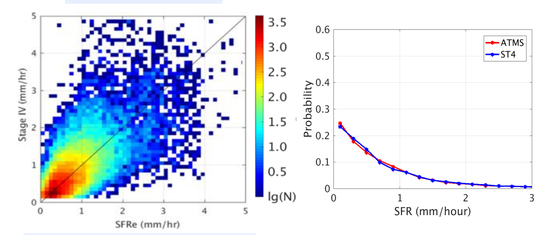

Histogram Matching

Correlation Coeff.	0.49
Accuracy (mm/hr)	-0.26
Precision (mm/hr)	0.84

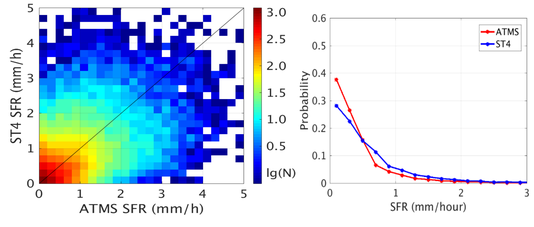

SFR over Ocean/Coast/Sea Ice

- **JPSS PGRR project**

✓Develop S-NPP and NOAA-20 SFR over ocean/coast/sea ice

- **Same algorithm framework as land SFR**

✓Logistic regression trained Snowfall Detection
✓1DVAR-based Snowfall Rate

- **Truth' data: snowfall rate from Spaceborne radars**

✓CloudSat CPR
✓GPM DPR

- **Snowfall Detection models have been developed**

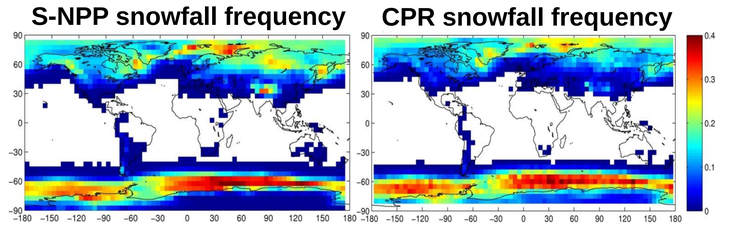

Snowfall Probability

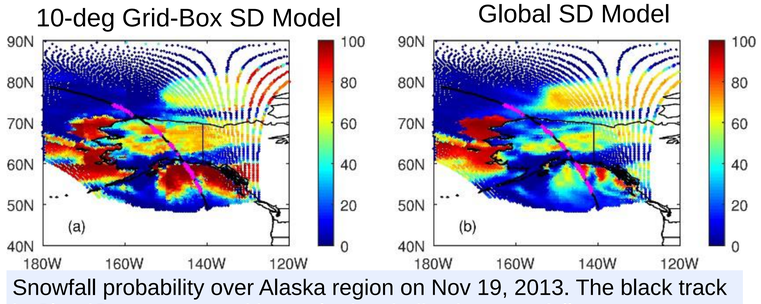

Snowfall probability over Alaska region on Nov 19, 2013. The black track is CloudSat overpass with purple dots indicating snowfall occurrences.

Northeast Snowstorm on February 7, 2020

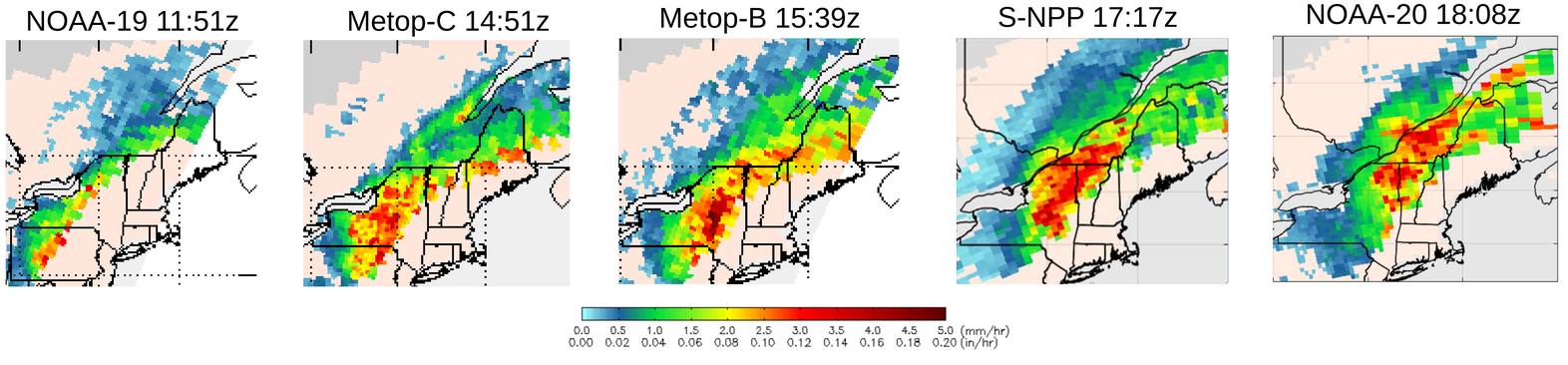

The CIRA Advected Layer Precipitable Water (ALPW) Product and Applications to Help Forecast Hazardous Precipitation Events

Sheldon J. Kusselson[1],John M. Forsythe[1], Stanley Q. Kidder[1], Andrew S. Jones[1], Ed Szoke[1], Dan Bikos[1], Chris Gitro[2], Michael Jurewicz[2] and Dan Leins[2]

[1]*Cooperative Institute for Research in the Atmosphere, Colorado State* [2]*NOAA/NWS*

CIRA ALPW products are currently produced hourly and distributed to 23 NWS WFO's and NWS/NCEP NHC, WPC, OPC and NESDIS SAB. Satellite inputs currently are S-NPP, NOAA-19/20, MetOp-A/B, and DMSP F17/18 MiRS Retrievals

John.Forsythe@colostate.edu

View near-realtime animations at: http://cat.cira.colostate.edu/sport/layered/advected/LPW_alt.htm

Sheldon.Kusselson@colostate.edu

What Do Forecasters Currently Use Operationally to Analyze Water Vapor?

Analyzing the distribution of water vapor from observations is a key component of the forecast cycle. Both integrated (total precipitable water - TPW) and vertically resolved fields are necessary, depending on the particular forecast challenge. Typically, National Weather Service (NWS) forecasters rely on a few standard tools for this task. There are currently no observing systems within the NWS region of responsibility that provide hourly, vertically resolved, land and ocean, clear and cloudy sky moisture soundings for weather forecasting. A 4-D water vapor product can be applied to many forecasting problems. It can be used to assess the depth of an "atmospheric river" of moisture to determine how much of it will make it over coastal mountains to affect the Cascades of Washington and Oregon or Sierra Nevada of California. A favorable amount of mid-level moisture can be the difference between just an ordinary heavy precipitation event and an extraordinary or historic event, like seen twice since 2016 around Ellicott City, MD. Upper level moisture above 500 hPa can also be useful to predict whether cirrus clouds will form or persist and impact high or low temperature forecasts. An experimental Advected Layered Precipitable Water Vapor (ALPW) product supported by the JPSS Proving Ground is assisting forecasters in this process.

Blended, layered water vapor products fill a void in observations to provide vertical structure

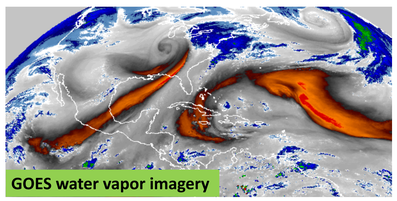

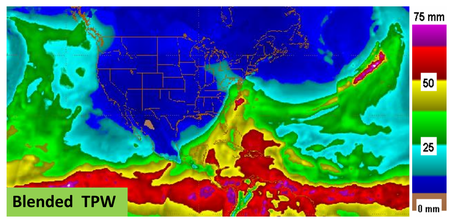

NOAA OFFICE OF SATELLITE AND PRODUCT OPERATIONS — 1800 UTC 15 November 2018

How is the Blended ALPW Product Created?

Satellite inputs currently are Suomi-NPP, NOAA-19/20, MetOp-A/B, and DMSP F17/18 MiRS Retrievals

Local equator crossing times, periods of high and low sampling

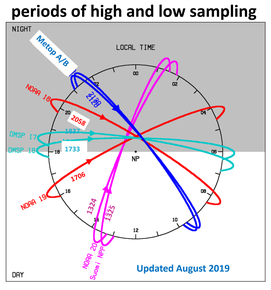

- Water Vapor profiles created by the NOAA operational Microwave Integrated Retrieval System (MiRS) retrievals from seven spacecraft received at CIRA. Typical latency is 1.5 to 3 hours.
- Four layers of precipitable water created (surface-850, 850-700, 700-500 , and 500-300 hPa).
- Advection of satellite moisture based on GFS model winds to shorten latency and smooth features.
- Satellites overlaid every three hours (36h loop) and every hour (12h loop) in a revolving composite to create animations.
- Product routed in AWIPS-2 and N-AWIPS format to 23 NWS WFOs, WPC via CIRA and SAB, NHC via NASA SPoRT (thank you!).

CIRA Blended Advected Layered Precipitable Water (ALPW) for 1800 UTC 15 November 2018

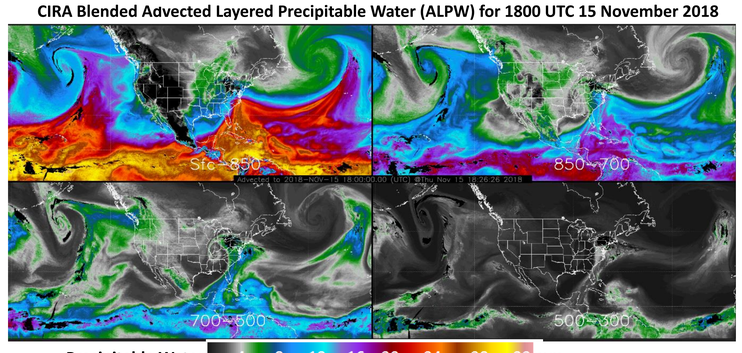

Training Forecasters on Use of Blended TPW and ALPW With Reinforcing Case Study Examples

The Virtual Institute for Satellite Integration Training (VISIT) is a joint effort involving NOAA/NESDIS Cooperative Institutes (e.g. CIRA, CIMSS), the National Environmental Satellite Data and Information Service (NESDIS) and the National Weather Service (NWS). The primary mission of VISIT is to accelerate the transfer of research results based on atmospheric sensing into NWS operations through distant education techniques. Everybody, including those outside government, can take part in the learning here. Many have taken part in both the live and online "ALPW Product" training at: *http://rammb.cira.colostate.edu/training/visit/training_sessions/advected_layer_precipitable_water_product/* . Many hazardous weather case study events are presented during these sessions, so forecasters can understand the products and how to use them. Reinforcing case studies examples using applications have also been well received. A few cases are provided below.

Ellicott City, Maryland Flood #1 (July 2016)

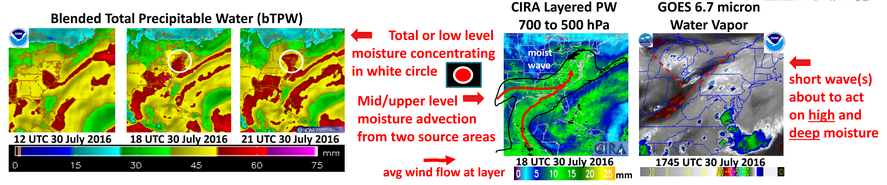

Ellicott City, Maryland Flood #2 (May 2018)

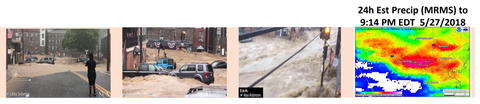

CIRA Experimental Advected Layered Precipitable Water for 18 UTC 27 May 2018

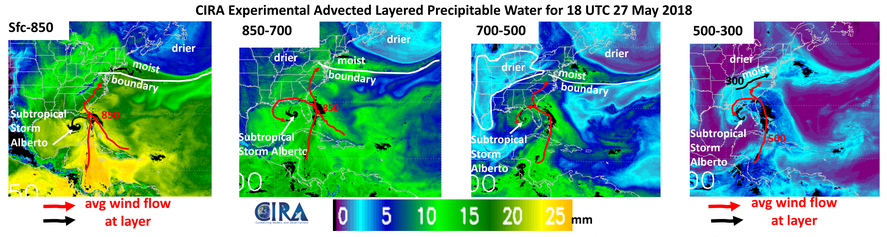

A relatively high concentration of moisture at 4 layers from Subtropical Storm Alberto into the Southeast U.S. Some of the same high moisture was also interacting with an analyzed boundary/front (west to east oriented concentration of higher moisture) to help produce a second 1000-year flood in three years in Ellicott City, Maryland.

Social Media – Use of Blended TPW and Advected Layered Precipitable Water in DC Area

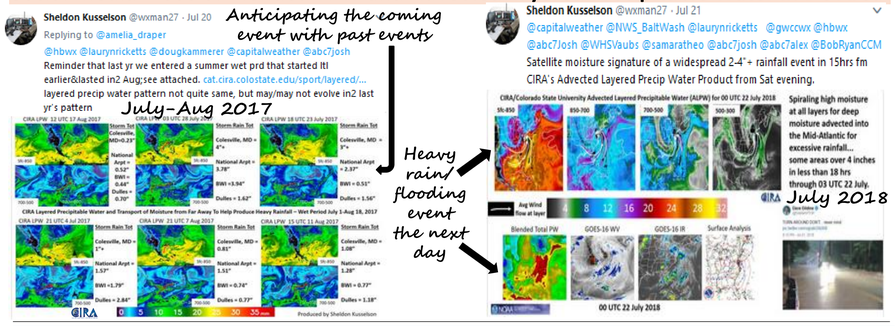

Five streams of tropical moisture, including one from a tropical storm, being transported to the Northeast U.S. and fueling heavy rain and flood potential

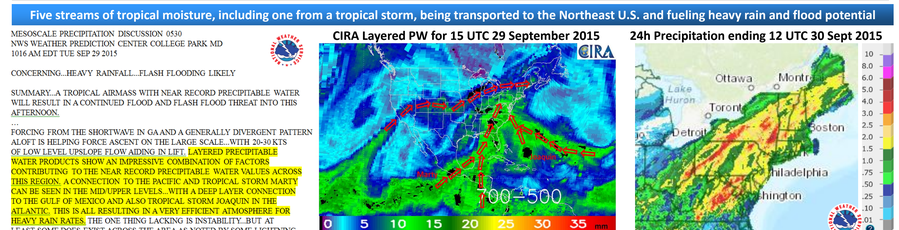

What Research is in Progress?

- Comparison of the ALPW to coincident radiosondes
- Comparison of HRRR model derived 3 hour forecast LPW to ALPW
  - Evaluated at the WPC FFaIR experiment in summer 2019
- Adding new geographic regions, such as the South America sector shown below and used by the NCEP WPC International desk.

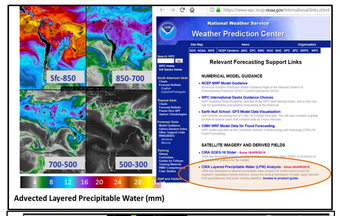

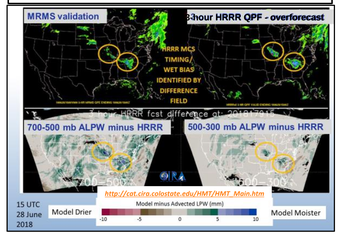

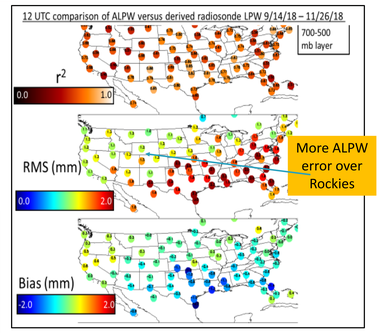

Can ALPW be used to tell whether the model is too moist or dry? Is this reflected in QPF?

from 2018 FFaIR experiment at WPC

Summary:

- The ALPW product is widely used by forecasters to track long-distance transport of water vapor which can be a precursor to heavy precipitation and flooding. Commonly used in WPC Mesoscale Precipitation Discussions.
- ALPW is independent of the model moisture fields and thus can be used for comparison to models. Work in progress to see if this is useful for QPF.
- A lead forecaster at NWS WFO Tucson mentioned, "we look at the ALPW product religiously, especially during the Southwest Monsoon season".
- Another WPC forecaster said, "I always value the ALPW when it comes to diagnosing eastern tropical Pacific mid/upper level moisture tongues that lift northeast across the central/southern Plains and Midwest. These streams of enhanced moisture can play key seeder-feeder roles in rainfall efficiency of mid-latitude convection well east of the Continental Divide, and will definitely alter the static stability of the vertical column".
- WPC forecaster looks at the 700-500 ALPW for narrow PW plumes at that layer; he mentioned, "you don't need as much CAPE/instability to get good convection over an area on downwind side of 700-500 moisture plume".
- CIRA and CIMSS are working on adding advection technology and GOES-TPW data to the operational blended TPW product (from Sheldon Kusselson's Wednesday morning NWA talk). If ALPW becomes operational, it will give forecasters a consistent set of satellite-derived water vapor analysis tools.

More details:

Forsythe, J. M., S. Q. Kidder, K. K. Fuell, A. LeRoy, G. J. Jedlovec, and A. S. Jones, 2015: A multisensor, blended, layered water vapor product for weather analysis and forecasting. NWA Journal of Operational Meteor., Vol. 3, No. 5, 41- 58.

LeRoy, A., K. K. Fuell, A. L. Molthan, G. J. Jedlovec, J. M. Forsythe, S. Q. Kidder, and A. S. Jones, 2016: The operational use and assessment of a layered precipitable water product for weather forecasting. NWA J. Operational Meteor., Vol. 4, No. 2, 22-33.

Gitro, C. M., M. L. Jurewicz, S. J. Kusselson, J. M. Forsythe, S. Q. Kidder, E. J. Szoke, D. Bikos, A. S. Jones, C. M. Gravelle, C. Grassotti, 2018: Using the multisensory advected layered precipitable water product in the operational forecast environment: NWA Journal of Operational Meteor., Vol. 6, No. 6, 59-73.

VISIT Advected Layered PW Training at: http://rammb.cira.colostate.edu/training/visit/training_sessions/advected_layer_precipitable_water_product/ .

National Weather Association Monthly (November, 2018) Webinar titled, "Using the Multisensor Advected Layered Precipitable Water Product in the Operational Forecast Environment" at: https://bit.ly/2P5mbSZ .

This work is supported by the NOAA JPSS Proving Ground and Risk Reduction Program and the NOAA Hydrometeorology Testbed, Office of Water and Air Quality under grant NA17OAR4590121.

Updates on the JPSS Infused 2nd Generation CMORPH

Pingping Xie[a], Robert Joyce[b], Shaorong Wu[b], and Bert Katz [b]

[a]NOAA/NCEP/CPC, College Park, MD

[b]NOAA/NCEP/CPC, INNOVIM , Greenbelt, MD

Introduction

A system has been developed at NOAA Climate Prediction Center (CPC) to produce 2nd generation CMORPH (CMORPH2) integrated high-resolution satellite precipitation estimates on a 0.05°lat/lon grid covering the entire globe from pole to pole. The CMORPH2 is built upon the Kalman Filter based integration algorithm of Joyce and Xie (2011). First, retrievals of instantaneous precipitation rates from passive microwave (PMW) observations aboard low earth orbit (LEO) satellites derived from SNPP and ~10 other passive microwave (PMW) sensors are decoded and mapped onto a 0.05°lat/lon grid over the globe. The mapped PMW retrievals are then calibrated utilizing a PDF matching technique against a reference field. In particular, snowfall rate retrievals of Meng et al. (2011) are utilized to capture the cold season precipitation. Precipitation estimation is derived from infrared (IR) window channels aboard the low earth orbit (LEO) satellites to fill in the gaps of PMW observations. The above mentioned retrievals of instantaneous precipitation rates are combined into a single gridded field called APCOMB. These instantaneous precipitation rates are then propagated from their respective observation times to the target analysis time along the motion vectors of the precipitating clouds. The motion vectors are computed through comparing the precipitation fields of two consecutive time steps as depicted by the 30-min precipitation estimates derived from the geostationary IR images and the NCEP/GFS hourly precipitation forecasts. The propagation is performed in both the forward and backward directions and the weighted mean of the forward and backward propagated APCOMB is defined as the CMORPH total precipitation estimates, with the weights set as a function of sensor type, length of propagation time, season, and location. Fraction of solid precipitation is then computed from the surface air temperature with the algorithm of Sims and Liu (2015).

- **Introduce the current status of second generation CMORPH**
- **Illustrate examination results for the real-time production of the 2nd generation CMORPH**

Overview of PTP 2nd generation CMORPH

- Pole to Pole Complete Global Coverage
  - *90°S-90°N*
  - *0.05° lat/lon*
- Improved Representation of Cold Season Precipitation
  - *New Versions of PMW retrievals (MiRS et al)*
  - *PMW Snowfall Rate (SFR) retrievals (STAR/Huan Meng)*
  - *LEO IR based precipitation estimates (in-house)*
- Strategy
  - *Combining information from > 15 geostationary and low earth orbit satellites*
  - *Kalman filter based objective technique*

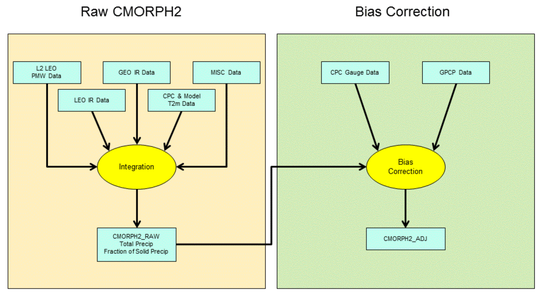

- Greatly refined integration algorithm at NOAA/CPC
  - *Inter-satellite calibration algorithm*
  - *Precipitation motion vectors*
  - *Kalman Filter analysis framework*
- Improved input satellite retrievals of rainfall and snowfall from NASA and NESDIS/STAR
- Satellite IR based precipitation estimates developed / refined at NOAA/CPC
- Newly added technique to determine fraction of solid precipitation from surface meteorology (T_{2m} et al) through collaboration with FSU
  - *Global hourly T_{2m} analysis*

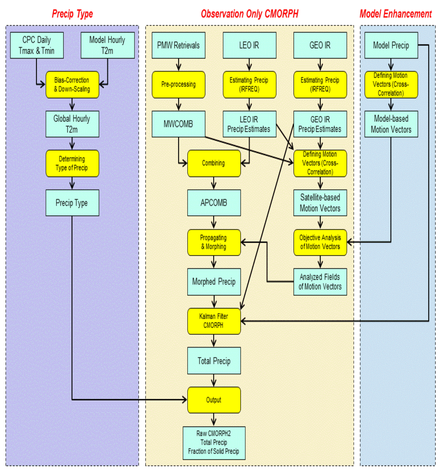

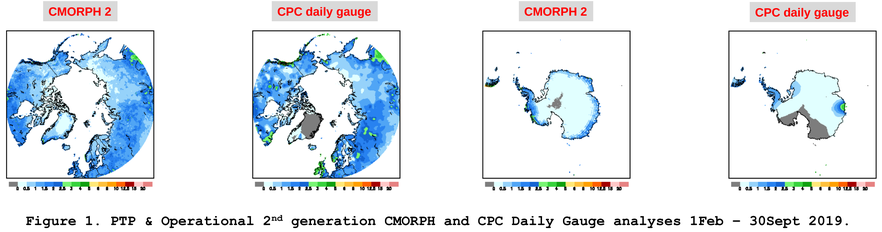

Figure 1. PTP & Operational 2nd generation CMORPH and CPC Daily Gauge analyses 1Feb – 30Sept 2019.

Evaluation of 2nd generation CMORPH

- **Higher relative skill for 2nd generation CMORPH**
- **CMORPH2/IMERG has negative/positive bias over winter hemisphere**

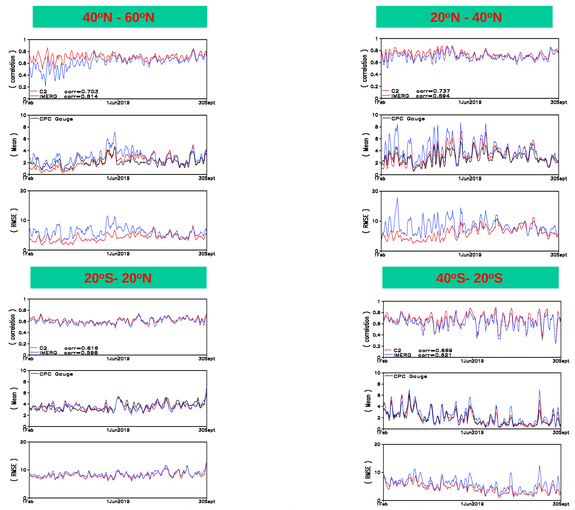

Figure 2. PTP, operational 2nd generation CMORPH [red], IMERG (late run V06B.RT) [blue], with CPC Daily Gauge analyses 1Feb – 30Sept 2019, 40N-60N [upper left], 20N-40N [upper right], 20S-20N [lower left], 40S-20S lower right. Correlation/mean/RMSE top/middle/bottom panels.

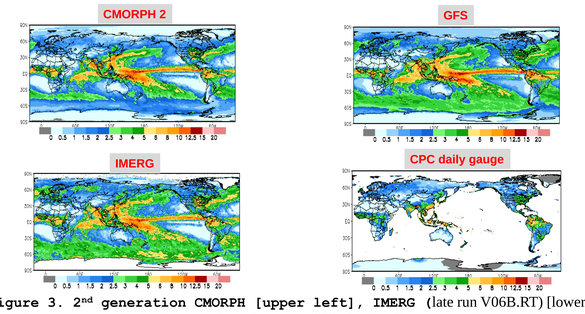

Figure 3. 2nd generation CMORPH [upper left], IMERG (late run V06B.RT) [lower left], GFS model precipitation [upper left], and CPC Daily Gauge analyses [lower right] 1Feb – 30Sept 2019 [mm/day].

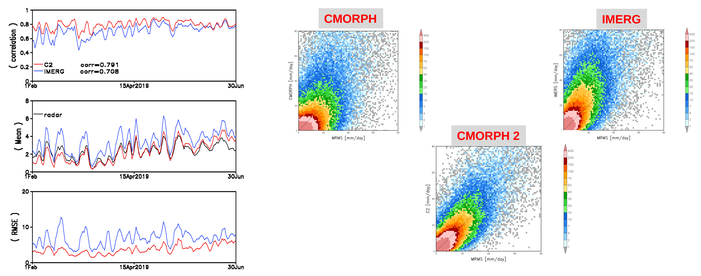

Figure 4. PTP, operational 2nd generation CMORPH [red], IMERG (late run V06B.RT) [blue], compared with gauge corrected MRMS 1Feb – 30June 2019, Correlation [upper left], Mean [middle left], RMSE [lower left].

Evaluating CMORPH at multiple near real time delay production latencies over CONUS

CMORPH2 Real-Time Production Improves with Production Latency but Maintains Good Quantitative Consistency among Productions of Different Latencies

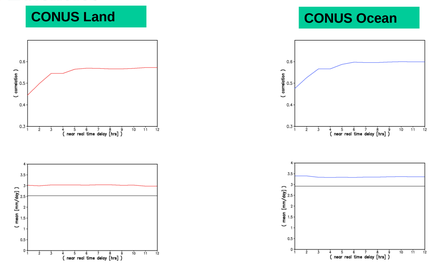

Figure 5: Comparison of the real-time 2nd generation CMORPH generated at various latency levels against the MRMS radar precipitation July, 2019, over CONUS land (left) and adjacent oceans (right) Comparisons are conducted for hourly precipitation on a 0.25°lat/lon grid box. Top and bottom panels show correlation and mean precipitation, respectively. Black line in the bottom panels are radar precipitation.

Daily precipitation (mm)

for 23 February, 2019

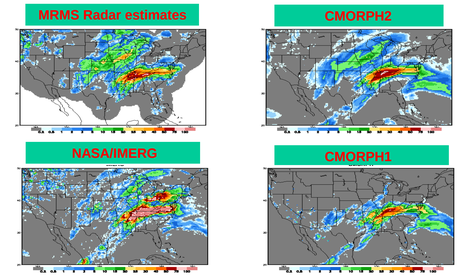

Figure 6. 2nd generation CMORPH [upper right], IMERG (late run V06B.RT) [lower left], gauge corrected MRMS [upper left], and original CMORPH [lower right] 23 Feb 2019 [mm/day].

CONCLUSIONS AND REFERENCES

- **PTP CMORPH in beta mode since 1 May 2017, frozen algorithm version since Jan 2019**
- **2nd generation CMORPH precipitation estimation and gauge reports generally agree over high latitude, Arctic, and Antarctica regions**
- **C2 more skill than IMERG relative to both CPC daily gauge and MRMS especially during winter mid and high latitudes, however very similar in skill and mean over the Tropics**
- **C2/IMERG had an under/over estimation in the Northern Hemisphere winter relative to both gauge and radar, and an under/over estimation over high-latitude ocean relative to GFS**
- **CMORPH correlation increases significantly from the 1 to 3 hour near real time latencies**
- **Infusion of Level 2 precipitation retrievals from JPSS plays important role in improving the CMORPH especially for the representation of snowfall rate (SFR).**

Probabilistic Precipitation Estimates from GOES-R for Hydrological Applications

Shruti Upadhyaya[1], Pierre-Emmanuel Kirstetter[2,3,4,5] , Jonathan Gourley[5]

[1] Cooperative Institute for Mesoscale Meteorological Studies, Norman, Oklahoma; [2] School of Meteorology, University of Oklahoma, Norman, Oklahoma
[3] School of Civil Engineering and Environmental Science, University of Oklahoma, Norman, Oklahoma; [4] Advanced Radar Research Center, University of Oklahoma, Norman, Oklahoma
[5] NOAA/National Severe Storms Laboratory, Norman, Oklahoma

Email: shruti.a.upadhyaya-1@ou.edu, pierre.kirstetter@noaa.gov, bob.kuligowski@noaa.gov, jj.gourley@noaa.gov

1. Introduction

Goal: To derive unified, consistent, accurate and fine-resolution precipitation rates over the Conterminous U.S., by leveraging GOES-R satellite observations and ground-radar based precipitation product from the Multi-Radar/Multi-Sensor (MRMS) system.

Specific Objective: To investigate the potential for improving precipitation estimation using multi-spectral data from the GOES-R satellite w.r.t. deterministic retrieval algorithms such as SCaMPR (Kuligowski et al. 2016).

Advanced Baseline Imager (ABI) on GOES-R satellite: Views Earth with three times more spectral channels (16) , four times the resolution (~ 2km), and five times faster scanning (5min across Conterminous U.S.) compared to its predecessor IMAGER on GOES 12-15.

Challenge: To effectively mine GOES-R "big data" observations for precipitation and document relations between multi-spectral ABI observations and MRMS surface precipitation estimates. `

2. Self-Calibrating Multivariate Precipitation Retrieval (SCaMPR) : NOAA's Operational Precipitation Algorithm for GOES-R satellite (Kuligowski et al. 2016)

I. SCaMPR Predictors derived from GOES-R

*T6.19 (WV)	T8.5-T7.34 (IR-WV)
S=0.568-(Tmin,11.2) (Texture)	T11.2-T7.34 (IR-WV)
Tavg,11.2-Tmin,11.2-S (Texture)	T8.5-T11.2 (IR-IR)
T7.34-T6.19 (WV-WV)	T11.2-T12.3 (IR-IR)

IR: Infrared spectral band **WV:** Water Vapor absorption band
***T6.19:** Brightness temperature observed in the ABI band at wavelength 6.19μm
Tavg,11.2: Average value of T11.2 across 5x5 pixel
Tmin,11.2: Minimum T11.2 over the closest six neighboring pixels

II. Stages in SCaMPR

- Cloud Type **Classification** (Deterministic)
  - **Type 1 (Ice Cloud):** T7.34<T11.2 and T8.5-T11.2<-0.3
  - **Type 2 (Water Cloud):** T7.34<T11.2 and T8.5-T11.2≥-0.3
  - **Type 3 (cold-top convective cloud):** T7.34≥T11.2
- Rain/No-Rain **Detection** (Deterministic) → Using Discriminant Analysis
- Precipitation **Quantification** (Deterministic) → Using Multiple Linear Regression
- Post Processing → E.g. Bias Correction, Relative Humidity Correction

III. Study Area and Dataset

- **Reference data:**
  - **SCaMPR:** CPC combined microwave (MWCOMB) dataset (Joyce et al. 2004) derived from satellite passive microwave sensors at 30min and 8km resolution
  - **Proposed: Multi-Radar/Multi-Sensor (MRMS) precipitation product at native ABI resolution**
- **Study Period:** Summer 2018
- **Study Area:** Conterminous United States (CONUS)

3. Challenges at different stages of SCaMPR

I. Classification

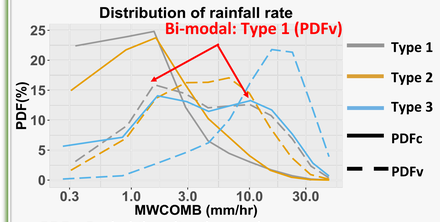

PDFc: Probability distribution by occurrence
PDFv: Probability distribution by volume

Challenge:
- **Bi-modal distribution suggests two different cloud populations in the Type 1 class of SCaMPR**
- **SCaMPR deterministic detection of precipitation and choice of channels questioned by Probability of Precipitation**

Proposed Solution: Explore more indices such as all possible difference and textures along with better reference to aid the classification (Section 4-II)

II. Detection

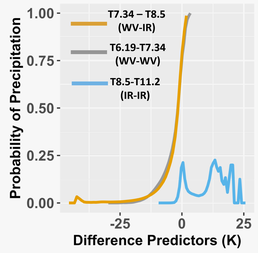

III. Quantification

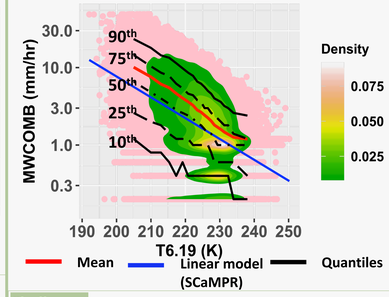

Challenge:
Precipitation retrieval requires more than just one deterministic "best estimate" and linear relation

Proposed Solution:
Probabilistic Quantitative Precipitation Estimation (PQPE)(Kirstetter et al. 2018) (Section 4-III)

4. Proposed Algorithm: Preliminary Results

I. Better Reference

- **To explore the potential of high resolution, low latency, and more spectral bands from ABI, a reference better than MWCOMB is required;**
- **High resolution, more physically based precipitation rates and types retrieved from MRMS are ideal to effectively mine data from GOES-R for precipitation retrieval**

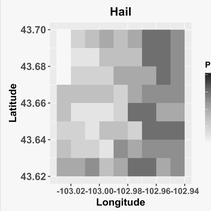

Proportion of Hail from MRMS in 30min window of MWCOMB

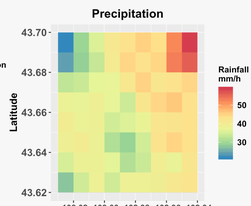

Date: 2018-07-22 04:00:00 UTC

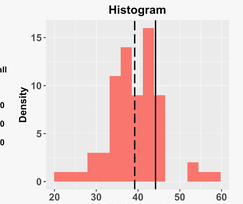

II. Detection and Classification

- **More channel combination and textures are derived: total 480 indices ;**
- **A Random Forest based Machine Learning (ML) algorithm is developed**

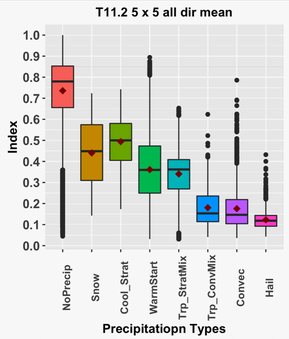

Example: Texture from ABI Spectral channel 11.2μm distribution across different MRMS precipitation types

Initial Classification and Detection results

Precipitation Type	Probability of Detection
No-Precipitation	96%
Hail	94%
Convective	69%
Tropical Convective/Mix	83%
Warm Stratiform	50%
Cool Stratiform	91%
Tropical Stratiform Mix	70%
Snow	87%

Overall Accuracy: 80%

III. Quantification: Probabilistic Quantitative Precipitation Estimation (PQPE)

PQPE Example from Kirstetter et al., 2018

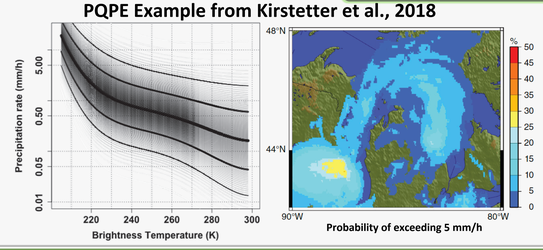

Initial Quantification Results with PQPE and its comparison with MWCOMB and SCaMPR

Statistics	MWCOMB	SCaMPR	PQPE(GOES-R)
Correlation Coefficient	0.41	0.32	0.49
Root Mean Square Error (mm/h)	5.63	4.95	4.1
Bias (mm/h)	+1.10	-0.78	+0.12
Mean Relative Error (%)	+41.5 (Overestimation)	-28.8 (Underestimation)	+3.6 (Unbiased)

5. Conclusions and Perspectives

- Challenge: the potential of high-resolution ABI data remains underutilized due to consideration of coarser scale data as reference ➔ solution: to address this issue, we are utilizing high resolution and accurate precipitation estimates from MRMS.
- Challenge: satellite precipitation has been deterministically computed despite the under-constrained relation between the satellite sensor measurements to precipitation rate. ➔ solution: preliminary results on new satellite precipitation approaches which focuses on probabilistic quantification of precipitation (Kirstetter et al. 2018) show promising results with unbiased estimates.
- Challenge: Effective utilization of high resolution (Spatial, Temporal and Spectral) GOES-R observations ➔ solution: results confirm the usefulness of GOES-R infrared and water vapor absorption bands, as well as newly derived indices for precipitation detection, classification and quantification.
- Challenge: simple unsupervised techniques are currently being used for precipitation classification ➔ solution: The detection and classification results using ML approach guided by better reference highlights the potential of GOES-R satellite observations in identifying precipitation types from ground radar i.e. MRMS system

Important References

- Kirstetter, P. E., Karbalaee, N., Hsu, K., & Hong, Y. (2018). Probabilistic precipitation rate estimates with space-based infrared sensors. Quarterly Journal of the Royal Meteorological Society, 144, 191-205.
- Kuligowski, R. J., Li, Y., Hao, Y., & Zhang, Y. (2016). Improvements to the goes-r rainfall rate algorithm. Journal of Hydrometeorology, 17(6), 1693-1704.

Acknowledgements: The work is supported through GOES-R risk reduction program
Contributor: Dr. Robert J. Kuligowski, NOAA/NESDIS/Center for Satellite Applications and Research (STAR)

Arctic Ocean as a significant source of atmospheric methane: year-round satellite data

yurganov@umbc.edu

Leonid Yurganov[1,3], Frank Muller-Karger[2], Ira Leifer[3]

Methane is a greenhouse gas, most of its sources are temperature-dependent. The Arctic is rapidly warming, methane hydrates buried in the seabed may be destabilized and liberated methane may amplify the warming further as a positive feed-back.

The question is: «ARE THE ARCTIC MARINE SOURCES IMPORTANT FOR REGIONAL AND GLOBAL METHANE BUDGETS?» **Thermal IR (TIR) sonders may help to answer this question. They are capable to supply data day-and-night, year-round in contrast to Short-Wave IR (SWIR) that require Sun light.**

METHANE IN SEAWATER AND ITS TRANSPORT TO THE TROPOSPHERE

A diagram to the right illustrates location of CH_4 sources and density stratification of the ocean **in summer.** Methane bubbles ascend from the seafloor and dissolve in the seawater en route ***(a bottom-left diagram)***. Finally, methane is consumed by bacteria in seawater. Deep layers of the Arctic seas (***right-bottom graph***) are strongly enhanced with methane but the flux to the amosphere in summer is negligible due to a blocking effect of the pycnocline with a typical mixed layer depth ~50 m.
The situation changes dramatically in late autumn. The surface layer cools, convection starts, wind mixing grows and the water column becomes well-mixed down to the seafloor. This lets methane reach the atmosphere.

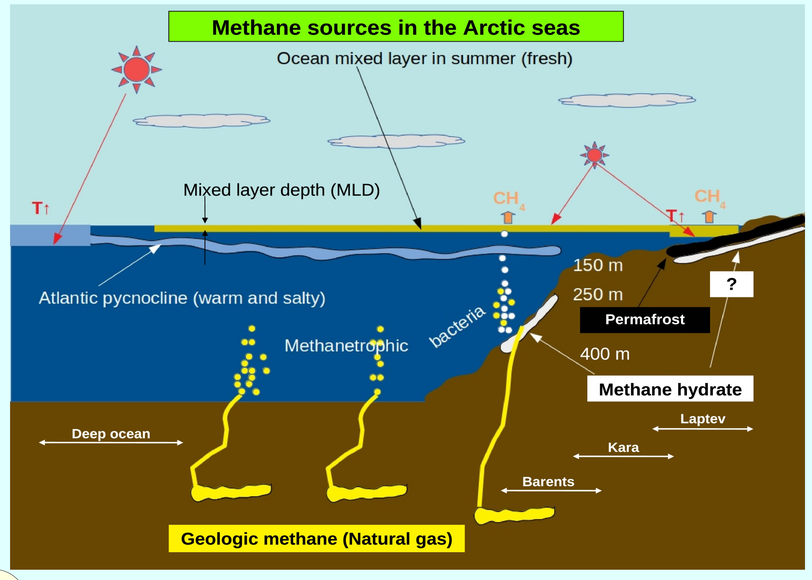

Mixed Layer Depth (MLD)
By Kara et al. (2003)
Note enhanced MLD in high latitudes of both hemispheres

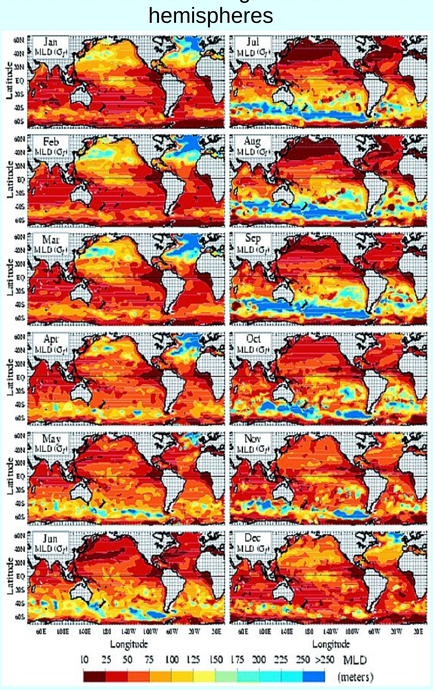

Sonars observe diminishing bubble concentration as the plume approaches the surface. By Veloso et al.(2015)

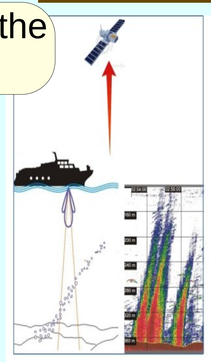

The mixed layer (see a ***top diagram***) is shallow in summer and deepens starting in October-November. Kara et al. (2003) calculated its depth (MLD) globally (below), but in the Arctic only to 65° N. MLD>250 m is estimated for high latitudes of both hemispheres. We calculated it specifically for the box #8 (***map to the right***) using the same global circulation model and compared with methane concentration measured by IASI and AIRS (below).

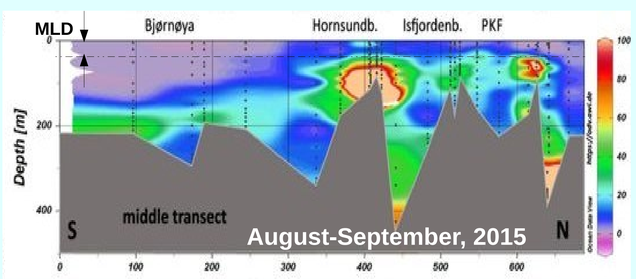

"Widespread methane seepage along continental margin off Svalbard - from Bjørnøya to Kongsfjorden" by Mau et al. (2016)

DO SATELLITES SEE INCREASED METHANE AS THE PYCNOCLINE BREAKS DOWN?

TIR sounders are sensitive to the lower troposphere

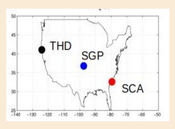

Validation of methane measured by IASI and AIRS satellite sounders versus aircraft sampling over 3 US sites.

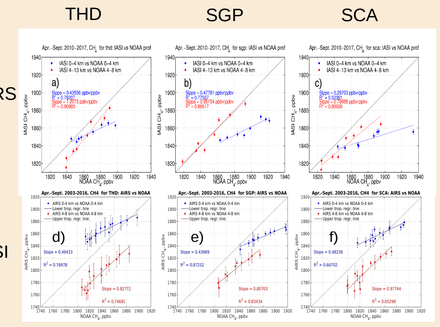

Sensitivity to 0-4 km layer is ~ 0.5. That means underestimation of real methane variations.

Monthly mean IASI methane concentrations in 2018

1. No variations over seas between May and August.
2. Spots of increased methane during autumn-winter mostly in Western Arctic.

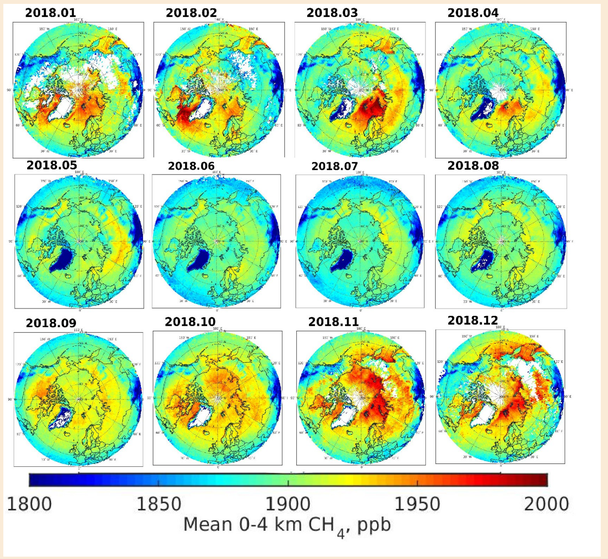

Eight boxes are selected and seasonal cycles are calculated

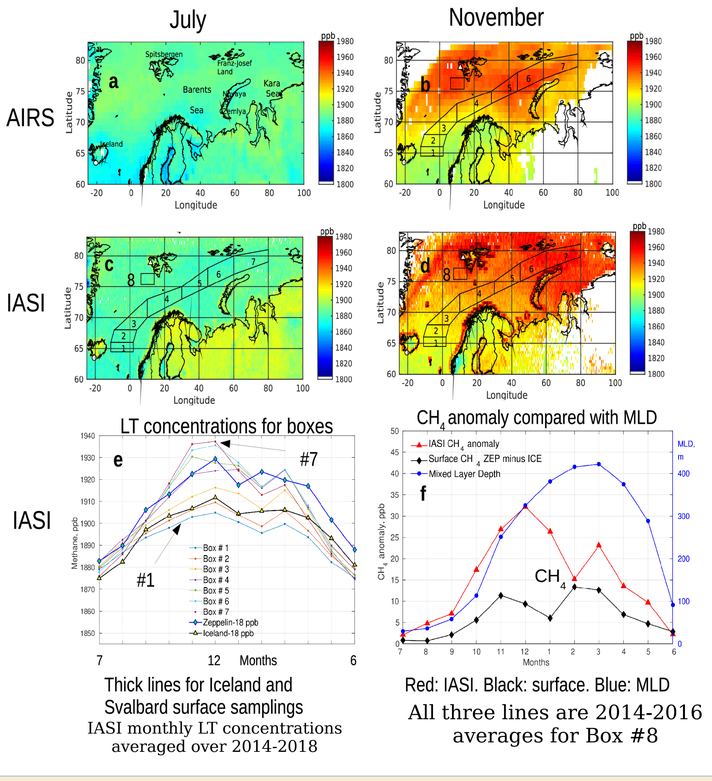

DISCUSSION AND CONCLUSIONS

Various studies have shown Arctic methane seabed emission from west Svalbard and elsewhere. However, current atmospheric methane budgets count the Arctic marine contribution as negligible; a priori it assumed as zero in reverse modeling simulations. TIR sounders AIRS and IASI clearly indicate non-negligible marine methane emissions in late autumn and winter. Yurganov et al. (2016) preliminary estimated its annual magnitude as ~2/3 of terrestrial methane emission to the North of 60° N. Existing estimates of terrestrial emission are in a range between 20 and 30 Tg/yr. Thus the current marine contribution may be in the range 15-20 Tg/yr, i.e., 3-4% of the global emissions. The amplitude of atmospheric CH_4 seasonal cycle is growing at many areas. This may be interpreted as a growing methane emission from the Arctic ocean. Much more work is necessary to investigate trends and inter-annual variability of this methane source.

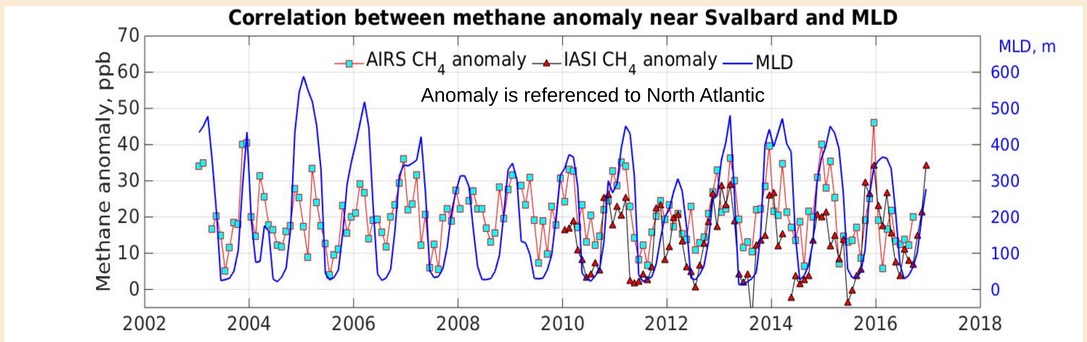

Methane anomaly referenced to the N. Atlantic background increases since October. This is explained by seawater mixing intensification and/or a breakdown of the summer pycnocline

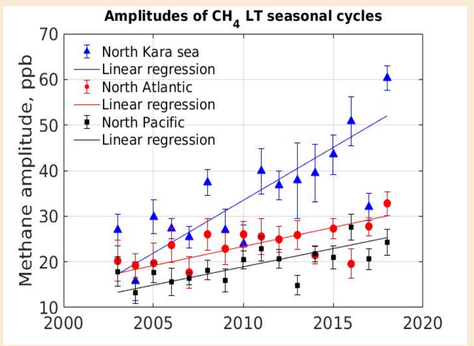

Seasonal maximum (Nov.-Dec.-Jan.) subtracted by seasonal minimum (May-June-July)

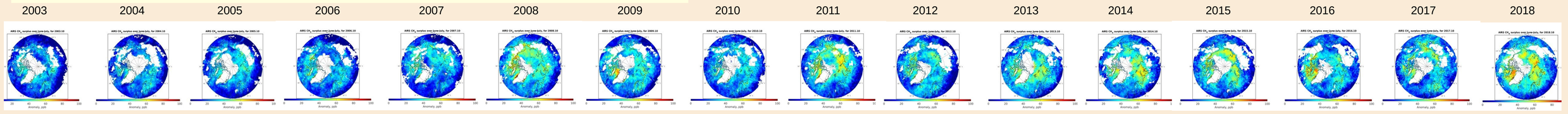

October AIRS methane concentration subtracted by the summer background for the same locations

1) University of Maryland Baltimore County,MD; 2) University of South Florida, St. Petersburg, FL.; 3) Bubbleology Research Int., Solvang, CA

NOAA Volcanic SO2 cloud measurement from SNPP and NOAA-20 using LFSO2 algorithm

Jianguo Niu[1], Lawrence Flynn[2] Trever Beck[2], Zhihua Zhang[1], Eric Beach[1]

[1]I.M. System Group Inc. @NOAA, [2]NOAA/NESDIS/STAR

Poster #19 Feb 25, 2020

Introduction

This poster presents an evaluation of the NOAA operational atmospheric SO_2 retrieval algorithm, the Linear Fit SO_2 algorithm (LFSO2). LFSO2 is used to create estimates from measurements made by the Suomi NPP (S-NPP) Ozone Mapping and Profiler Suite (OMPS). We compare the results to those from a Principal Component Analysis (PCA) algorithm applied to the same measurements. A total of 20 independent volcanic scenarios and one environmental disaster scenario over eight years of time span are selected for this comparison. More than three months of Mount Kilauea volcanic activity in 2018 are monitored and included in this comparison. We found that the current operational LFSO2 retrievals at lower troposphere (TRL), mid-troposphere (TRM), and lower stratosphere (STL) have a discontinuity and a saturation-like relationship with PCA results. The current operational LFSO2 algorithm has been investigated, and a new logic has been introduced. With this, the discontinuity and the saturation appearance in comparisons vanished and a close to linear relationship with the matchup data from the PCA retrieval products is demonstrated. The minimum detectable values for all three SO_2 layer products and the PBL products are estimated with the improved LFSO2 algorithm. Results for a volcanic cloud over Colombia for the updated LFSO2 for OMPS and a Differential Optical Absorption Spectroscopy (DOAS) algorithm for TROPOMI measurements are also compared. Similar SO_2 total mass estimates over the region are obtained from the two instruments.

Data and volcanic scenarios for comparison

Table 1 listed all data sets examined with this study. The operational NRT estimation of global SO_2 from S-NPP OMPS measurements are created by the NOAA S-NPP Data Exploitation (NDE) center. The SO_2 data records (V8TOS) are available for download starting from 24 January 2018. The LFSO2 computes total SO_2 which are assumed to be distributed in the Umkehr layers of 0, 1, 2, and 4. The NASA PCA NMSO2 data are used in this study for inter comparison with LFSO2 retrievals, and are available from the NASA GES DISC site. The SO_2 estimates from DOAS method retrieval measured by TROPOMI on board S5P are collected via the GES DISC site.

Table 1 Data related in this investigation

	platforms	Processing	methods	Source
V8TOS	S-NPP	NOAA NDE	LFSO2 (NRT)	Operational
NMSO2	S-NPP	NASA	PCA	GES DISC
NMEV-L1B	S-NPP	NASA	LFSO2 (off line)	GES DISC
TROPOMI	S5P	ESA	DOAS	Via GES DISC

Table 2 Scenarios selected for inter comparison

Event	days	Date (mm/dd/yyyy)	Volcano	SO2 Cloud height
1	1	05/08/2012	Nyiragongo, DR Congo	TRM
2	2	05/14/2012	Mauna Kea Hawaii USA	TRL
3	3	04/16/2013	Manam, New Guinea	TRM
4	4	02/14/2014	Kelut, Java, Indonesia	STL
4	5	02/16/2014	Kelut, Java, Indonesia	STL
4	6	02/17/2014	Kelut, Java, Indonesia	STL
4	7	02/18/2014	Kelut, Java, Indonesia	STL
4	8	02/19/2014	Kelut, Java, Indonesia	STL
5	9	09/01/2014	Bardarbunga, Iceland	TRL
6	10	09/27/2014	Ontake, Japan	TRM
7	11	11/24/2014	Fogo, Cape Verde Islands	TRM
7	12	11/27/2014	Fogo, Cape Verde Islands	TRM
7	13	11/28/2014	Fogo, Cape Verde Islands	TRM
8	14	04/24/2015	Calbuco, Chile	STL
8	15	04/26/2015	Calbuco, Chile	STL
9	16	12/04/2015	Etna, Sicily, Italy	TRM
10	17	03/28/2016	Pavlof Aleutian Islands, Alaska	TRM
11	18	03/08/2017	Bogoslov, Aleutian Islands, Alaska	TRM
12	19	04/21/2017	Turrialba, Costa Rica	TRL
13	20	05/17/2017	Bogoslov, Aleutian Islans, Alaska	TRM
14	21	09/05/2017	Fernandia Galapogos Islands, Ecudor	TRL
15	22	10/21/2017	Tinakula Solomon Islands	TRM
16	23	11/27/2017	Agung, Bali, Java	TRM
17	24	01/22/2018	Mayon Philippines	TRM
17	25	01/23/2018	Mayon Philippines	TRM
18	26	02/19/2018	Sinabung, Indonesia	STL
18	27	02/20/2018	Sinabung, Indonesia	STL
19	28	06/03/2018	Fuego, Guatemala	TRM
20	29	06/17/2018	Fermandian Galapagos Islands Ecuador	TRL
21	30	06/27/2019	Mosul, Iraq	PBL
21	31	06/28/2019	Mosul, Iraq	PBL

Current Operational LFSO2 vs. PCA

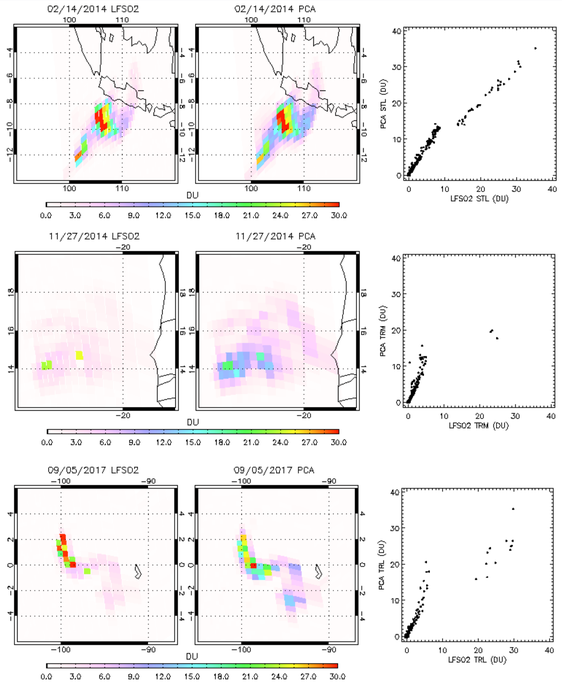

Figure 1 demonstrates the status of current operational LFSO2 product compare with the PCA products for three daily cases. The maps on the left are for LFSO2 retrievals, the maps in the middle are from PCA retrievals, and the scatter plots on the right illustrates the correlations of LFSO2 and PCA retrievals. The first row shows a case where the volcanic clouds were assumed to be distributed in Umkehr layer 4 (STL). The second row shows a case for volcanic clouds estimates for Umkehr layer 2 (TRM). The third row shows a case for the volcanic clouds estimates for Umkehr layer 1 (TRL).

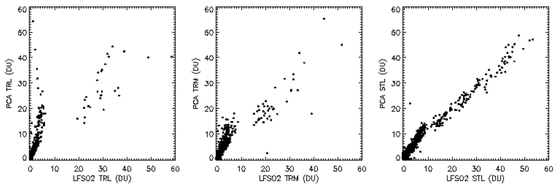

Figure 2. Comparisons between LFSO2 (in current operation) and PCA retrievals for all three volcanic SO2 cloud heights in the 29 selected scenarios in Table 2. From left to right, SO2 estimates are for TRL, TRM, and STL layers.

LFSO2 algorithm

The LFSO2 is a multi-technique combined algorithm. It contains the linear fit technique, the Band Residual Difference (BRD) technique, and the Beer-Lambert law technique. The linear fit technique in conjunction with BRD technique are used to retrieve total amount of SO_2 distributing in the TRL, TRM, and STL layers. The Beer-Lambert law is independently used to retrieve the SO_2 distributed in the boundary layer (PBL). All the three techniques in LFSO2 algorithm are based on the ozone residuals from V8TOZ EDR ozone retrieval. The linear fit technique conducts its retrieval in two steps. In the first step, the SO_2 total amount is initially estimated. In the second step, the retrieval is switched to either the linear fit or the BRD technique based on weather the first initial estimated SO_2 total amount is larger or smaller than 10 DU and on the air mass factor 4. When initial $SO_2 < 10$, the switch turns to BRD technique, otherwise it turns to the linear fit. This is the reason the scatter plots exist discontinuity and a saturation like relation with PCA.

Improvement of LFSO2 Linear Fit technique

Based on the algorithm investigation, we tested a new retrieval logic, in which we turn off the "switch" by tuning the criteria of 10 DU close to the minimum detectable value of about 0.5 DU.

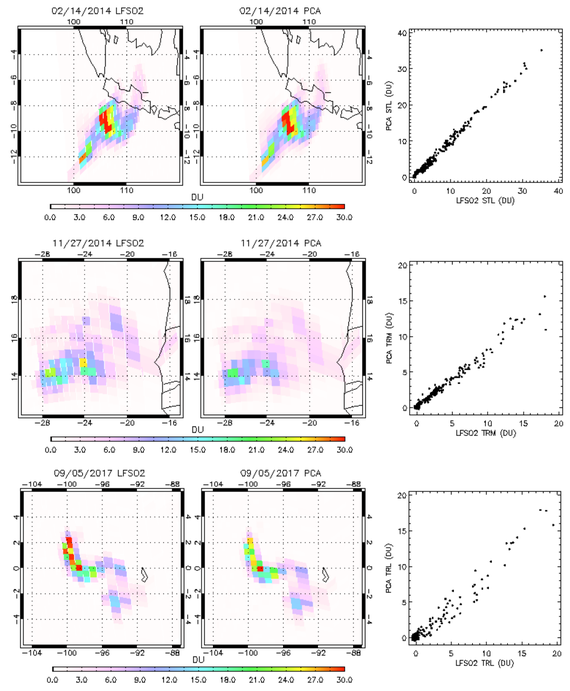

Figure 3 The figure demonstrates the LFSO2 retrievals status after using improved retrieval logic. The figure arrangement is the same as in figure 1.

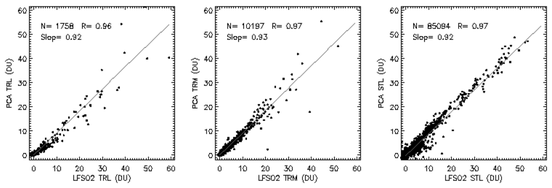

Figure 4. Comparisons between improved LFSO2 and PCA in all three volcanic SO_2 cloud heights in the 29 selected scenarios are illustrated. From left to right are SO_2 appeared in the layers of TRL, TRM, and STL.

LFSO2 vs. PCA over Kilauea Hawaii

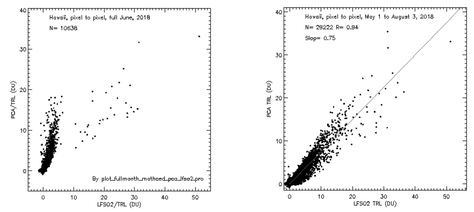

Figure 5. Hawaii Kilauea volcano erupted form May 3 to August 5 in 2018 as measured by S-NPP. We investigated this event in a latitude/longitude box (14°N to 24°N and 150°W to 165°W) for LFSO2 before and after its improvements. The left panel shows the current operational LFSO2 vs. PCA collected over the full month in June 2018. The right panel shows improved LFSO2 vs. PCA for three month data from May 1 to August 3, 2018.

LFSO2 vs. PCA in PBL retrieval

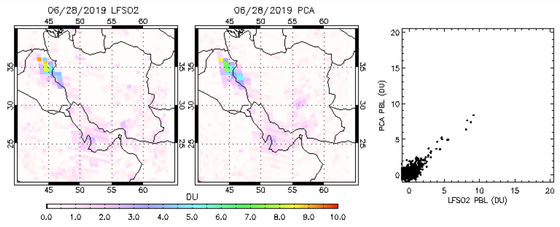

Figure 6. A Sulphur company fire near Mosul in Iraq has been measured by OMPS. LFSO2 results and PCA results are given in the left and middle maps. Their pixel to pixel comparison results are illustrated by the scatter plot on the right panel.

LFSO2 minimum detectable

The minimum detectable amount for both LFSO2 and PCA at PBL, TRL, TRM, and STL layers are estimated in the Equatorial Pacific region. The geographic extent is 120° to 150° west longitude and ±10° in latitude. A total of 76 cases with little or no expected SO_2 contamination were selected in the region from May 1 to August 1, 2018 for the evaluation.

Table 3. Average means and standard deviations over 76 days

	Mean PBL	STD (PBL)	Mean TRL	STD (TRL)	Mean TRM	STD (TRM)	Mean STL	STD (STL)
LFSO2	0.087	0.53	0.019	0.19	0.0077	0.087	0.0064	0.071
PCA	0.077	0.32	0.023	0.16	0.012	0.087	0.01	0.073

S-NPP OMPS and S5P TROPOMI

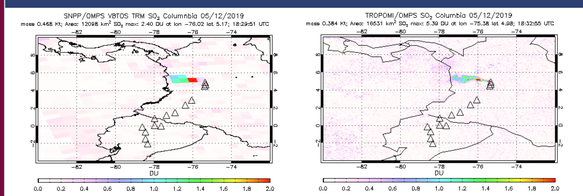

Figure 7. Both satellite witnessed a vary similar SO_2 cloud pattern. The total SO_2 cloud mass estimated by each instrument is similar as expected. The difference in maximum total amount is caused by different spatial resolution.

Summary

1. Current operational LFSO2 retrievals have been compared with PCA retrievals both from S-NPP OMPS NM observations.
2. Discontinuity and nonlinearity are found in operational Linear Fit results in TRL, TRM, and STL layers versus PCA results.
3. Investigation indicated these are caused by two independent retrieval techniques, linear fit and BRD, both are used in the LFSO2 by switch on or off based on a previously determined criteria.
4. We tested the effects of turning off the BRD technique and using the linear fit technique only.
5. We redo the all the same pixel by pixel comparisons, and the results demonstrate that the discontinuity and nonlinearity problem are removed and reduced, respectively.
6. A new updated LFSO2 algorithm is ready for use in operation.
7. LFSO2 PBL retrievals have a close to linear relation with PCA.
8. Except for the noisier PBL retrievals, TRL, TRM, and STL products have similar noise level as those of PCA.

Acknowledgment and contact

This research and development work was supported by the NOAA JPSS Program. The poster contents are solely the opinions of the authors and do not constitute a statement of policy, decision, or position on behalf of NOAA or the U. S. Government.

Contact: **Jianguo.Niu@noaa.gov**

Is stratospheric ozone recovering as we expect? Results of the SPARC/WMO LOTUS analyses.

I. Petropavlovskikh (1,2) (irina.petro@noaa.gov), D. Hubert (3), S. Godin-Beekmann (4), R. Damadeo (5), B. Hassler (6), V. Sofieva (7), W. Ball (8), K.L. Chang (1), Kleareti Tourpali (9), Jeannette Wild (10), Stacey Frith (11), and others

(1) GMD, NOAA/ESRL, Boulder, CO, USA , (2) CU/CIRES, Boulder, CO, USA , (3) Royal Belgium Institute for Space Aeronomy, Brussels, Belgium; (4) Université de Versailles Saint-Quentin en Yvelines (UVSQ), Centre National de la Recherche Scientifique (CNRS), Guyancourt, France; (5) NASA Langley Research Center, Hampton, VA; (6) Institut für Physik der Atmosphäre, Oberpfaffenhofen, Germany; (7) Finnish Meteorological Institute, Helsinki, Finland; (8) ETH, Zürich, Switzerland; (9) LAP, Aristotle University of Thessaloniki, Greece; (10) University of Maryland Earth, SSIC, College Park, MD; (11) NASA/Goddard, MD, USA.

LONG-TERM OZONE TRENDS AND UNCERTAINTIES IN THE STRATOSPHERE

LOTUS

SPARC Stratosphere-troposphere Processes And their Role in Climate

WCRP World Climate Research Programme

WORLD METEOROLOGICAL ORGANIZATION

UNESCO United Nations Educational, Scientific and Cultural Organization

Intergovernmental Oceanographic Commission

International Science Council

IOC International Ozone Commission

The LOTUS-2 project goals:

(a) Update and extend stratospheric ozone observations to recent years

(b) Improve our understanding of crucial yet poorly known sources of uncertainties in trend retrieval

(c) Investigate how uncertainties interact and propagate through the different stages of analysis chain

(d) Re-evaluate current best practices and possibly establish more suitable alternatives.

SPARC website :

http://www.sparc-climate.org/activities/ozone-trends/

LOTUS 2020 workshop website

https://events.spacepole.be/event/81/

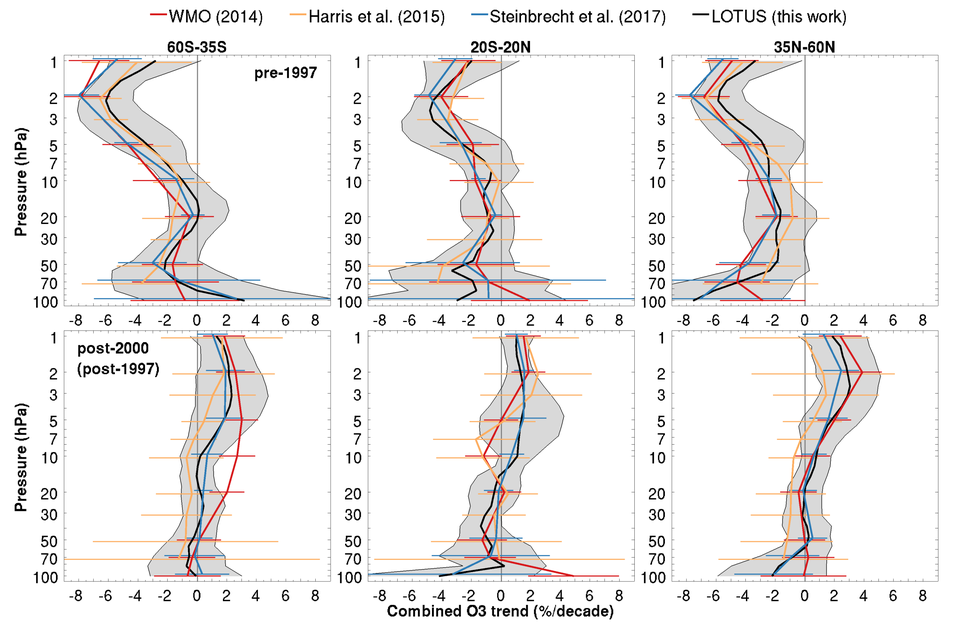

Figure 1: Trends from SPARC/WMO LOTUS Report 41 compared to WMO/UNEP 2014 Ozone Assessment, SI2N initiative (Harris et al, 2014) and W. Steinbrecht et al (2017). Upper panel: trends from 1985-1996, Lower panel: trends for 2000-2016 period. Satellite trends are combined in three latitude bands.

Satellite datasets per measurement principle

Group 1. Ozone profiles from nadir sensors (partial columns on pressure grid)
SBUV NASA MOD (Release 6)
NOAA COH

Group 2. Ozone profiles from limb instruments in mixing ratio on pressure grid
HALOE – MLS

Group 3. Ozone profiles from limb instruments in number density on altitude grid
corrSAGE II (by Damadeo)–OSIRIS–OMPS (Usask 2D v1.02)
SAGE II – OSIRIS – OMPS (Usask 2D v1.02)
SAGE II – Ozone_cci – OMPS (Usask 2D v1.02)
SAGE-II – MIPAS – OMPS (NASA v2.2)

The dataset with converted ozone representation
Mixed coordinates converted to mixing ratio on pressure
GOZCARDS v2.2, SWOOSH v 2.6

Ground-based Instruments	Station, period since
Lidar	OHP (1986), Hohenpeißenberg (1987), Table Mountain (1988), Mauna Loa (1993), Lauder (1994)
Microwave	Bern (1994), Payerne (2000), Mauna Loa(1995), Lauder (1992)
FTIR	Izana (1999), Lauder (2001), Jungfraujoch (1995), Wollongong (1996)
Umkehr	Mauna Loa (1984), Lauder (1987), Arosa (1956), OHP(1984), Boulder(1984), Perth (1984)
Ozonesondes	NOAA and SHADOZ datasets, zonal averages

Q: Do different regression models have impact on trends?
A: Trend results agree within ~1%/decade. Larger differences noted for other regressed terms, e.g. Solar & QBO. Tests were used to identify importance of different explanatory variables for the LOTUS regression models.

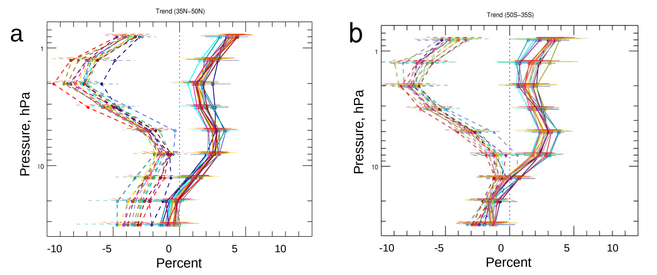

Figure 2 (to the right). *Common dataset (SBUV NASA MOD) test was used in 8 multiple linear regression (MLR) models. Results for Trends (dashed lines for pre-1998 and solid lines for post 2000) and associated uncertainties are shown for* ***a)*** *35N-50N and b) 35S-50S.*

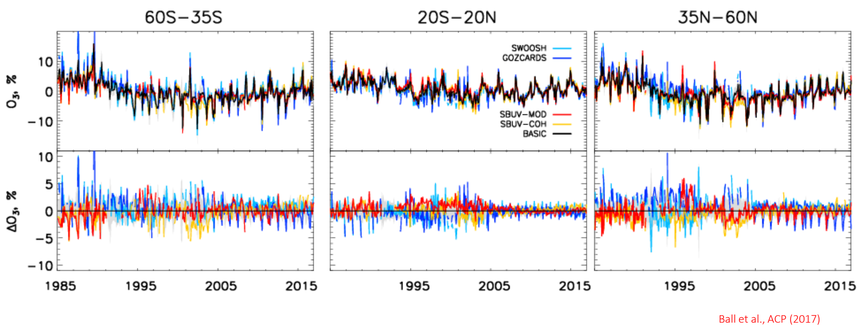

Figure 5. BASIC analyses: uses SWOOSH, GOZCARDS, SBUV NASA MOD (marked as SBUV-MOD in the legend) and NOAA COH (marked as SBUV-COH in the legend) ozone to identify instrumental drifts and then create the best record and derive trend.

Recent accomplishments

- Provided results of ozone trend analyses to Chapter 3 in the 2018 WMO/UNEP Ozone assessment.
- SPARC/IO$_3$C/GAW, 2018: SPARC Report N°9 (2019) of The SPARC LOTUS Activity: SPARC/IO3C/GAW Report on Long-term Ozone Trends and Uncertainties in the Stratosphere. Edited by I. Petropavlovskikh, S. Godin-Beekmann, D. Hubert, R. Damadeo, B. Hassler, and V. Sofieva. SPARC Report No. 9, WCRP Report 17/2018, GAW Report No. 241 doi: 10.17874/f899e57a20b, www.sparc-climate.org/publications/sparc-reports
- LOTUS multiple linear regression (MLR) trend model, download from https://arg.usask.ca/docs/LOTUS_regression
- Dynamical linear model (DLM; Laine et al., 2014; Alsing, 2019: github.com/justinalsing/dlmmc)

Q: *How stable are the new satellite combined ozone records relative the to the ground-based data?*
A: *Insignificant drifts are found in most combined limb-satellites. SBUV NASA MOD and NOAA COH merged datasets show different drifts relative to MLS.*

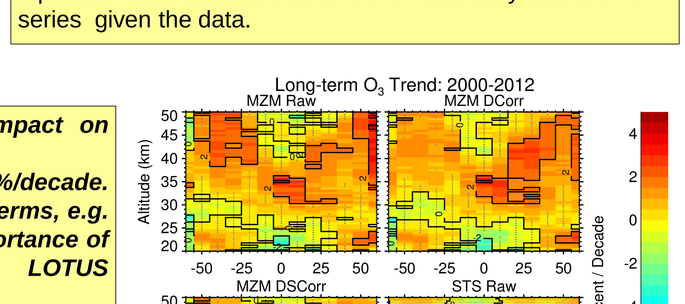

Figure 3. *Time series of the time-smoothed relative difference of Hohenpeissenberg (top) and Observatoire Haute Province (Bottom) lidar and Aura MLS satellite ozone profile data, offset to the median value in the reference period. Thin grey vertical lines at the bottom show the sampling of the co-located profile data records. Adapted from Hubert et al. (in preparation, 2020).*

Q: Are there sampling issues that can impact on the derived trends?

Approach 1: Create sampling-bias corrected monthly zonal mean data set (**corrSAGE**) **Simultaneous temporal and spatial (STS) regression** can separate and characterize sampling effects (with limitations)

Approach 2: Bayesian Integrated and Consolidated **(BASIC)** composite method merges multiple ozone composites within a probabilistic framework to form the most likely ozone time-series given the data.

Figure 4 Trends derived from MZM using different corrections (raw=top left, diurnal correction =top right, diurnal & seasonal corrections =bottom left) and STS (raw=bottom right) regressions

Q: Do CCMI models agree with observations?
A: Yes, in long-term, but models (REF-C2) cannot fully capture the natural (i.e. volcanic/QBO) variability that is seen in observations.

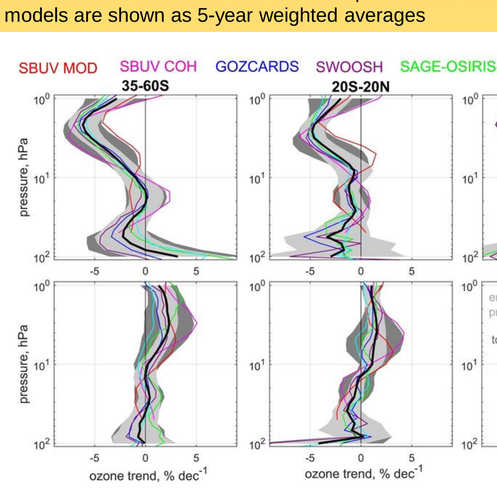

LOTUS models for trend analyses:
PWLT *– piece wise linear trend*
ILT *– independent linear trends for two periods*
EESC (1,2) *– single and two EOFs as the long-term proxy for the Effective Equivalent Stratospheric Chlorine in the atmosphere*
The ***LOTUS MLR*** *trend model is comprised of the trend (linear or EESC based) and seasonal component,* ***Solar cycle, QBO, ENSO and aerosol proxies.***
LOTUS trend model: *https://arg.usask.ca/docs/LOTUS_regression/*
Special thanks to Daniel Zawada and Doug Degenstein of USASK for developing and maintaining the LOTUS trend code.

Figure 6. The evolution of ozone changes as annual mean anomalies at the 10 hPa/31 km level. Four different latitude bands are shown. Satellite data are based on zonal means, and ground-based stations are averaged over the latitude bands. The grey "envelope" gives the **CCMI (RefC2)** model results, based on the models 10th and 90th percentile. The model mean, the median and the ± 2 standard deviation range of the mean are also plotted. All anomalies are calculated over the base period 1998-2008, and the CCMI models are shown as 5-year weighted averages

•SPARC LOTUS activity phase 1 results:

- delivered and intercompared several state-of-the-art satellite and ground-based ozone profile data sets, complemented with CCMI model data
- developed a common multiple linear regression test-bench written in Python
- defined a baseline regression model after review of methods and auxiliary datasets used for ozone trend analyses
- assessed trend and trend significance of individual data sets
- suggested a new and reviewed previous methods to combine trends and trend uncertainties
- assessed ozone profile trends in the stratosphere based on satellite, ground-based, and model records

Q: How will trends change if three different trend methods are applied?
A: All three methods capture very similar patterns in stratospheric ozone trends.
Q: If one regression method (ILT) is used what do different datasets tell us about stratospheric trends?
A: Similar patterns are found in all tested satellite records, i.e. statistically significant ozone recovery at ~ 40-50 km (1-5 hPa) altitude. Although magnitude of the trends vary they are all comparable within individual trend uncertainties.

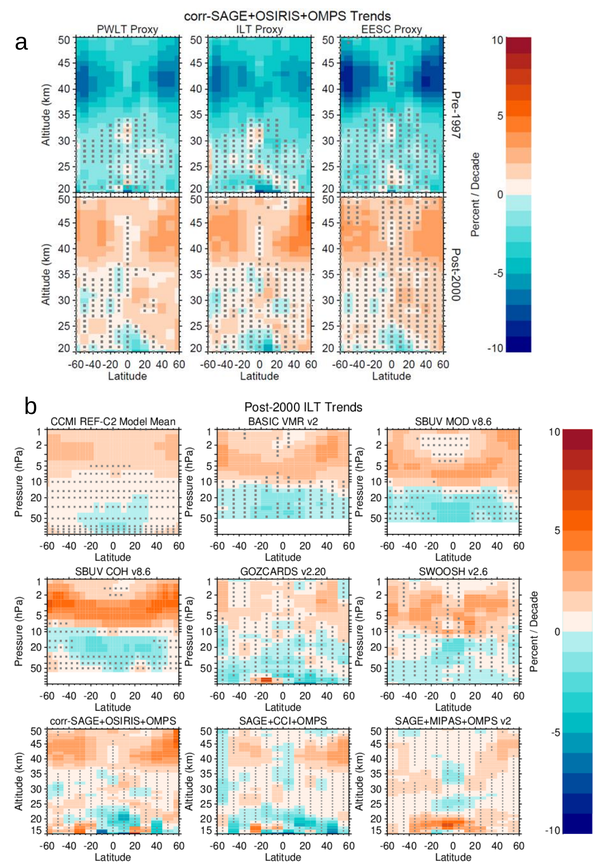

Figure 7 (above). a) Derived trends in ozone in percent per decade for the corrSAGE II-OSIRIS-OMPS data sets for both the pre-1997 (1985-1997, top row) and post-2000 (2000-2016, bottom row) time periods. Results are shown for each of the three trend proxies: the PWLT (left), ILT (middle), and EESC EOFs (right) proxies.
b) Derived trends in satellite ozone in percent per decade for the period 2000 to 2016 for each of the satellite data sets, using the ILT trend proxy in a regression analysis. Grey stippling denotes results that are not significant at the 2-sigma level.

Figure 8 (left). Combining pre-1997 (top) and post-2000 (bottom) trend estimates and uncertainties (2-sigma) from six limb profile data sets. Black solid line indicates the mean trend. The uncertainty component corresponding to error propagation (envelop in light grey shading), and total (dark grey shading) uncertainty are included. Dataset correlation correction is included.

Open issues from the SPARC/WMO LOTUS report and NOAA OAR/AC4 project to homogenize NOAA COH and Umkehr ozone records for trends.
Analyses

- Continue to monitor upper stratosphere ozone levels in tropics & mid SH latitudes. Do these continue to rise at mid NH latitudes?
- Are post-2000 LS ozone levels really declining? (Wargan et al., 2018; Chipperfield et al., 2018; Ball et al., 2018, 2019, 2020)
- Seasonal trends need to be evaluated (Szeląg, ACPD, 2020)
- Do O3 profile & column trends agree? (Weber et al, 2018 found semi-neutral TO trends)
- What is tropospheric ozone contribution to TO (IGAC TOAR questioned stability in some records, Ziemke et al, 2018, Gaudel et al, 2018).
- How consistent are GND (local) & SAT (zonal) data? (Zerefos et al, 2018, Bernet et al, 2019, **NOAA/OAR AC4 project**)

- **Data records**
  - Ultimately, LOTUS analyses conclude that the most meaningful way to improve the uncertainties in future analyses would be to **reconcile the discrepancies between the data sets** themselves prior to the merging process (**NOAA/OAR AC4 project**)
  - Satellites: new updates to L1, L2, L3, **i.e. JPSS S-NPP OMPS nadir and limb profiles in combined and homogenized records (NOAA OAR AC4 project); gridded data for trends (i.e. NOAA's SWOOSH)**
  - Ground-based (Umkehr, ozonesonde, NDACC lidar and MW homogenization, combining station data for trends to improve sampling biases)
- **Regression**
  - Investigate if LOTUS regression model (developed for satellite records) is also adequate for ground-based records.
  - More systematic study of sensitivity to proxies on all data records is needed (**NOAA/OAR AC4 project**).
  - Explore spatial structure of proxy coefficients in more detail.
  - DLM vs. MLR trends
- **Uncertainties**
  - Can / should we avoid combining trend profiles & uncertainties?
  - How to estimate correlation between trend estimates? (NOAA/OAR AC4)

$$\sigma^2_{mean} = \max\left(\frac{1}{N^2}\sum_{i,j} C_{ij}\sigma_i\sigma_j,\ \frac{1}{n_{eff}}\sum\frac{(x_i-\bar{x})^2}{N-1}\right)$$

$$n_{eff} = \frac{N^2}{\sum_{i,j=1}^{N} C_{ij}}$$

LOTUS Uncertainties.
The first term is the variance of the mean of correlated values, obtained through traditional propagation of errors. The second term is the unbiased estimator of the standard error of the mean, where n_{eff} independent measurements are assumed from the N=6 different trend estimates.

N is the number of independent observation records, C_{ij} are the correlation coefficients for the trend estimates x_i from data sets i and j ,$[\![\ \sigma]\!]_i$ are the trend uncertainties estimated from the fit residuals for the individual data sets, and n_{eff} is the effective number of independent trend estimates.

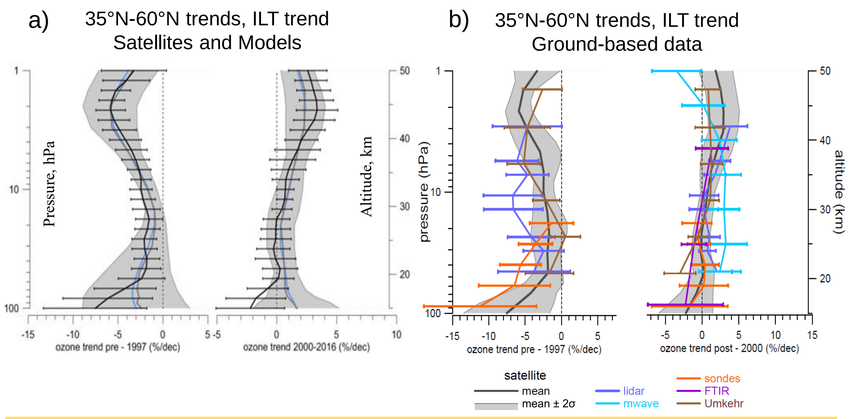

Figure 9. a) The combined satellite trends (black line) and uncertainties, calculated by the sequential averaging method: takes correlations between the individual trend estimates into account and considers systematic uncertainties as well. The CCMI model trends (grey – mean and blue – median) and variably is shown as grey envelops.
b) Derived trends from ground-based (GB) ozone records, in percent per decade, for the period 2000 to 2016, using the ILT trend proxy in a regression analysis. Ground-based trends are combined into zonal averages by weighted error means, but only in the upper stratosphere combined GB trends become representative of the broad-band zonal trends. Satellite combined trends are shown as mean with grey envelop.

V8TOz and V8Pro Ozone Products at NOAA

Zhihua Zhang[1,2], Lawrence E. Flynn[2], Eric Beach[1,2], Jianguo Niu[1,2] , Trevor Beck[2]

[1]I.M. Systems Group, Rockville, MD; [2]NOAA/NESDIS Center for Satellite Applications and Research, College Park, MD

Poster# 26
JPSS/GOES-R PGRR Summit
Feb 25-27, 2020

Introduction

V8TOz and V8Pro products from the S-NPP Ozone Mapping and Profiler Suite (OMPS) have been running on the NOAA NDE near-real-time system. However, due to a numbers of updates and changes to the Level 1 Sensor Data Records (SDRs), there are inconsistencies and biases in the operational products of daily global total ozone, nadir ozone profiles, UV reflectivity and aerosol indices. This poster will describe analysis to create soft-calibration adjustments of NOAA OMPS/S-NPP V8TOz and V8PRO products to remove internal inconsistencies, maintain stability over time, and to better agree with the NASA S-NPP OMPS products. The NASA products were adjusted to agree with the NOAA-18 SBUV/2 ozone products so the reprocessed products from V8TOz and V8Pro will provide users with a new, consistent component of the long-term climate data record extending from February 2012 to present. The adjustments will also be implemented in the forward processing on the operational NDE system.

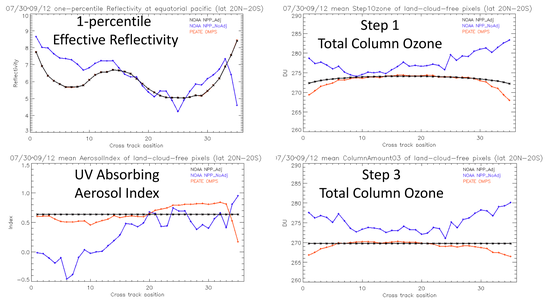

OMPS V8TOz Soft-Calibration

NOAA OMPS/S-NPP V8TOz was adjusted to agree with NASA/V8TOz. The data used for this soft-calibration is from Jul/30, 2018 to Sep/12, 2018. The figures above show that, before soft-calibration, the one-percentile reflectivity, aerosol index and step1/step3 ozone vary significantly over 35 cross-track Fields of View. The natural "truth" ozone and aerosol patterns would be expected to show a flat averaged value dependence cross-track over a period time. So, this systematic cross-track bias has to be removed for high quality retrievals. The N-Value adjustments were calculated based on N-Value sensitivity to ozone and reflectivity(see figure below). The figure also shows that, after soft-calibration, the cross-track bias for the ozone and aerosol retrievals was mostly "leveled out", with reflectivity over equatorial Pacific showing sun-glint signals and high view angle effects.

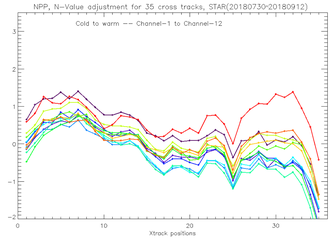

Zhihua.zhang@noaa.gov

The figures below show OMPS V8TOz retrieved total column ozone and aerosol index values. There is apparent striping like structure in the global ozone retrieval before soft-calibration. This systematic cross-track related bias were completely gone in the retrievals when adjustments were put in the processing. The comparison between NASA processed OMPS ozone retrieval and NOAA processed OMPS ozone shows that the global total column ozone patterns are almost identical even though there are slightly difference in SDR and cross track positions.

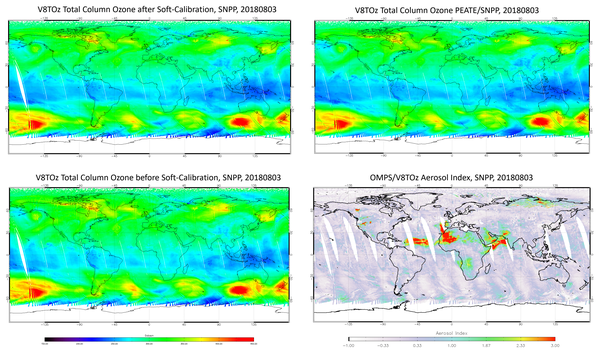

OMPS V8PRO Soft-Calibration

The NOAA OMPS/S-NPP NP V8Pro was adjusted to agree with the results for NASA Version2.6 OMPS/S-NPP NP V8Pro which had already been adjusted to NOAA-19 SBUV/2 and previous NOAA SBUV/2 series. 5 days' retrievals (03/18/2013- 03/22/2013) was selected to estimate calibration offsets and adjustments. The table below shows the averaged retrievals over Pacific box where we make statistical analysis before and after adjustments.

Averaged Retrievals over Pacific Box from OMPS-NPP V8PRO

	NASA	NOAA/0-adj	NOAA/adj
Reflectivity	0.196	0.188	0.196
Step1-O3	250.60	254.62	250.60
Step2-O3	248.92	253.10	249.07
Step3-O3	246.99	251.58	247.17
Total-Profile	252.90	249.01	252.71
Aerosol-Index	0.71	0.55	0.71

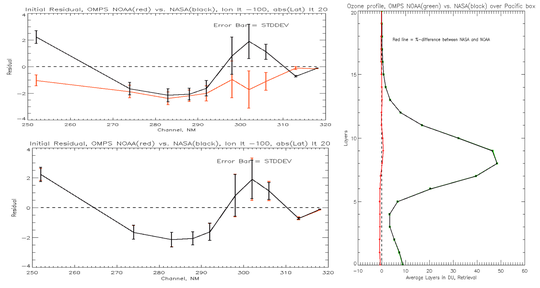

The figures above compare the averaged initial residuals between NASA OMPS SNPP and NOAA OMPS SNPP over Pacific box before and after adjustments. The well-matched values of initial residual after adjustment make the retrieved ozone profiles agree well with each other as show in the plot on the right.

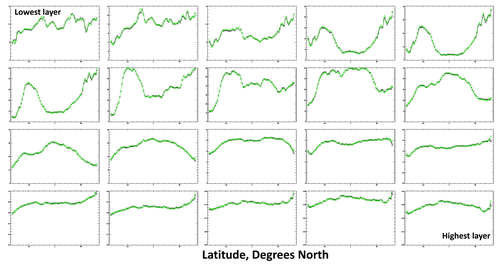

The figure above shows the averaged ozone profiles that confirms that the retrieved layer ozone values from NOAA OMPS are very close to those from NASA OMPS, with differences less than one percent for all the layers. The figure in the top of the next column shows the layer ozone amounts from the Version 8 Ozone Profile Retrieval Algorithm for both NASA and NOAA OMPS NP as a function of Latitude after applying the adjustments over a orbit. The very small differences in retrieved ozone indicate slight differences in SDR values as processed by the two systems.

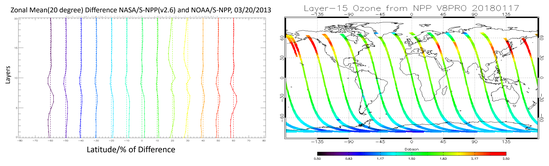

The plot on the left above shows the percent differences at 21 layers for 20-degree zonal mean between NOAA SNPP V8Pro retrievals and NASA retrievals after adjustments. The results indicates that the N-Value adjustments based on statistics over Pacific ocean are adequate to apply globally. Some relative large deviation (~5%) seen at some layers in higher latitude area imply small disagreement of SDR data between NASA OMPS and NOAA OMPS. The OMPS S-NPP V8Pro retrieved layer-15 ozone amounts (see plot on the right above) show the typical wintertime ozone pattern with apparent higher ozone density in the Northern Hemisphere then in the Southern Hemisphere.

Products and Monitoring

NOAA/NESDIS/STAR has a well designed Integrated Cal/Val System(ICVS) to monitor the performance of instrument, to compare products from different instruments or algorithms, to alert the occurrence of natural disaster events, as well as to monitor the long-term environmental change.

The figures at the top of the next column show daily total column ozone latitudinal mean from NOAA OMPS S-NPP for the year 2018 and 2019. The spatial-temporal ozone pattern in the year shows apparent seasonal structures, which switch around the end of Spring and around the begin of Fall. The variation of timing for the switch and the strength of seasonal pattern should have strong association with global general circulation and weather patterns. The daily zonal mean ozone differences for the year 2019 and 2018 show a reduced ozone latitudinal gradient in the Northern Hemisphere for the winter and spring in 2019. The extremely enhanced ozone gradient in the Southern Hemisphere begins at the end of August suggests we will have a very unusual ozone hole season this year.

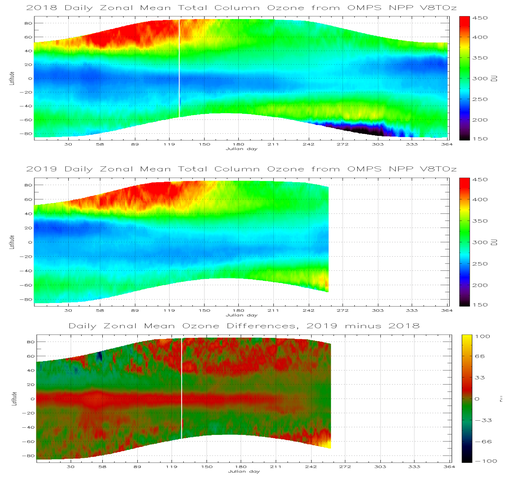

NOAA regularly monitors the Antarctic ozone hole variation, as well as global aerosol loading from wildfire, dust storm and anthropogenic air pollution. The figure (to the right) below shows the ozone hole on Oct. 12, 2018 from S-NPP at NOAA NDE, which is the 13th largest out of 40 years of satellite observations. The figure (to the left) shows that the S-NPP detected smoke plumes from wildfire occurred in the North America in August 2018. Apparently, this major wildfire influenced the aerosol loading for regions as far away as western Europe.

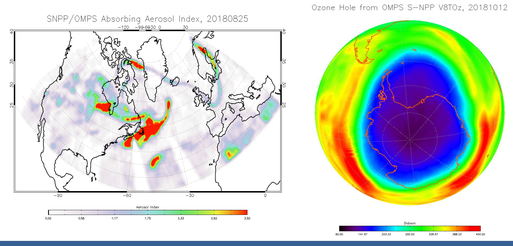

Conclusions

- The well calibrated retrievals from OMPS/S-NPP V8PRo and V8TOz can provide users with a consistent component of long-term climate data records.
- The OMPS/S-NPP has had stable performance in orbit, and is able to continue providing near-real time environment monitoring.

References

[1] Flynn, L., et al. (2014), Performance of the Ozone Mapping and Profiler Suite (OMPS) products, J. Geophys. Res. Atmos., 119, 6181–6195, doi:10.1002/2013JD020467.

[2] Bhartia, P. K., McPeters, R. D., Flynn, L. E., Taylor, S., Kramarova, N. A., Frith, S., Fisher, B., and DeLand, M.: Solar Backscatter UV (SBUV) total ozone and profile algorithm, Atmos. Meas. Tech., 6, 2533-2548, doi:10.5194/amt-6-2533-2013, 2013.

[3] Rodgers, C.D., "Retrieval of atmospheric temperature and composition from remote measurements of thermal radiation," *Rev. Geophys. Space Phys.*, **14**, 609-624, 1976.

Acknowledgment & Disclaimer

This work was supported by the NOAA JPSS program. The results and opinions are those of the authors and do not reflect any official policy of NOAA.

Atmospheric Chemistry, Carbon Cycle And Climate Program

ATMOSPHERIC COMPOSITION FROM SPACE

Program Managers: Monika Kopacz & Kenneth Mooney | NOAA/OAR Climate Program Office

WHAT IS THE AC4 PROGRAM?

AC4 is a competitive research program that focuses on atmospheric composition. The program aims to provide a process-level understanding of the climate system through observation, modeling, analysis, and field studies to support the development and improvement of models and ultimately predictions.

AC4 is part of OAR, under the Climate Program Office (CPO). On atmospheric composition from space, AC4 collaborates with **NESDIS** directly through product development and validation, but also with users across OAR, namely with **ESRL**'s Chemical Sciences Division and Global Monitoring Division, **ARL** and **GFDL**.

PROGRAM GOAL

Determine the processes governing atmospheric composition in the context of the Earth system and climate.

RESEARCH AREAS

In collaboration with NOAA labs and line offices, as well as the academic community, AC4 has supported research on:

- trace gases,
- aerosols – their emissions,
- chemistry and transport,
- aerosol-cloud interactions in connection, and
- research on atmospheric and oceanic components of carbon cycle.

SCIENTIFIC CAPABILITIES

AC4 supported research spans several platforms. Primarily, it focuses on in situ field measurements, but also includes laboratory experiments, analysis of field and monitoring observations, as well as process, regional, global and Earth system modeling. In situ measurements allow for satellite data validation, while satellite data are a data source for all types of atmospheric composition studies.

NOAA Satellite Products

AC4 program science can benefit from all trace gas, aerosol and related products retrievable from JPSS and GOES-R instruments, including:

- CrIS: carbon monoxide, CO_2, ozone, methane, ammonia, SO_2, N_2O, PAN, isoprene
- OMPS: ozone, NO_2, HCHO
- VIIRS: burned area, AOD, other fire products

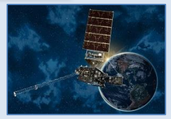

SATELLITE PRODUCT VALIDATION

FIELD CAMPAIGNS

During field campaigns, coordinated vertical profiles of measurements from an aircraft are a good source of validation data for all types of chemical species. FIREX-AQ field campaign in 2019 featured several aircrafts measuring chemical species such as CO, ozone, CH_4, NH_3 and may others.

IN SITU MEASUREMENTS

Validation of satellite data using vertical profiles of atmospheric composition has most recently been enhanced by AirCore, developed and deployed by ESRL's Global Monitoring Laboratory. AirCore measures CO_2.

ROUTINE MONITORING

Ozone profiles at the South Pole provide vertical profiles for validation of satellite products.

PROJECT HIGHLIGHTS

Between FY13 and FY19, AC4 has supported 10 projects that specifically focus on development and application of JPSS data in atmospheric composition research. Several more include other relevant satellite data products. Below are just a few examples.

Biosphere emits chemical compounds that can form aerosols. Formaldehyde (HCHO) is a chemical product of the most abundant biogenic volatile organic compound (BVOC), which is observable from space by OMPS instrument.

Ammonia (NH_3) emissions. NH_3 is an important trace gas, emitted from various sources such as agriculture and wildfires. It can be retrieved from CrIS instrument.

Carbon monoxide and ozone are good tracers of biomass burning. Both species were retrieved from CrIS and tested during FIREX-AQ field campaign.

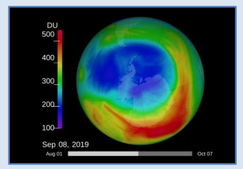

Status of stratospheric ozone recovery can be monitored through ozone measurements retrieved from OMPS instrument, thus continuing a long term satellite record.

FUTURE APPLICATIONS

- Improved understanding of atmospheric composition
- NOAA Climate/Earth System Model (GFDL) development and validation
- Air quality forecasting
- NGGPS
- Monitoring of air pollution and greenhouse gases

LEARN MORE

AC4 program website:
www.climate.noaa.gov/ac4
Climate Program Office website:
ww.climate.noaa.gov
CrIS Atmospheric Chemistry Data Users' Workshop report:
https://repository.library.noaa.gov/view/noaa/11187

Towards an improved understanding of the CO budget through different data assimilation frameworks

B. Gaubert[1], M. Trudeau[2], Louisa Emmons[1], Simone Tilmes[1], Helen Worden[1] and Nadia Smith[3]

(1) National Center for Atmospheric Research, (2) NOAA Earth System Research Laboratory, Global Monitoring Division (3) IMSG - NOAA/NESDIS/STAR

BACKGROUND

Why are models underestimating CO?

$$\frac{d[CO]}{dt} = \frac{\delta[CO]}{\delta t}_{transport} + \frac{\delta[CO]}{\delta t}_{emissions} + \frac{\delta[CO]}{\delta t}_{chemical\ sources} - k_{OH}[CO][OH] - k_{dep}[CO]$$

➢CO is important for tropospheric chemistry, it is a major sink for OH, and can produces Ozone.

➢Common underestimation is not understood

- ❖ Anthropogenic sources
- ❖ Biogenic sources
- ❖ OH sink
- ❖ Deposition

METHODS

Acronym	CAM-Chem/DART	TM5 4DVar
horizontal resolution	0.9° x 1.25°	3°x2° global, 1°x1° zoom
Number of vertical layers	32	25
Chemical assimilation	MOPITT V8J	GGGRN data*, MOPITT V8J
Meteorological assimilation	yes	no (offline, driven by ERA-Interim)
Online dynamic	yes	no (offline, driven by ERA-Interim)
online chemistry	yes	yes (OH sink)
online aerosols	yes	no
Methyl Chlorofom OH	no	yes
Interactive OH	yes	no (fixed OH)
Anthropogenic	CMIP6 + CREATE	MACCity
BB	FINN 1.5	GFED41s
Biogenic	MEGAN 2.1 (CLM)	MEGAN v2 + POET
DA algorithm	EAKF	4DVar
State optimization	CO + some VOCs	CO
Anthropogenic emissions	yes	no
BB emissions	yes	yes
Chemical source flux	No (but interactive chem)	yes (IMAGES total column)
Chemical sink flux	No (but interactive chem)	no

KORUS-AQ field campaign

- ➢ 20 research flights over South Korea in May-June 2016 with the NASA DC-8 aircraft.
- ➢ Vertical profiles of CO, Ozone, Methane (CH4), Formaldehyde (CH2O).
- ➢ Extreme gradients of pollution, in space and time, over different weather regimes

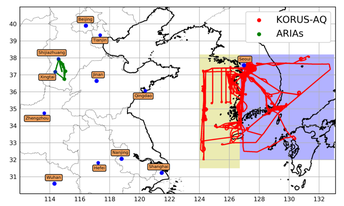

Location of the KORUS-AQ DC8 and of the ARIAs Y-12. Dots are from the 1-min merge.

RESULTS

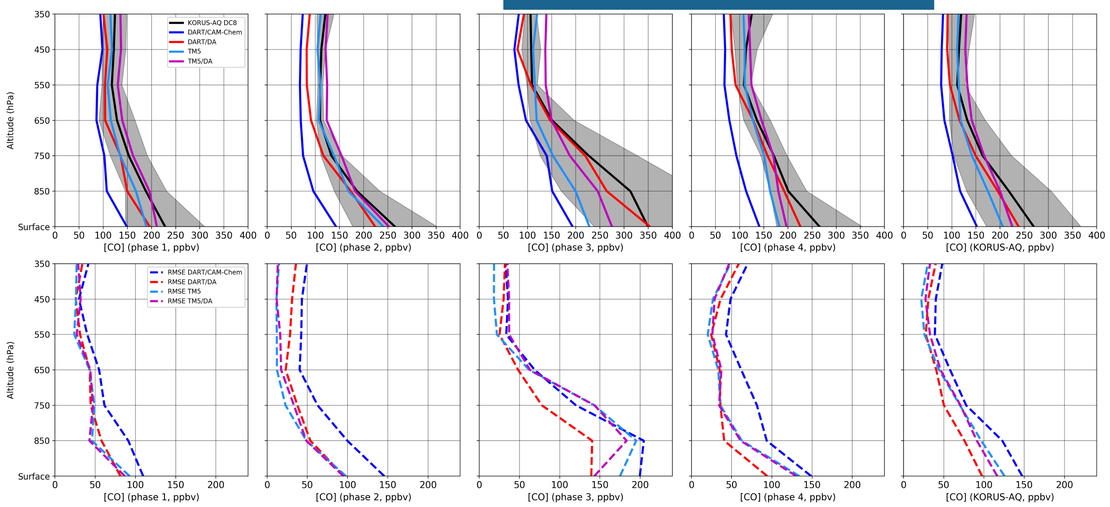

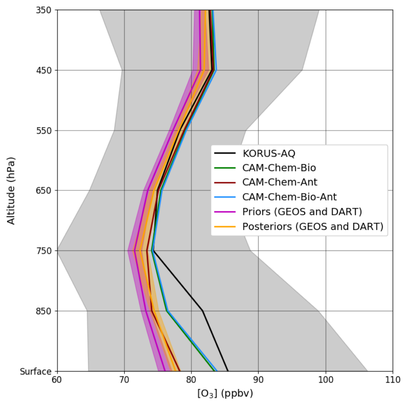

- ❖ Phase 1, the synoptic weather system dynamically changed.
- ❖ Phase 2: Synoptic flow was weak, stagnant conditions led to strong enhancements of pollution over the Korean Peninsula.
- ❖ Phase 3: Strong westerlies existed, polluted air was rapidly transported from China to Korea, causing extreme pollution.
- ❖ Phase 4: a blocking pattern determined the large-scale ozone distribution over East Asia.

CONCLUSIONS

- ➢ **Inversion and forward runs suggests that most up to date emissions are underestimated.**
- ➢ **Sensitivity experiments with CAM-Chem suggest that secondary CO is also underestimated, and is confirmed through comparison of measured VOCs.**
- ➢ **The correction of the CO emission bias improve the Ozone profile and increasing biogenic emissions leads to a better Ozone.**
- ➢ **CLIMCAPS CrIS is going to provide additional constraints, work in progress.**
- ➢ **Will assess the role of OH, chemical sources and transport on retrieved emissions.**

ACKNOWLEDGMENTS

This work is supported by the NOAA grant NA18OAR4310283. The NCAR MOPITT project is supported by the National Aeronautics and Space Administration (NASA) Earth Observing System (EOS) Program. Computing resources were provided by the Climate Simulation Laboratory at NCAR's Computational and Information Systems Laboratory (CISL), sponsored by the National Science Foundation and other agencies. NCAR is sponsored by the National Science Foundation. KORUS-AQ data are available at https://www.air.larc.nasa.gov/cgi/bin/ArcView/korusaq.

Global Formaldehyde Products from the OMPS Nadir Mappers on Suomi NPP and NOAA-20

Caroline Nowlan[1,*], Gonzalo González Abad[1], Lei Zhu[1,2,3], Christopher Chan Miller[1], Amir Souri[1], Ewan O'Sullivan[1], Yeonjin Jung[1], Kelly Chance[1], Lawrence Flynn[4], Glen Jaross[5], Colin Seftor[5]

[1]Center for Astrophysics | Harvard & Smithsonian, Cambridge, MA, [2]Harvard University, Cambridge, MA, [3]Southern University of Science and Technology, Shenzhen, China,
*[4]NOAA Center for Satellite Applications and Research, College Park, MD, [5]NASA Goddard Space Flight Center, Greenbelt, MD, *cnowlan@cfa.harvard.edu*

CENTER FOR ASTROPHYSICS HARVARD & SMITHSONIAN

1. Atmospheric Formaldehyde

- Formaldehyde (HCHO) is one of the most abundant non-methane volatile organic compounds (NMVOCs) in the troposphere.
- Enhanced levels result from oxidation of VOCs from biogenic, anthropogenic and pyrogenic activities, and direct emissions from fires and industry.
- Background HCHO exists in the global atmosphere due to the oxidation of methane.
- ***HCHO measured by satellites can be used as a proxy for other NMVOCs and as a top-down constraint on isoprene emissions.***

2. The OMPS Nadir Mapper Instruments

- The OMPS (Ozone Mapping and Profiler Suite) instruments include a nadir mapper which uses a 2D CCD array detector to measure backscattered solar light in a ~2800 km wide swath.
- The equatorial local overpass time is ~1:30 PM.
- OMPS currently flies on the Suomi NPP and NOAA-20 satellites.

Table 1: Characteristics of OMPS nadir mappers currently on orbit.

	OMPS Suomi NPP	OMPS NOAA-20
Launch	October 2011	November 2017
Spectral Coverage	300 – 380 nm	300 – 420 nm
Spectral Resolution	1 nm	1 nm
Spatial Resolution at Nadir*	50 × 50 km^2	17 × 17 km^2 (launch – 02/2019) 12 × 17 km^2 (02/2019 – present)

* The OMPS nadir mapper on JPSS-2 (launch 2022) has a planned resolution of 10 × 10 km^2.

3. OMPS Formaldehyde Retrievals

- The Smithsonian Astrophysical Observatory (SAO) OMPS retrieval is based on our operational OMI HCHO retrieval, which is also the basis for future TEMPO retrievals.
- The SAO HCHO product uses a 3-step approach:
  1. Fit a slant column of HCHO for each spectrum using a cross-track dependent reference spectrum from a clean area over the Pacific.
  2. Determine an air mass factor and convert to vertical column.
  3. Adjust the background using a modeled column over the Pacific.

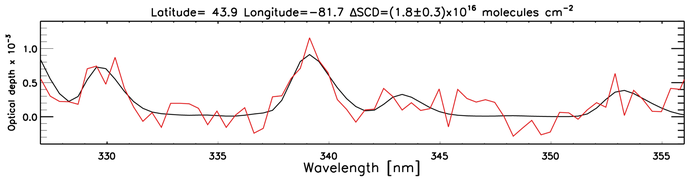

Figure 1: Simulated (black) and observed (red) optical depth of HCHO from a single OMPS Suomi NPP spectrum (González Abad et al., 2016).

4. OMPS HCHO from Suomi NPP and NOAA-20

We are producing a multi-year HCHO dataset from OMPS on Suomi NPP and NOAA-20.

- A multi-year Version 1 product should become available mid-2020. Users can download from a dedicated publicly-accessible SAO website.
- The OMPS Suomi NPP algorithm will be integrated into the NASA Science Investigator-led Processing Systems, with the HCHO product eventually provided by NASA.

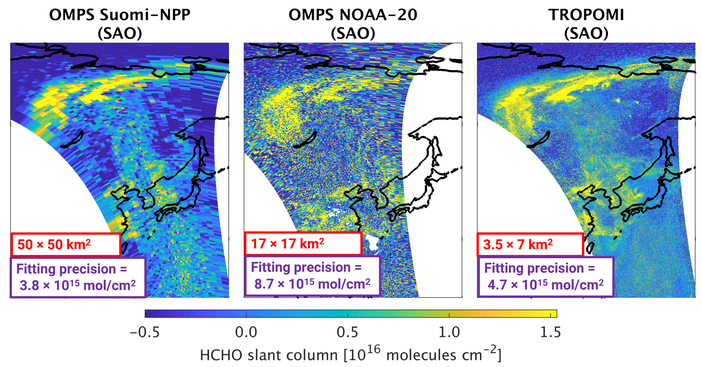

Figure 2: Fitted HCHO slant columns from OMPS/Suomi-NPP, OMPS/NOAA-20 and TROPOMI (using SAO algorithm) for orbit passing over East Asia and a Siberian fire on 4 July 2018. All observations (clear and cloudy) are shown. Because OMPS Suomi NPP spectra are spatially averaged on-board, observations are at a coarser spatial resolution than those from OMPS NOAA-20, and fitting uncertainties are lower. NOAA-20 operates 50 minutes ahead of Suomi NPP. The ESA/KNMI TROPOMI instrument was launched in October 2017 into an orbit 5 minutes behind Suomi NPP. Its observations are of high spatial resolution and have low fitting uncertainties due to high instrument signal-to-noise.

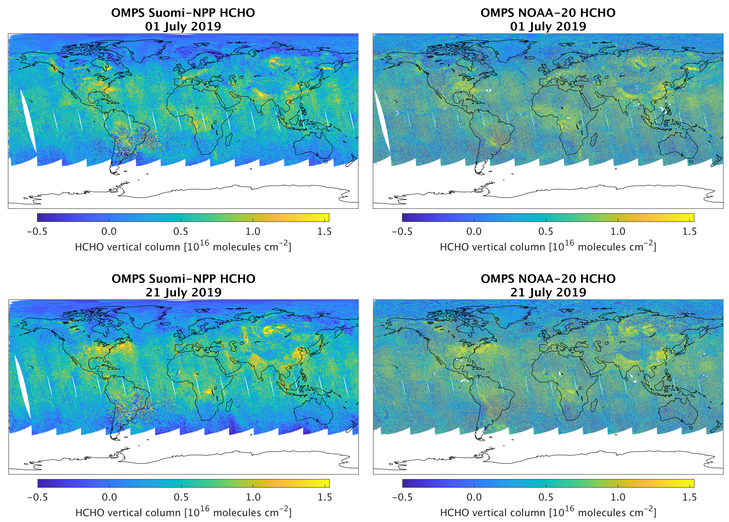

Figure 3: Global HCHO vertical columns observed from OMPS/Suomi-NPP and OMPS/NOAA-20 for all orbits on 1 and 21 July 2019. Cloudy and clear observations are included. Several areas of enhanced HCHO are clearly visible, including over fires in Spain, Russia, Canada, the US, South America and Africa, and from anthropogenic emissions in China.

5. Validation

- We are validating the retrieval using airborne data from multiple field campaigns through indirect validation with a model as an intercomparison platform (Zhu et al., 2016).
- Zhu et al. (2020) have prepared the validation framework using 12 campaigns, initially applied to OMI HCHO retrievals.
- Figures 4 – 6 show an example for OMPS/Suomi-NPP from the May-June 2016 KORUS-AQ campaign over South Korea.

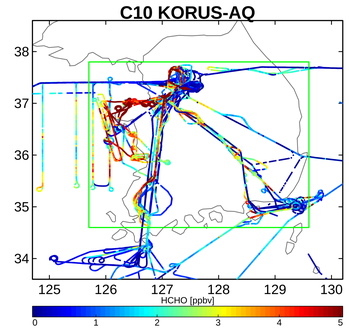

Figure 4: HCHO mixing ratio measured in situ by the CAMS instrument on the DC-8 aircraft over South Korea during the KORUS-AQ campaign in May-June 2016. All altitudes are shown (0-7.5 km). The green rectangle indicates the validation region.

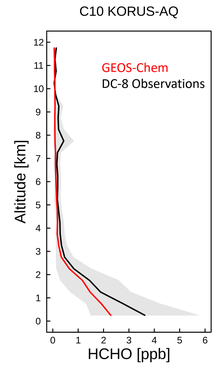

Figure 5: Mean mixing ratio profiles from observations (CAMS) and a coincidentally-sampled model (GEOS-Chem) for the entire KORUS-AQ campaign. Here, GEOS-Chem underestimates the column by 31%. The model is later scaled using the ratio of the observed to modeled column so that it can be compared with OMPS and OMI.

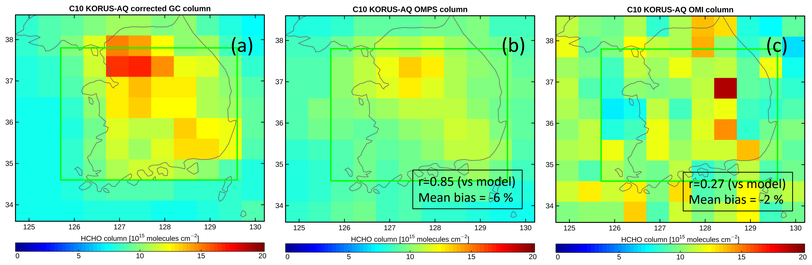

Figure 6: Mean vertical column HCHO during KORUS-AQ at satellite overpass time on a 0.5°x0.5° grid from a) GEOS-Chem scaled to match mean in situ observations (above); b) OMPS/Suomi-NPP; and c) OMI. OMPS shows a much better spatial correlation than OMI with the model, due partly to the OMI row anomaly and missing data from an OMI instrument outage during the campaign.

References

González Abad et al., Smithsonian Astrophysical Observatory Ozone Mapping and Profiler Suite (SAO OMPS) formaldehyde retrieval, Atmos. Meas. Tech., 9, 2797-2812, 2016.

Zhu et al., Observing atmospheric formaldehyde (HCHO) from space: validation and intercomparison of six retrievals from four satellites (OMI, GOME2A, GOME2B, OMPS) with SEAC⁴RS aircraft observations over the southeast US, Atmos. Chem. Phys., 16, 13477–13490, 2016.

Zhu et al., Validation of satellite formaldehyde (HCHO) retrievals using observations from 12 aircraft campaigns, Atmos. Chem. Phys. Discuss., 2020, under review.

Acknowledgments

This work is supported by NOAA grant NA18OAR4310108 (AC4) and NASA grants 80NSSC18K0691 (TASNPP) and 80NSSC18M0091 (MEaSUREs).

A51R-2655

Ozone recovery as detected in NOAA Ground-Based and Satellite Ozone Measurements

J. D. Wild[1], I. Petropavlovskikh[2,3], A. McClure[2,3], K. Miyagawa[3], B. Johnson[3], C. Long[4], S. Strahan[5] and K. Wargan[6]

[1] University of Maryland Earth, System Science Interdisciplinary Center, College Park, MD, [2] CIRES, University of Colorado, Boulder, CO, [3] NOAA ESRL, Global Monitoring Division (GMD), Boulder, CO, [4]NOAA Science Center, College Park, MD, [5]Universities Space Research Association, NASA GSFC, Greenbelt, MD, [6] Science Systems and Applications, INC, NASA GSFC, Greenbelt, MD

1. Introduction.

The 1987 Montreal Protocol and its 1990 amendments to the US Clean Air Act require NASA and NOAA to monitor ozone and the reduction of ozone depleting substances (ODS). The 2018 WMO/UNEP Ozone Assessment and the SPARC/WMO/IO3C Long-term Ozone Trends and Uncertainties in the Stratosphere (LOTUS) special report indicate that the extent of ozone recovery is geographically diverse. These studies focused on Multi-linear Regression analyses (MLR) optimized for broad latitudinal bands. NOAA's ground-based instruments (GB) include Dobson total column ozone observations, vertical distribution of ozone from Dobson Umkehr and ozonesonde profiling. Additionally NOAA's homogenized satellite record from SBUV, SBUV/2 and OMPS provide information on ozone vertical distribution globally allowing the study of large scale ozone variability. The meteorological models MERRA2, GFS and the GMI chemistry transport models allow the exploration of diurnal variability in the satellite records and the tracking of air parcels relevant to the representativeness of the GB data. This study aims to revise historical WMO GAW and NOAA Umkehr records with improved stray light corrections. Overpass data are generated for the NOAA GB sites using the combination techniques of the NOAA Cohesive (SBUV COH) zonal ozone product. This project is aimed at comparing ozone variability and trend in regional (i.e. GB station, satellite overpass) and zonally averaged data.

2. N-value correction optimized using the M2GMI simulation.

Dobson Umkehr measurements are made by tracking relative differences in zenith sky intensities from two UV wavelengths between the horizon and 70-degrees Solar Zenith Angle (SZA). The ratio of the zenith sky intensities are converted to N-values, $100*\log_{10}(I_{332.4}/I_{310.5})$. Large differences between the observed and modeled N-values are found in the volcanic eruption periods (1982-1984, 1991-1994). Modeled corrections are based on M2GMI model ozone profile data matched to the Umkehr observations.

Umkehr Retrievals (Operational) and Stray light corrections

Dobson Umkehr measurements are made using information from the C wavelength pair (311.5, 332.4 nm). The algorithm for ozone retrieval, UMK04 (Petropavlovskikh et al., 2005, is used for operational data processing (WinDobson).

The operational Umkehr ozone profiles are biased relative to other ozone observations, i.e. SBUV record (Petropavlovskikh et al., 2011). The updated algorithm takes into account the standardized stray light correction (dNslc):

$$N_{slc} = N(w, Z) + dNslc(O_3, P, Z)$$

where dN_{slc} is estimated from look-up tables that are dependent on latitude, altitude (p), solar zenith angle (Z), and total ozone (O_3).

Optimization with the M2GMI model

Re-alignment of Dobson optical system (wedge) and instrument replacements can create step changes in Umkehr data. The optimization process involves the use of empirical corrections to reduce differences between observed and simulated Umkehr data, and serves to homogenize the time series (Fig.1 and 2). The Umkehr simulations are based on ozone profiles from the independent datasets, i.e. NDACC ozonesonde, lidar, and MW, SBUV/OMPS COH record, and GMI CTM (Strahan et al, 2016) and M2GMI models (Wargan et al, 2018).

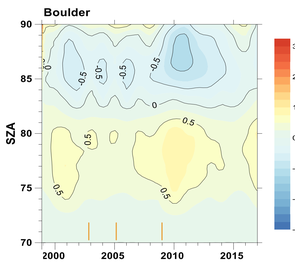

Figure 1. Optimized correction of Umkehr N value for Boulder (BDR, 40 N, 105 W) as function of time and SZA. The difference between observed N-values and those simulated based on M2GMI ozone porifles is shown as a function of time (monthly mean) and SZA.

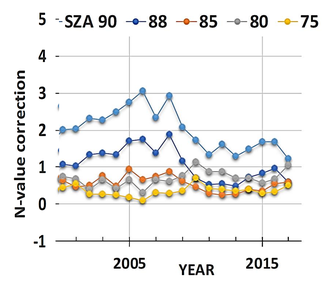

Figure 2. Optimized correction of Umkehr N value for Boulder is shown as function of time at several solar zenith angles (SZA). Umkehr empirical correction for volcanic aerosol period shows strong dependence on SZA

2. SBUV COH time series and overpass data.

The Solar Backscatter Ultraviolet (SBUV and SBUV/2) instrument onboard NASA and NOAA satellites have provided 40 years of continuous ozone profile data (1978 – present). OMPS on Suomi National Polar-orbiting Partnership (S-NPP), NOAA-20 and successor satellites continues this series using a retrieval algorithm similar to SBUV. The SBUV&OMPS COH dataset combines data from these instruments removing small residual differences by examination of overlap periods. The resulting profile product is a set of daily or monthly zonal means publically available at ftp.cpc.ncep.noaa.gov/SBUV_CDR. The corrections to remove the instrumental differences are determined by an examination of the overlap period for each zone and level (or layer). An overpass SBUV&OMPS COH has been produced by applying the adjustments for the relevant zone to SBUV and OMPS profiles extracted within proximity to the ground measurement site. For this study, we collect satellite profiles within 2° latitude and 20° longitude of the site.

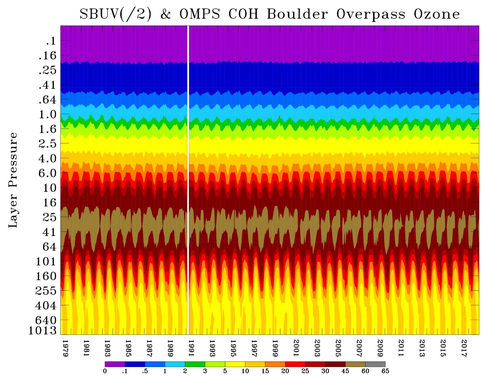

Figure 3. A contour plot of the COH ozone profile time series selected for the overpass criteria: a monthly average of all data within the +-2 degree latitude, and +- 20 degree longitude, centered at Boulder, CO station (40 N, 105 W).

3. Satellite and model comparisons.

Validation of optimized Umkehr RT.

The optimized Umkehr ozone processing includes multiple N-value adjustments for each of instrument calibration periods as in Figure 4 where arrows at the bottom indicate dates of the applied corrections and during volcanic eruptions shown as yellow colored periods.

The changes in the Umkehr Boulder record are assessed through comparisons to M2GMI, GMI CTM and several satellite datasets (Aura MLS, aggregated SBUV series and JPSS OMPS V8PRO).

Figure 4 also shows comparisons of optimized Umkehr data and the M2GMI model where seasonal to sub-seasonal biases are +/-2 % and the long-term mean bias is 0%. Figure 5 shows comparisons with other datasets.

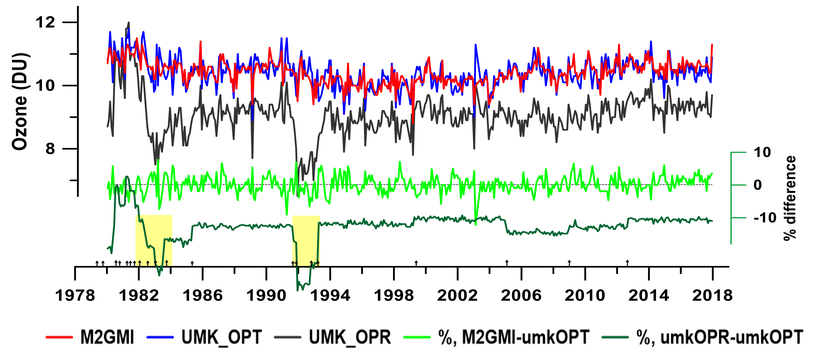

Figure 4. The time series of ozone at Boulder in Umkehr layer 8 (2-4 hPa). Operational Umkehr (black), Optimized Umkehr (blue) and M2GMI (red) data are shown as monthly averages. Difference between Optimized and Operational Umkehr data is shown as a dark green line. The percent difference between optimized Umkehr and M2GMI model is shown as a light green line. The arrows at the bottom indicate dates of Dobson calibrations and instrument replacements.

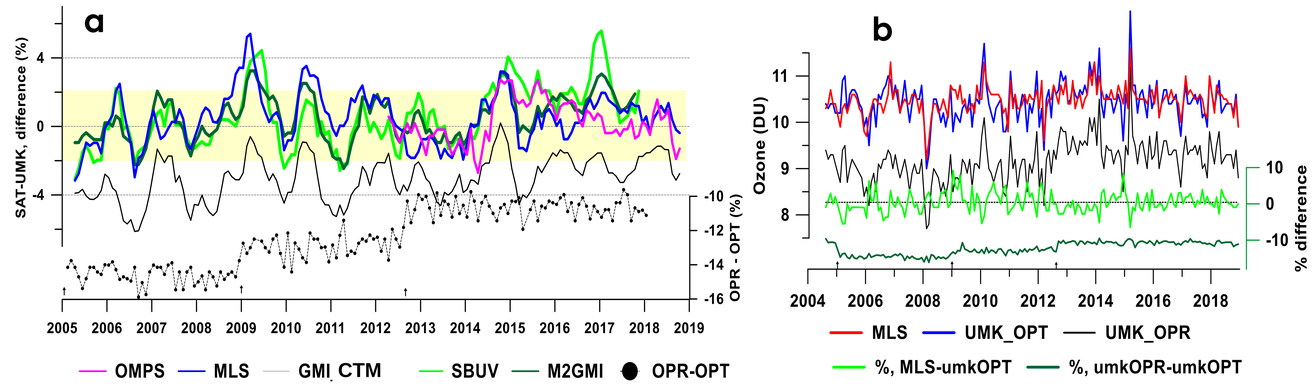

Figure 5. **a)** The 5-month smoothed difference of optimized Umkehr and measured/modeled ozone over Boulder, Umkehr layer 8 (2-4 hPa). The difference is calculated relative to the optimized Umkehr data. The data sets include: M2GMI simulated ozone (dark green), GMI CTM (black), Aura MLS (blue), SBUV aggregated (light green) and JPSS S-NPP OMPS (pink). The difference between optimized (UMK_OPT) and operational Umkehr (UMK_OPR) data is shown with dotted-dashed black line. **b)** similar to **a)**, but focused on Aura MLS 2004-2018 comparisons with operational and optimized Umkehr data.

4. Summary and Discussion

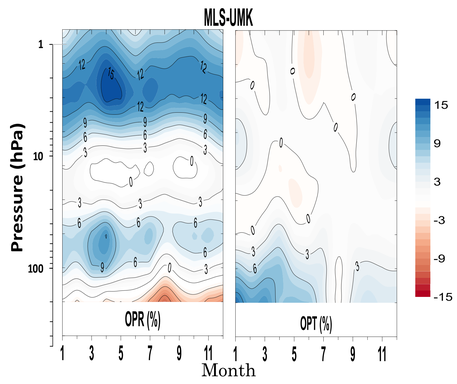

Figure 6. Seasonal biases between the Umkehr measurements in Boulder and the Aura MLS satellite overpass record. Two panels show results for Umkehr retrievals: operational (left), Optimized correction (right). The biases are significantly reduced after the Optimized Umkehr correction.

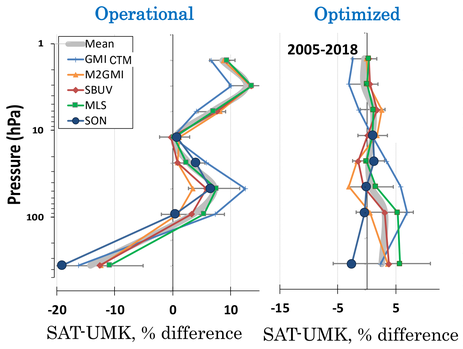

Figure 7. Biases in M2GMI, GMI CTM, SBUV, Aura MLS, and ozonesondes are shown with respect to the operational (left panel) and optimized (right panel) Umkehr profiles at Boulder, CO. Averages are done for 2005-2018. The mean bias is shown with light grey thick line.

Findings

- Umkehr mean bias is reduced after optimization (Figs. 6 & 7).
- Seasonal biases are still present and need to be investigated (Fig. 6).
- Mean bias of 5 % is found between M2GMI and GMI CTM in the stratosphere (Fig. 5a & Fig. 7)
- Very similar models (MERRA2 winds and chemistry), biases in the upper stratosphere need to be understood better (Fig. 7, i.e. Stauffer et al, 2019).

Nest Steps

- Residuals of the Umkehr retrieval (delta N-value) need evaluation to verify improvement in the Umkehr measurement fit.
- Other Umkehr stations will be optimized and verified against other instruments including lidar, FTIR and Microwave.
- Examine variability of SBUV COH overpass and GB records in the context of overpass selection criteria, atmospheric dynamics, and representation in Equivalent Latitude
- Optimize the LOTUS statistical trend model for GB and overpass datasets testing the need to include additional proxies

Using Machine Learning to Assimilate Precipitating Pixel Information from GOES ABI and GLM

Kyle Hilburn [1], Imme Ebert-Uphoff [2], and Steve Miller [3]

[1] Kyle.Hilburn@colostate.edu

[1,2,3] Cooperative Institute for Research in the Atmosphere (CIRA)

[2] Department of Electrical and Computer Engineering (CSU)

Introduction

Motivation: How can we get the maximum benefit from GOES observations for forecasting?

- **Radiance assimilation** is physically-based (easy to interpret), but individual pixel information content saturates around optical depths of 160(8) during day(night) or composite reflectivity (**REFC**) of 20-25(0-5) dBZ, and does not use lightning information
- **Machine learning** is statistically-based (harder to interpret), but image gradients and spatial context provide reliable information to about 45 dBZ, and provides framework for using lightning information (*data fusion*)

Question: what is our neural network (**NN**) learning that provides such good skill?

Hypothesis: the skill comes from using information in *image gradients and lightning*

Data

- GOES-16 Advanced Baseline Imager (**ABI**)
  - Channel 7, 3.9-micron, shortwave infrared window
  - Channel 9, 6.9-micron, mid-level water vapor (~442 mb)
  - Channel 13, 10.3-micron, clean longwave infrared window
- GOES-16 Geostationary Lightning Mapper (**GLM**)
  - Group extent density
- Multi-Radar Multi-Sensor (**MRMS**) Quality-Controlled Composite Reflectivity
- All fields are resampled to 3-km Lambert Conformal Conic HRRR grid

Dataset Construction

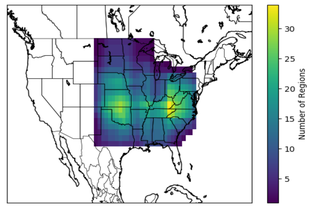

- Selected samples from the 92-day period 4/17/2019 to 7/17/2019 during which there was abundant severe weather.
- *Automatically select regions- and times-of-interest* based on maximizing the number of **SPC storm reports** (tornado, hail, wind)
  - 6-hour periods with 15-minute refresh
  - 256 x 256-pixels on 3-km HRRR grid (768 km)
- Mode of 20-50 storm reports per day
- **Top panel**: geographic preference for Southern Great Plains and Upland South
- **Bottom panel**: temporal preference for mid to late afternoon
- Split: 80% / 20% for training / validation
- An independent training dataset (*Hilburn et al., JSC 2019*) that includes nighttime and other locations produces similar results

Analysis Methodology

Our approach is to produce many models and interrogate them in order to open the lid of the "black box" and identify the strategies the NN is using that produce such good skill.

- **Channel withholding experiments** to identify the information content that is most important for producing skill in certain situations
- Comparing results using standard 3x3 convolutional filters with **1x1 filters** in order to remove the spatial context and simulate an approach considering just individual pixels
- Use of **attribution methods**, such as Layer-wise Relevance Propagation, to visualize what information the NN is using to make a specific prediction
- Use of **synthetic inputs** to quantify the sensitivity of the output to variations in properties of the inputs
- Use of **metrics** that are unrelated to the loss function (MSE), such as: coefficient of determination (R^2), categorical metrics at various output threshold levels (POD, FAR, CSI, Bias), and evaluation of the MSE binned over the range of true output values

Architecture

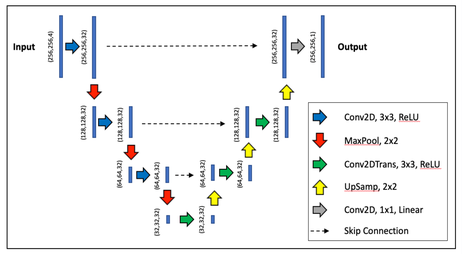

- Sequential structure based on **U-Net**
- Skip connections off: they provide very small improvements but complicate visualization
- 3 encoding and decoding layers, *deeper produces overfitting*
- 32 filters per layer, fewer do nearly as well but give blurry output
- 100 epochs validation statistics:
  - RMSD = 5.29 dBZ
  - R^2 = 0.738

This model has 47,457 trainable parameters.

Loss Functions

- Standard unweighted MSE loss function has *sub-optimal performance at high REFC*
- REFC PDF ~ Exp(-5*y) where y=[0,1]
- Use performance diagram (**right**) to select loss function weights producing minimum bias
- Also select model (different random seeds)
- *Generalized exponential*: Wt = Exp(b*y^c)
- The optimal coefficients (grid search) are b=5 and c=4 (for MSE) and c=3 (for MAE)
- Connection to AUC approach but without derivative problems
- Acts as a global constraint on realism of fields

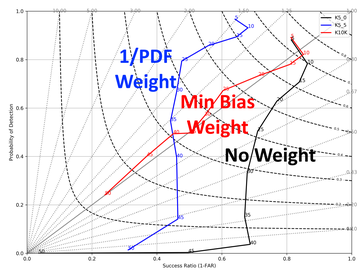

Performance for REFC: 0, 5, 10, … 50 dBZ

Results for Validation Sample 2019-07-02 23:30Z

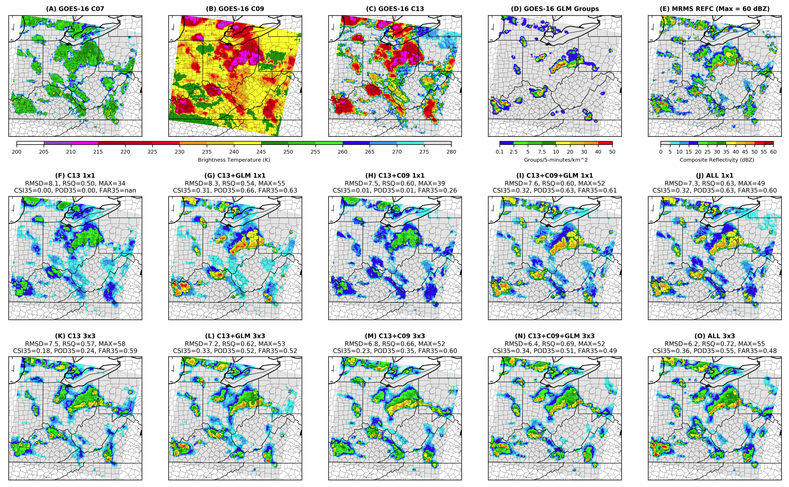

Top row: GOES inputs (**Panels A-D**) and MRMS truth (**Panel E**)
Middle row: Predictions with 1x1 filters for various channel combinations
Bottom row: Predictions with 3x3 filters for various channel combinations

Importance of Gradients and Spatial Context

Traditional infrared imager retrievals of precipitation, which only use individual pixel information or rudimentary spatial information, have poor skill (low POD and high FAR).

- **Panel F** simulates that type of algorithm, which has poor skill at REFC > 20 dBZ
- Adding water vapor (**Panel H**) helps a little bit, but not enough at high values

Allowing the NN to use gradient information and spatial context provides tremendous improvements in skill.

- **Panel K** shows that *even with just C13, image gradients and spatial context carry a great deal of information about REFC > 35 dBZ*
- Note that RMSD and R^2 tell a limited story, and that *categorical statistics are crucial* for evaluating whether a model provides improvements
- Adding water vapor (**Panel M**) helps increase the POD in areas where the difference between C09 and C13 is small, but does this *at the expense of a high FAR*

Importance of Lightning

Given that gradients carry so much information, to isolate the importance of lightning, consider the 1x1 experiments.

- Adding lightning (**Panel G**) *provides dramatic improvements for REFC > 35 dBZ* but note that values between 20-35 dBZ are mostly absent

When gradients are included, lightning provides less relative value, but it still has unique characteristics.

- **Panel L** shows that combining lightning with C13 provides *dramatic improvements in POD* (0.52 vs 0.24) with reasonable FAR (categorical bias is near one)
- Unlike water vapor (**Panel M**) lightning is better able to *pinpoint locations of strong radar echoes* and provides dramatically better POD (0.52 vs 0.35)
- **Panel O** shows that *other channels work together with lighting to provide the best estimates* with sharp, well defined convective core features

The properties illustrated in this example of the skill provided by lightning and image gradients are confirmed in statistics across all validation samples.

Layer-wise Relevance Propagation

- **Top set**: results with lightning
- **Bottom set**: lightning zeroed out
  - **Top rows**: input fields
  - **Middle rows**: image gradients
  - **Bottom rows**: heatmaps
- Uses LRP with alpha=1 and beta=0
- NN uses the lightning value itself more than the lightning gradient (**top set**)
- Without lightning (**bottom set**), the network uses strong infrared gradients
- With lightning, *the emphasis for the other channels is changed*, looking at gradients in locations with lightning
- While the LRP percentage of lightning is only 12.9% in this case, it impacts the interpretation of the other channels, *giving the NN additional clues of where to look*, yielding a more accurate estimate of REFC
- A *remaining question* is how does the NN learn which strong gradients to ignore and which are important?

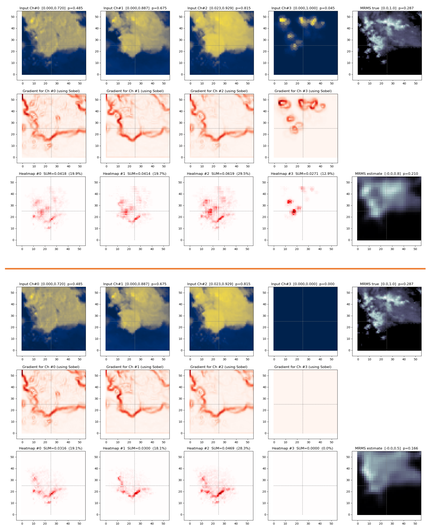

Synthetic Inputs

- Using a *sum of Generalized Elliptical Gaussians* model that provides six parameters for the inner and outer Gaussians: 1) location, 2) amplitude, 3) size, 4) aspect, 5) orientation, and 6) sharpness (exponent)
- Evaluating 45K+ different parameter settings, the spatial patterns that most strongly activate the NN, based on maximum REFC, all resemble that shown to the **right** (**top**: synthetic input, **middle**: NN output)
- The NN has learned about *thunderstorms with overshooting tops* (OT)
- Note the *very strong gradients* along the anvil edge and along the OT edge, corresponding to large exponents
- The weakest responses have in common weak gradients and are the least physical looking
- Evaluating all the model parameters, the most influential are the inner and outer Gaussian sharpness
- An example of the sensitivity is given in **right bottom** panel, which shows the maximum REFC as functions of the inner and outer exponents
- The emergence of 35 dBZ echoes requires the outer exponent to be 1 or greater, or very large inner exponents around 8

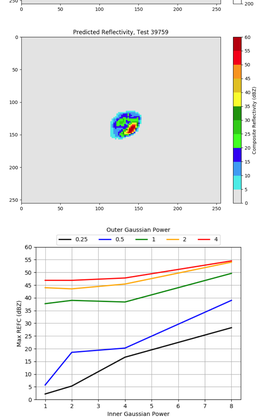

Summary and Conclusions

- We have shown that a convolutional NN trained on *GOES ABI+GLM can accurately reproduce composite reflectivity* from MRMS over eastern CONUS warm season
- We have shown the skill comes from *gradients in infrared images and lightning* and that lightning helps the network better interpret radiance gradients
- We used *novel approaches* to derive weights for the loss function and in our analysis methodology to evaluate the importance of image gradients and lightning
- A *remaining question* is how applicable will this NN be to different meteorological regimes, such as tropical convection, and what additional meteorological information will be needed to produce robust predictions globally?
- However the *tools developed* in this work will be applied to investigate those questions
- **Goal**: GOES-derived synthetic reflectivity profiles used where ground-based radar network coverage is poor for the RAP/HRRR latent heating initialization/assimilation
- Additional details about this work will appear in *Hilburn et al. (2020, JAMC in preparation)*

Acknowledgements

- Thank you to the **GOES-R Program**; this research is support by award NA19OAR4320073
- Thank you to **NOAA RDHPCS** for access to the Fine Grain Architecture System on Hera, without which this research would not have been possible

Development of a Machine Learning-Based Radiometric Bias Correction for NOAA's Microwave Integrated Retrieval System (MiRS)

Yan Zhou[1], C. Grassotti[1], R. Honeyager[2], Y.-K. Lee[1], S. Liu[3], Xingming Liang[1], F. Ming[4]

1. CISESS/UMD 2. JCSDA/UCAR 3. CIRA/CSU 4. IMSG Inc.

Contact: yanzhou@umd.edu

Background & Motivation

- The **M**icrowave **I**ntegrated **R**etrieval **S**ystem (**MiRS**) is NOAA's operational microwave-only satellite retrieval system. It aims to provide a single consistent source for many microwave retrieval products, such as vertical profiles of temperature and moisture, from different satellites with various instrumental configurations.
- MiRS relies on a forward model, the **C**ommunity **R**adiative **T**ransfer **M**odel (**CRTM**), to provide simulated radiances and implements a one-dimensional variational (1DVAR) algorithm to determine the atmospheric state which best fits the radiometric measurements.
- The current radiometric bias correction uses a Histogram Adjustment Method, which performs well at characterizing the average global differences between measurements and retrievals (static method). However, the local variations of systematic errors in CRTM are not accounted for.
- New method: a machine learning-based approach to the radiometric bias correction, a **N**eural **N**etwork (**NN**).
- The goal of using NN is to learn the bias structure from historical collocations of observed and simulated brightness temperatures, along with the estimated corresponding atmospheric and surface state. The NN model, once trained, can then be used in near real time for bias correction during the MiRS retrieval process.

Methodology

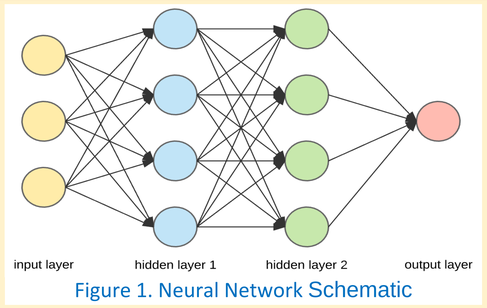

Figure 1. Neural Network Schematic

A NN has been developed for ATMS/SNPP. The architecture is:

- Number of hidden layers: 2
- Number of neurons (or nodes) in each hidden layer: 200
- Activation function: Rectified Linear Unit (ReLU)

Input features:

- Brightness temperature (TB) of the measurements,
- Satellite viewing angle,
- latitude,
- other geophysical parameters such as cloud liquid water (CLW), total precipitable water (TPW), and skin temperature (Tskin).

Output:

- Brightness temperature bias

Training: 12-days dataset

- Jan-14, Feb-15, Mar-25, Apr-01, May-11, Jun-04, Jul-15, Aug-01, Sep-01, Oct-20, Nov-01, Dec-01

Testing: 20191001

NN Results

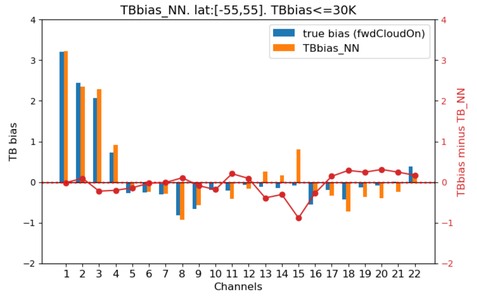

Figure 2. Mean TBbias of each ATMS channel, for latitude [55^{O}S-55^{O}N], when true TBbias is less than 30K.

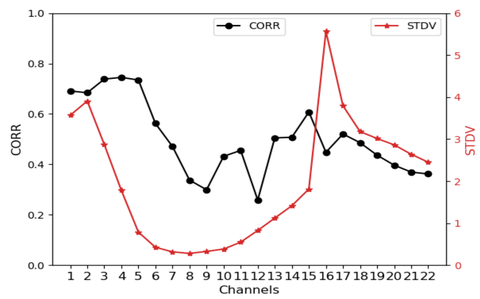

Figure 3. Correlation (black) and standard deviation (red) of TBbias, NN vs. true. For latitude [55^{O}S-55^{O}N], when true TBbias is less than 30K.

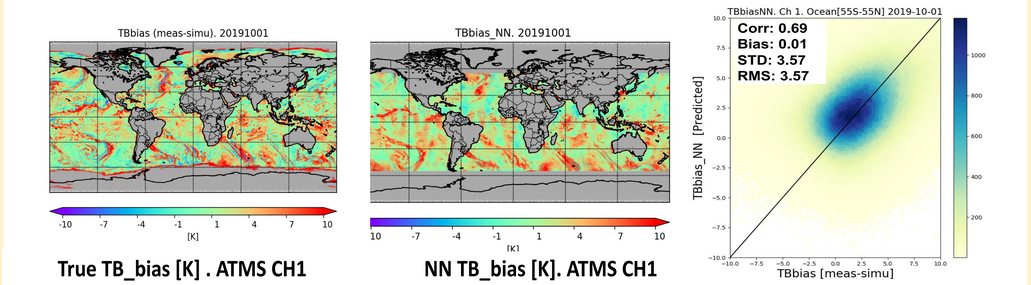

Figure 4. NN TBbias verification for ATMS/SNPP Channel 1 (23.8GHz). Latitude [55^{O}S-55^{O}N], true TBbias is less than 30K.

MiRS Retrieval Results

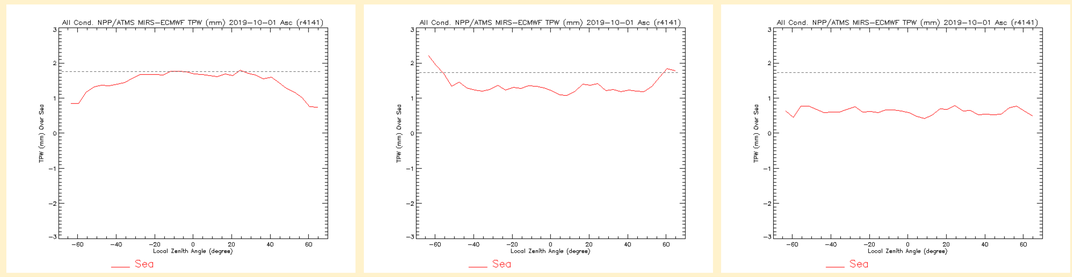

Figure 5. Figure 5. MiRS TPW Over Ocean. From left to right: Static, Perfect, and NN experiments

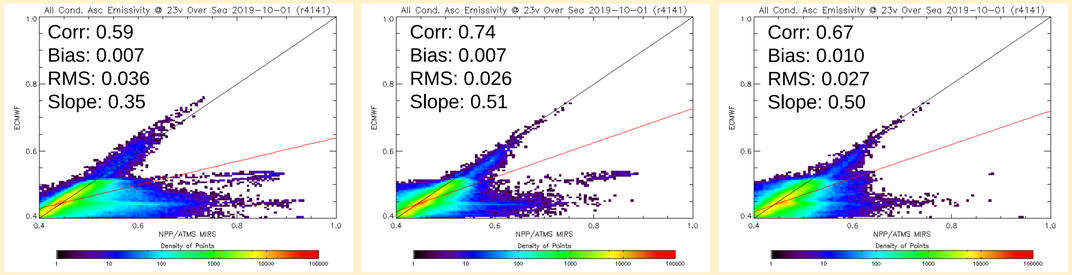

Figure 6. MiRS Emissivity Over Ocean (23.8GHz). From left to right: Static, Perfect, and NN experiments

MiRS Retrieval Results (*cont.*)

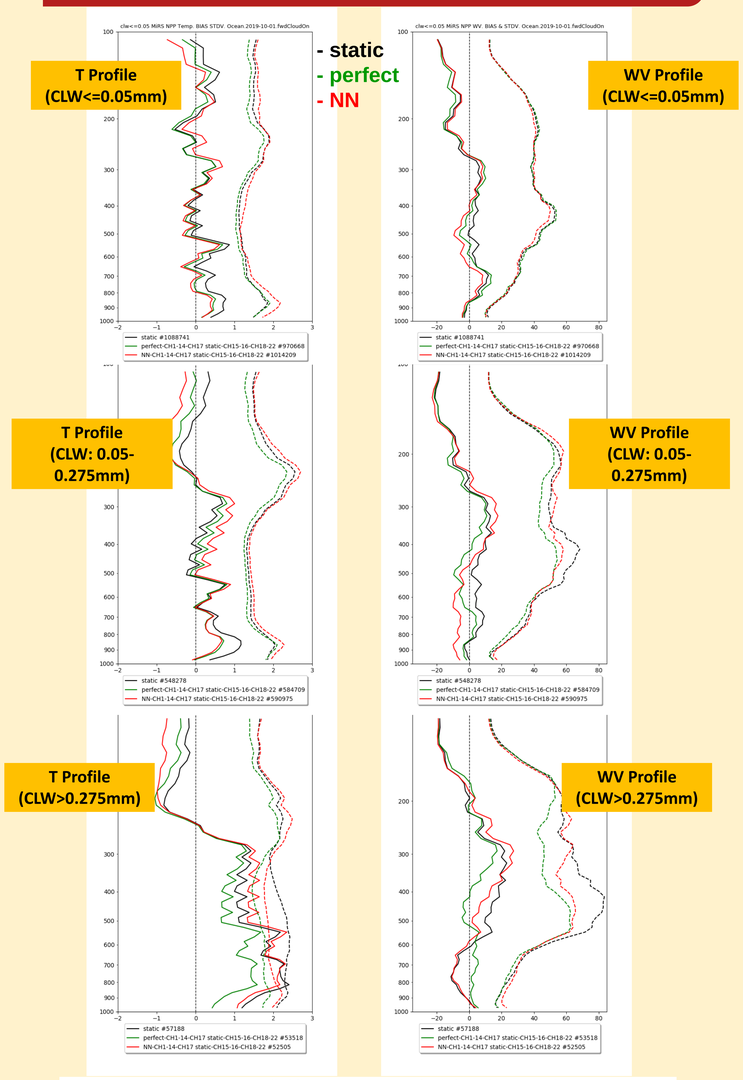

Figure 7. MiRS temperature (left) and water vapor (right) profiles stratification by CLW

Summary & Future Works

- A new NN-based approach to estimate the observed TB bias structure was developed. The NN represents TB bias very well, at least for surface channels such as 23.8GHZ (Figure 4), and for water vapor channels at 183.31GHz (not shown).
- Applying either true or NN-estimated TBbias to MiRS leads to generally positive impact on atmospheric temperature and water vapor profiles than static method (Figure 7). Significant improvement can be observed
  - for temperature bias where CLW is larger than 0.275mm, under 300hPa
  - for water vapor standard deviation where CLW is larger than 0.05mm, between 300-600hPa
- The TPW shows smaller bias and scan-dependency using NN-estimated TBbias (Figure 5).
- Future Works: Improving NN is possible by using more channels, such as 23.8GHz (Figure 6), by fine-tuning of the NN architecture, such as number of hidden layers, nodes, and activation functions (Undergoing).

Airborne Demonstration of Next-Gen Imaging Infrared Sounder Capabilities and Algorithms

Joe K. Taylor, D. C. Tobin, F.A. Best, R. K. Garcia, R.O. Knuteson, H.E. Revercomb, W.L. Smith Sr., E. Weisz, and S-HIS Team
Space Science and Engineering Center, University of Wisconsin-Madison, 1225 West Dayton St., Madison, WI, 53706

2020 JPSS GOES Proving Ground / Risk Reduction Summit

Introduction

Airborne instrumentation and measurements are a valuable resource for development, test, and demonstration of next-generation technology and algorithms. The Scanning High-resolution Interferometer Sounder (S-HIS) has demonstrated state-of-the-art performance and excellent robustness and reliability over 20-years of operation on 35 missions around the globe, and has earned recognition as an infrared calibration reference standard for satellite calibration validation.

The current S-HIS measurement capability provides highly accurate spectrally resolved infrared radiances with relatively small spatial footprints at high spectral resolution and contiguous spectral coverage. These measurement qualities can be leveraged for algorithm development and testing for next-generation LEO and GEO high spectral resolution imaging infrared sounders. The S-HIS measurements can also be used with SRF convolution for spectral band assessment for the next generation IR imagers. Co-located measurements from other instruments in the payload are often useful for product assessment.

Furthermore, the UW-SSEC is conducting a study to (1) define what is required to maintain the current capability of the S-HIS into the future, (2) identify enhanced capabilities enabled by new technologies and guided by science community consensus on key questions posed by NASA and and NOAA, and (3) identify sources of funding and a consistent development approach for various upgrade scenarios.

S-HIS: Next Generation Capabilities

Enhancement of the S-HIS capabilities can be enabled by upgrading the instrument with new technologies such as (but not limited to):

- An independent On-board Absolute Radiance Standard. This technology has been developed for the UW-SSEC Absolute Radiance Interferometer and an airborne version for the S-HIS would allow for traceability to absolute references via end-to-end calibration verification in-flight, as well as improved detector nonlinearity characterization and correction, and reduced radiometric uncertainty.
- Improved spatial resolution via the integration of a detector array and conversion of the instrument to an imaging FTS. The next generation LEO and GEO sounders will move to improved spatial resolution and will benefit from technology and algorithm demonstration. Additionally, improved S-HIS spatial resolution will enable a wider breadth of research and applications.
- Improved spectral coverage and/or improved spectral resolution. Spectral coverage beyond our current spectral limits and/or finer spectral resolution would allow additional research opportunities and applications.
- A bore-sighted sub-pixel imager (infrared microbolometer FPA). A bore-sighted high spatial resolution infrared imager would provide additional scene information within the FTS footprint at a relatively low cost.
- Enhanced on-board processing to facilitate the imaging FTS and sub-pixel imager capabilities.
- Upgraded instrument electronics based on small-sat technology to further increase reliability and reduce instrument power and size.

Possible Interferometer Core Options Include both Large Aperture Prototype and Compact COTS

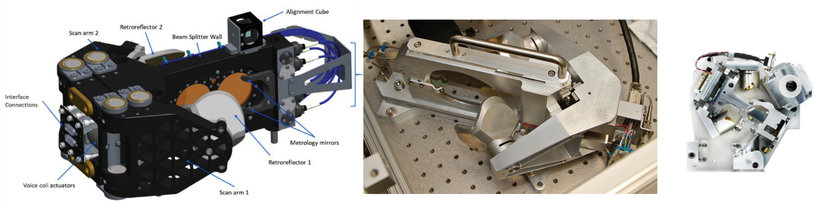

Sub-pixel Imager:
FLIR Boson
IR Microbolometer Core

Absolute Radiance Standard developed for ARI

Scale to S-HIS Aperture and modify design for airborne application

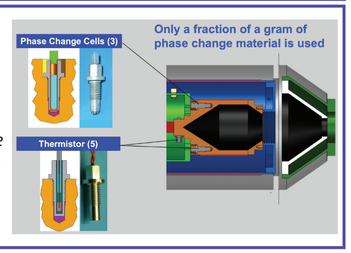

S-HIS: Current Capability and Existing Measurements

The Scanning High-resolution Interferometer Sounder (S-HIS) measures emitted thermal radiation at high spectral resolution between 3.5 and 17.3 microns (580 – 2850 cm^{-1}) at 0.5 cm^{-1} spectral sampling resolution with 0.100 radians angular field of view (2 km footprint from 20 km observing altitude) and imaging accomplished via cross-track scanning. Since 1998, the S-HIS has participated in 35 field campaigns on the NASA ER-2, DC-8, Proteus, WB-57, and Global Hawk airborne platforms. The S-HIS has proven to be extremely dependable with high calibration accuracy and consistent performance on all platforms. Applications of the S-HIS measurements have included radiances for evaluating radiative transfer models; temperature and water vapor retrievals; cloud radiative properties; cloud top retrievals; surface emissivity and temperature; trace gas retrievals; the characterization of the thermodynamic environment around hurricanes and tropical storms; the characterization of fire development, emission processes, plume evolution, and downwind impacts on air quality; and satellite calibration validation.

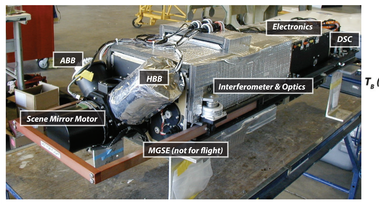

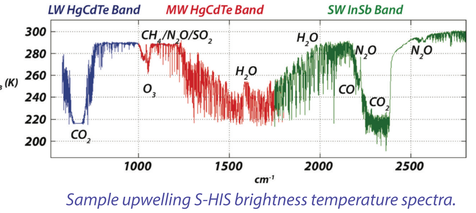

Sample upwelling S-HIS brightness temperature spectra.

S-HIS field deployment map, 1998 to present. Green circles indicate aircraft integration locations. (1) CAMEX, DC-8, 1998; (2) AirMISR 98, ER-2, 1998; (3) WINTEX, ER-2, 1999; (4) KWAJEX, DC-8, 1999; (5) WISC-2000, ER-2, 2000; (6) SAFARI 2000, ER-2, 2000; (7) AFWEX, DC-8, 2000; (8) TX-2001, ER-2, 2001; (9) CLAMS, ER-2, 2001; (10) IHOP, ER-2, 2002; (11) SMEX 2002, DC-8, 2002; (12) ARM UAV-SGP, Proteus, 2002; (13) TX-2002, ER-2, 2002; (14) Pacific THORpex, ER-2, 2003; (15) Atlantic THORpex, ER-2, 2003; (16) Tahoe 2004, ER-2, 2004; (17) INTEX Proteus, Proteus, 2004; (18) ADRIEX Proteus, Proteus, 2004; (19) EAQUATE, Proteus, 2004; (20) M-PACE, Proteus, 2004; (21) AVE-OCT04, WB-57, 2004, (22) AVE-JUN05, WB-57, 2005; (23) CR- AVE, WB-57, 2006; (24) Tahoe 2006, ER-2, 2006; (25) JAVIEX, WB-57, 2007; (26) TC-4, ER-2, 2007; (27) Railroad Valley, ER-2, 2011; (28) HS3, Global Hawk, 2011; (29) HS3, Global Hawk, 2012; (30) SNAP2013, ER-2, 2013 (31) HS3, Global Hawk, 2013; (32) HS3, Global Hawk, 2014 (33) SNAP2015, ER-2, 2015; (34) GOES-16 PLT, ER-2, 2017; (35) FIREX-AQ, ER-2, 2019. Map imagery courtesy of NASA Visible Earth, http://visibleearth.nasa.gov.

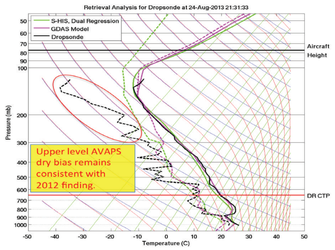

Example comparison of AVAPS Dropsonde and co-located S-HIS two-minute mean atmospheric state retrieval profiles. This example shows good retrieval despite upper level thin cirrus and lower level aerosol layers. AVAPS data since reprocessed and the upper level dry bias has been addressed.

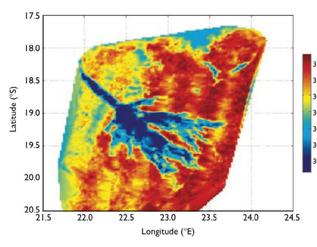

BT Map of the Okavango Delta, Botswana at 10.2 micron, acquired by Scanning-HIS during six parallel flight lines over the Delta on 27 August 2000 [King 2003].

Recent S-HIS datasets are available on the UW-SSEC data distribution website, and historical datasets are available on request. HS3, GOES-PLT, and FIREX-AQ data are also available via the mission data archives. Preliminary Level 1b (geolocated radiances) and Level 2 (temperature, humidity, and trace gas profiles) products are typically available within a few hours of data download during a mission. When a high bandwidth downlink is available for the aircraft, the Level 1 and Level 2 products can also be processed using a real-time ground data processing system that is capable of delivering atmospheric profiles, radiance data, and engineering status to mission support scientists via a web browser in less than one minute from the time of observation.

Calibration, Calibration Verification, and Traceability

- Pre-integration **calibration of on-board blackbody references** at subsystem level
- **Pre and post deployment end-to-end calibration verification**
- Periodic **end-to-end radiance evaluations under flight like conditions with NIST transfer sensors**.
- Instrument calibration during flight using **two on-board calibration blackbodies**

Pre and post deployment End-to-end Cal Verification 2007 - 2018

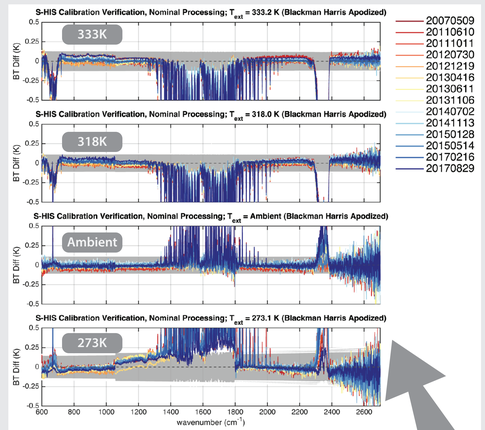

- Data acquired for external blackbody temperatures of ambient, 318K, 333K, and Ice Bath Blackbody
- Atmospheric emission/absorption not included in predicted BT (i.e. no LBLRTM)
- S-HIS NLC is optimized for 'flight' detector and instrument temperatures, not for laboratory temperatures
- 2013-04-16: Stirling cooler failing during testing and detector temperature increased to ~85K during calibration verification; primary impact is on MW nonlinearity (note the outlier spectra for Ice Bath blackbody.

NIST TXR Comparison

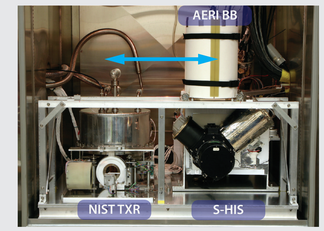

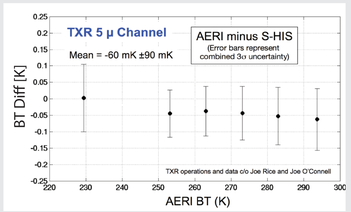

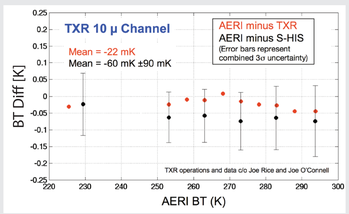

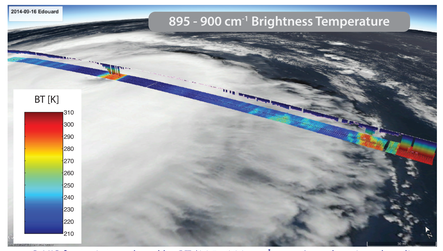

S-HIS footprints, colored by BT (895 - 900 cm^{-1} mean), and retrieved nadir temperature profile overlaid on VIIRS true color imagery (Hurricane Edouard, 16 Sept 2014). VIIRS images produced using polar2grid.

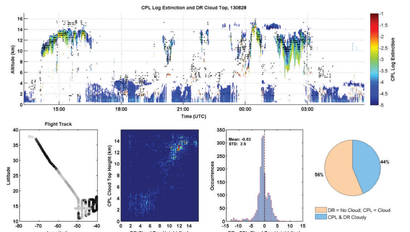

Example comparison of Cloud Physics Lidar (CPL) mean cloud top compared to S-HIS Dual Regression Retrieved Cloud Top Height product (2013-08-28 flight)

METOP-C Underflight Example (2019-08-19)

Near left:
S-HIS footprints (white outline)
IASI footprints (black outline)
Complete coverage of IASI footprints by S-HIS (red outline)

Far left:
895-895 cm^{-1} S-HIS BT
(17:20 – 18:15 UTC)

IASI Sub-sat line in red
ER-2 flight path in white

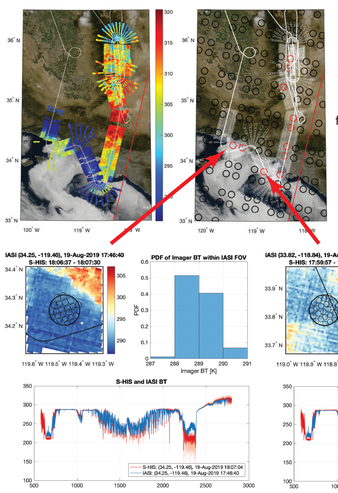

Low spatial variability within these IASI FOVs (IASI boresighted IR imager). GOES ABI data can be used to assess temporal stability between IASI and S-HIS time of observation for these FOVs

joe.taylor@ssec.wisc.edu, Space Science and Engineering Center, University of Wisconsin-Madison, 1225 West Dayton Street, Madison WI 53706 USA

JPSS NUCAPS Soundings Support (NWS) Forecasters

Anthony Reale[1], Bomin Sun[1,2], Nick Nalli[1,2], Michael Pettey[1,2], Arunas Kuciauskas[3] and Ryan Smith[1,2]

[1] NOAA/NESDIS/STAR, College Park, MD, USA; [2]I. M. Systems Group, Inc., Rockville, MD, USA, [3]Naval 5resrach lab, Monterey, CA

Abstract

NOAA Unique Combined Atmospheric Product System (NUCAPS) derived sounding products provide global observations of atmospheric temperature and moisture profiles in the troposphere (and stratosphere). These profiles have provide information useful to Local and regional weather forecasters in cases of severe weather. NUCAPS soundings from NOAA-20 and SNPP are routinely available to NWS field offices (mainly CONUS) via **AWIPS-2** with additional programs available / developing to distribute NUCAPS soundings outside CONUS … for example, recent JPSS / NWS sponsored workshops were held South America and Barbados with NUCAPS availability in the Alaska region and recently confirmed at GUAM. The following report provides a cross section of case studies demonstrating NUCAPS performance.

The NOAA Products Validation System (NPROVS, Reale et al. 2012), operated at NESDIS Office of Satellite Applications and Research (STAR), provides routine processing and archive of collocated **Conventional (WMO)** and **Special (targeted) Radiosondes** with various **Satellite Products** and **Forecasts**. These directly support of NOAA Joint Polar Satellite System (JPSS) calibration/validation program for NUCAPS and are leveraged in the case studies (retrospective) assessments shown below.

NOAA Products Validation System (NPROVS)

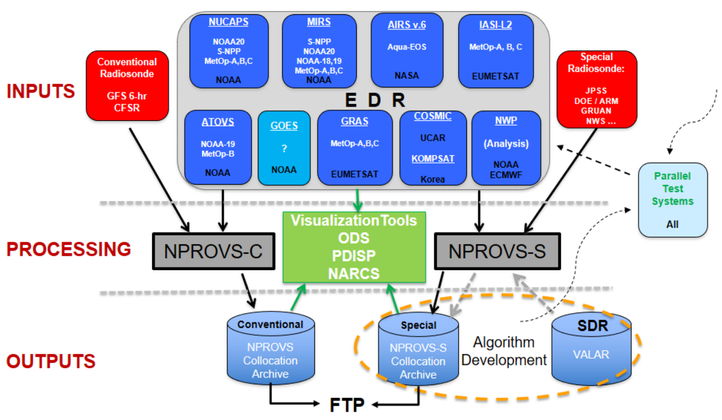

Funded by JPSS Cal/Val Program
(Enterprise Assessment at STAR !)

NPROVS provides routine compilation of collocated radiosondes, numerical weather prediction model and operational satellite atmospheric temperature and water vapor sounding profiles derived from multiple satellite platforms (NOAA, NASA, EUMETSAT …); a single "closest" sounding from each platform (and NWP) is collocated to a given radiosonde within 6 hr and 150 km.

Case studies span from within CONUS, for example, Atmospheric River (US West Coast) and Pre-convective (Great Plains USA) environments to Tropical Storm (Barbados), Special NOAA AEROSE (Saharan Air Layer) trans-Atlantic campaigns and the Brush Fires in Australia.

JPSS - HWTB

Week	Case #	Date	Weather Region	Product	Success/ Failed	Details
2	3	5/10 2018	Eastern Wyoming	Mid-Level Moisture	Success	• NUCAPS sounding captured higher moisture levels better than NAM12 • NUCAPS helped forecaster diagnose storm mode and indicating where the mixing is occurring ahead front
	4	5//9 2018	South Central Illinois	CAPE	Failed	• NUCAPS CAPE was very high, however severe storms did not occur • CAPE anomaly sounding near Newton, IL
3	5	5/14 2017	Texas panhandle up to Kansas City	CAPE	Success	• NUCAPS CAPE closer to high resolution guidance than AllSky CAPE
	6	5/17 2018	Amarillo, TX	Lapse Rates	Failed	• Gridded NUCAPS lapse rates were not steep enough compared to models

JPSS hazardous Weather test bed (HWTB) offers opportunities for forecast users and NUCAPS providers to interact on case studies of interest; Case Study 6, Amarillo Texas, May 17, 2018 is summarized below

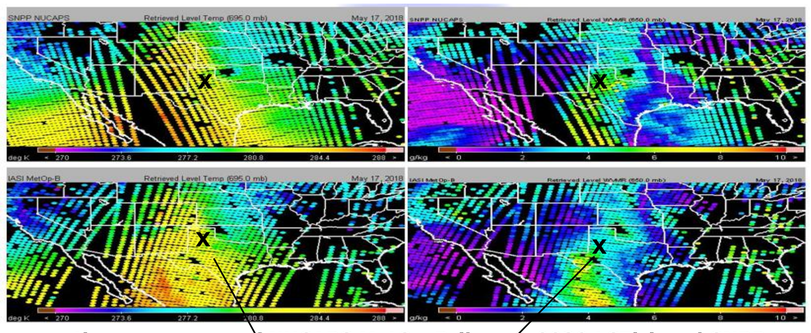

Consecutive overpasses of NUCAPS MetOp-B (lower, 0930 LST)) and SNPP (upper, 1330 LST) for temperature (left) and H2O vapor (right) confirm the advection of warm moist air northeastward toward Amarillo (X) and heightened potential for convection.

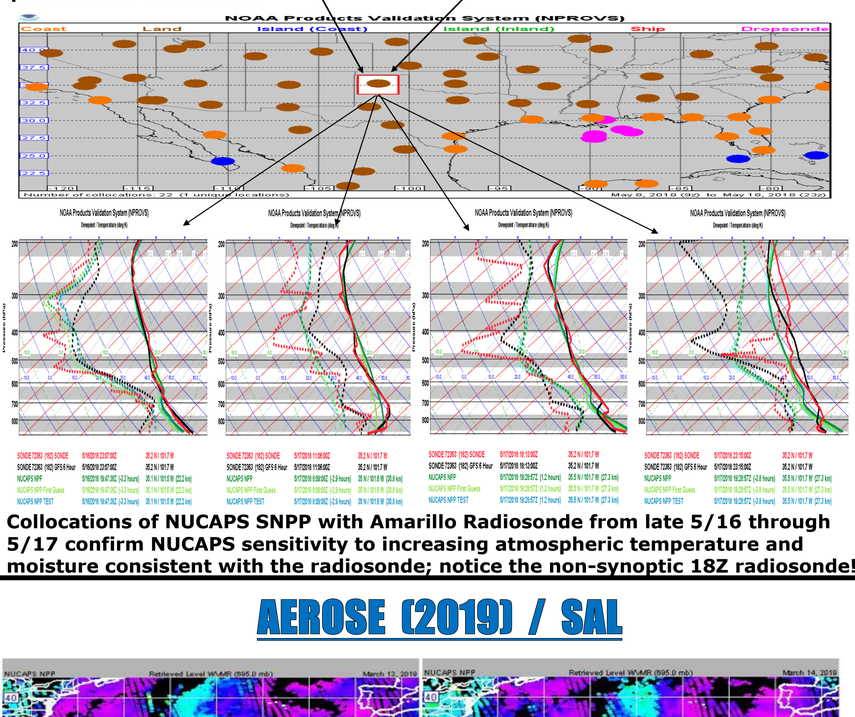

Collocations of NUCAPS SNPP with Amarillo Radiosonde from late 5/16 through 5/17 confirm NUCAPS sensitivity to increasing atmospheric temperature and moisture consistent with the radiosonde; notice the non-synoptic 18Z radiosonde!

Hurricane Dorian

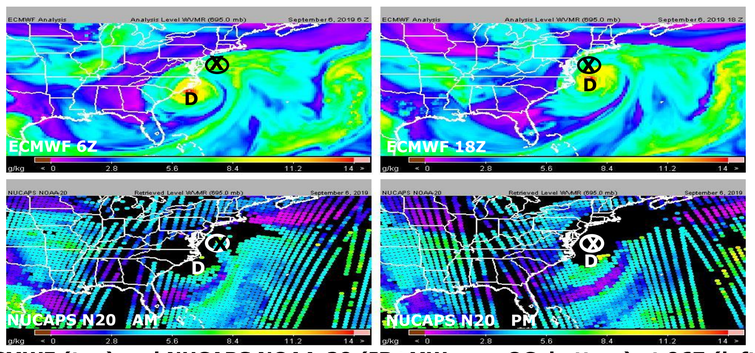

ECMWF (top) and NUCAPS NOAA-20 (IR+MW pass QC, bottom) at 06Z (left) and 18Z (right) on Sept. 6, 2019; "D" indicates Dorian's center and "X" the target location for NUCAPS

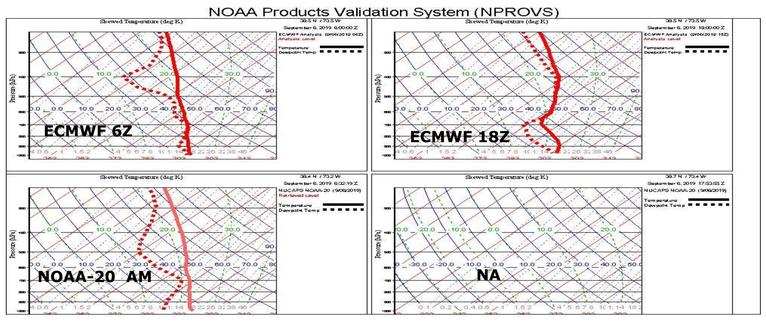

ECMWF (top) and NUCAPS (IR+MW pass QC, bottom) at 06Z (left) and 18Z (right) on Sept. 6, 2019 at locations 'X"; NUCAPS in good agreement at 06Z in the path of Dorian but not available at 18Z in vicinity of eye-wall

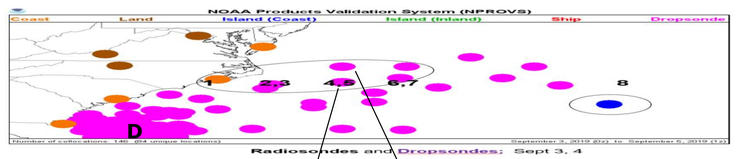

Special NOAA dropsondes on September 3 and 4 include subsets in Dorians projected path; cases of interest in the context of NUCAPS soundings are circled

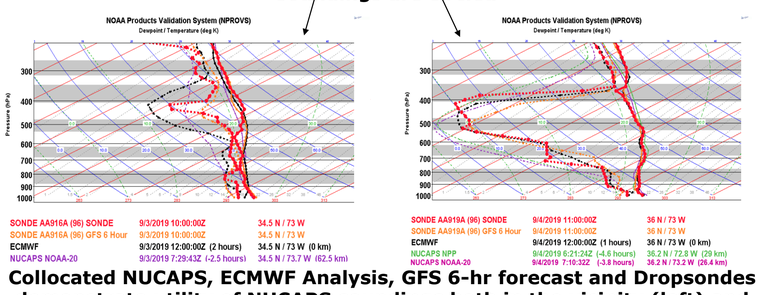

Collocated NUCAPS, ECMWF Analysis, GFS 6-hr forecast and Dropsondes demonstrate utility of NUCAPS soundings both in the vicinity (left) and further out ahead of Dorian (right).

Atmospheric River

AWIPS-2 El-Nino Rapid Response 2016

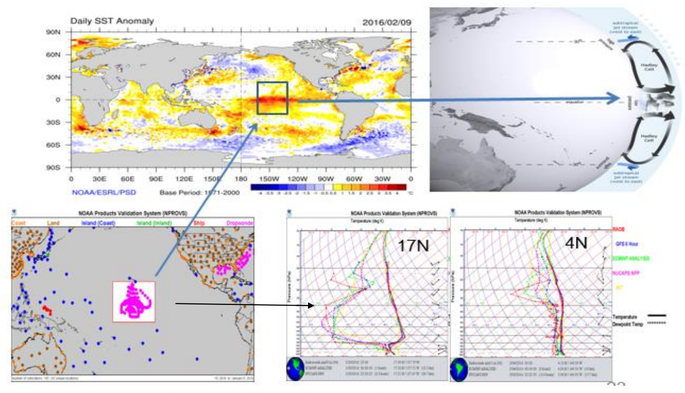

NUCAPS vertical profiles (lower right) compared to special targeted radiosondes (low left) captures circulation (Hadley cell) regimes (top) of the central tropical/sub-tropical region

January 2018

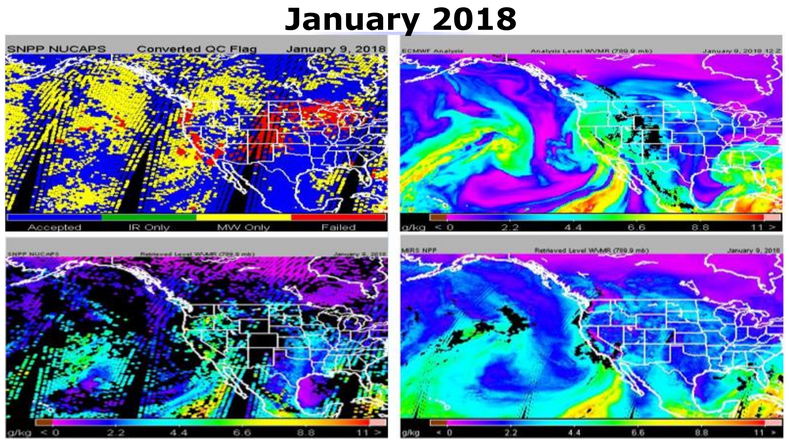

NUCAPS (v5, low left) 800 hPa Atmospheric River moisture pattern compares favorably to ECMWF Analysis (up right) and NOAA operational MiRS (low right). The upper left denotes successful NUCAPS IR+MW (blue) that are plotted below; *yellow and red are regions where IR+MW failed.*

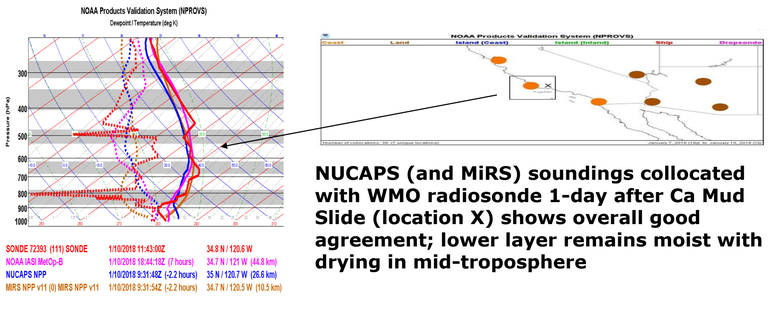

NUCAPS (and MiRS) soundings collocated with WMO radiosonde 1-day after Ca Mud Slide (location X) shows overall good agreement; lower layer remains moist with drying in mid-troposphere

AEROSE (2019) / SAL

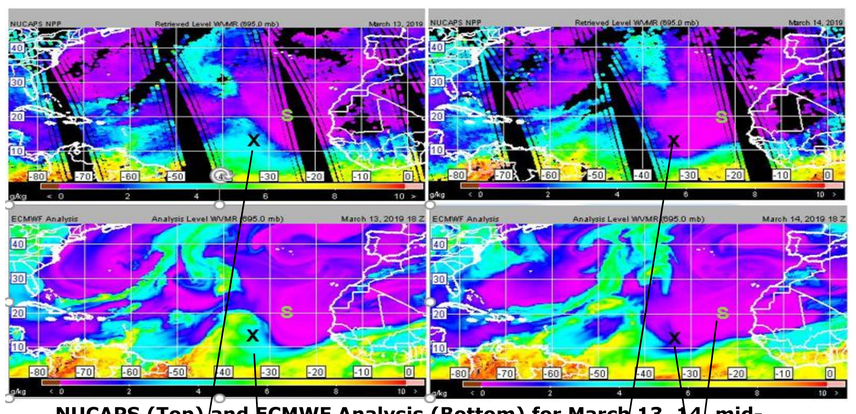

NUCAPS (Top) and ECMWF Analysis (Bottom) for March 13, 14, mid-afternoon; 695 hPa H20 vapor: "X" Target; "S" ship

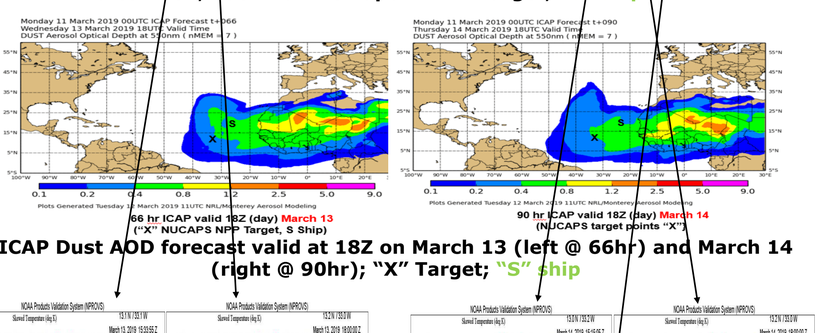

ICAP Dust AOD forecast valid at 18Z on March 13 (left @ 66hr) and March 14 (right @ 90hr); "X" Target; "S" ship

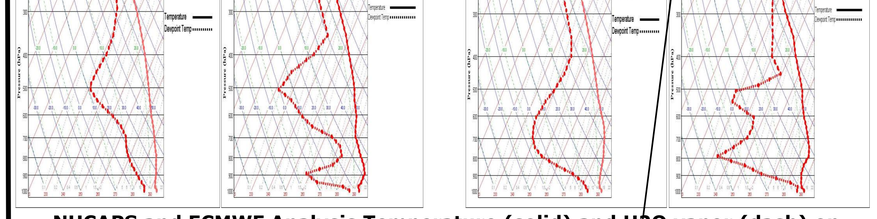

NUCAPS and ECMWF Analysis Temperature (solid) and H2O vapor (dash) on March 13 (left) and March 14 (right) at the location "X"; penetration into SAL manifested in enhanced dry subsidence layer vicinity of 700 hPa in both NUCAPS and ECMWF

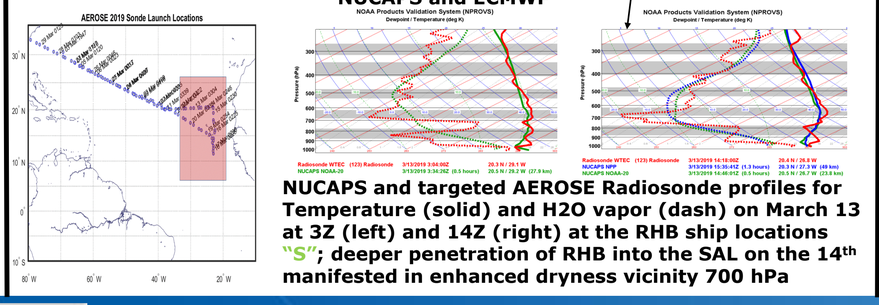

NUCAPS and targeted AEROSE Radiosonde profiles for Temperature (solid) and H2O vapor (dash) on March 13 at 3Z (left) and 14Z (right) at the RHB ship locations "S"; deeper penetration of RHB into the SAL on the 14th manifested in enhanced dryness vicinity 700 hPa

Australia Brush Fires

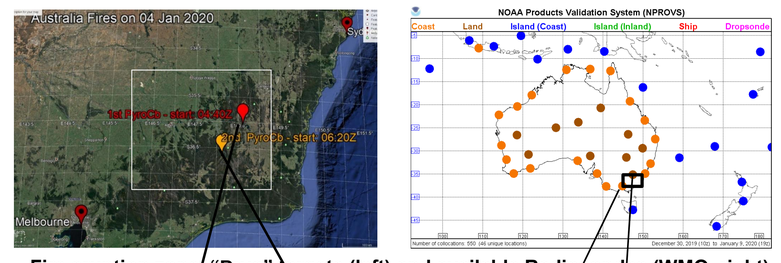

Fire eruption zone, "Pryo" targets (left) and available Radiosondes (WMO, right) collocated to NUCAPS soundings on January 4, 2020

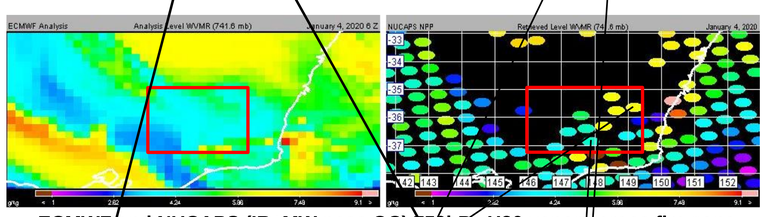

ECMWF and NUCAPS (IR+MW pass QC) 750hPa H20 vapor across fire zone corresponding to NPP afternoon overpass (06Z) on January 4, 2020

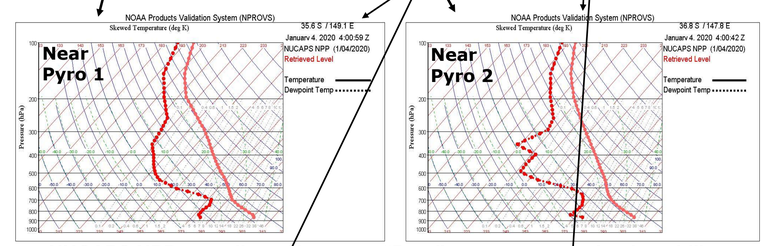

NUCAPS NPP soundings closest to "Pyro" targets suggesting instability promoting fire expansion

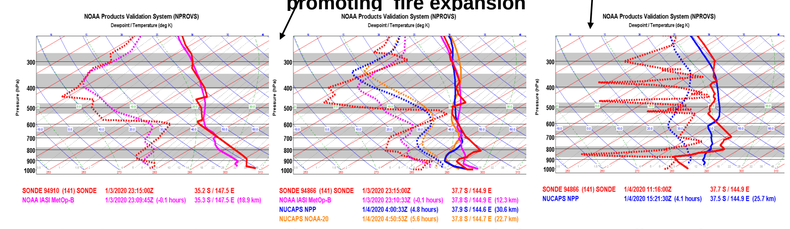

NUCAPS NOAA-20, NPP and/or MetOp-B (pass QC) closest to Radiosondes near the targets zone and 06Z on Jan 4, 2020;

References

- Reale, A., B. Sun, F. Tilley, and M. Pettey, 2012: The NOAA Products Validation System (NPROVS). Journal of Atmospheric and Oceanic Technology. 29, DOI:10.1175/JTECH-D-11-00072.1.
- Nalli, N., and Coauthors, 2011: Multi-year observations of the tropical Atlantic atmosphere: Multidisciplinary applications of the NOAA Aerosols and Ocean Science Expeditions(AEROSE). Bull. Amer. Meteor. Soc., 92, 765–789, doi:10.1175/2011BAMS2997.1.

STAR Center for Satellite Applications and Research

Poster 30, JPSS / GOESR Proving Ground Risk Reduction Summit
24-28 February 2020, National Center for Weather and Climate Prediction (NCWCP)
College Park, MD
(*corresponding author: Tony.reale@noaa.gov*)

Adapting Satellite Soundings for Operational Forecasting within the Hazardous Weather Testbed

Rebekah Esmaili, Nadia Smith, Chris Barnet
Science and Technology Corporation, Columbia, Maryland USA

NUCAPS soundings

- Supplement radiosondes with wide swaths of soundings from JPSS satellites
- Retrieve vertical temperature, moisture, and trace gases
- Calculate stability indices
- Are available multiple times during the day
- Are model-independent
- Available in real-time through direct broadcast

https://weather.msfc.nasa.gov/nucaps

NUCAPS evaluated by NWS forecasters in the Hazardous Weather Testbed (HWT) since 2015

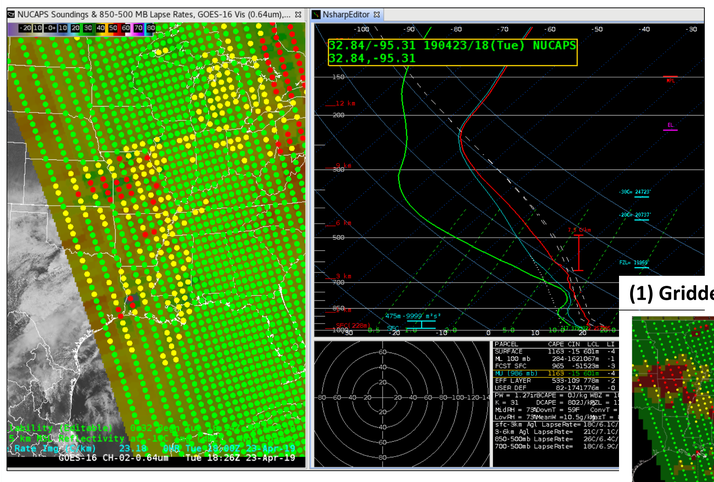

HWT Goals
- Train forecasters in new products/technology
- Evaluate new products ahead of their release in operations

- Left: NUCAPS in AWIPS, soundings available in NSHARP display
- Incremental product development from forecasters feedback:

(1) Gridded NUCAPS: Plan-view/cross-section displays

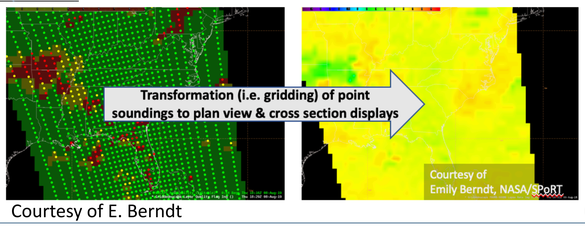

Courtesy of E. Berndt

(2) Modified NUCAPS w/Boundary layer modification w/surface observations and GOES

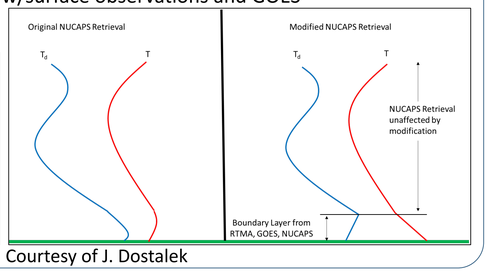

Courtesy of J. Dostalek

Recommendations to Product Developers for Research to Operations:

Have a clear understanding of user needs

Developer needs

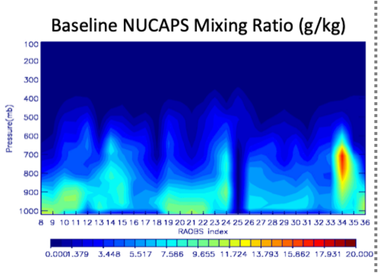

How a product developer wants to see a cross-section

User needs

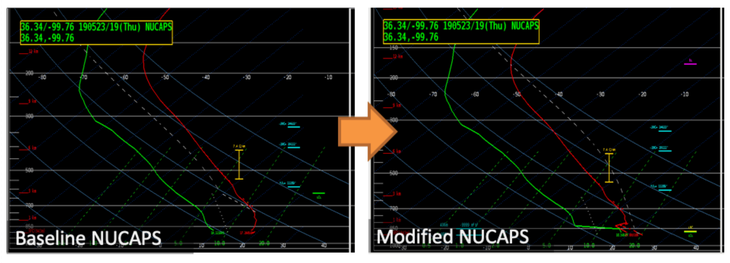

How a forecaster wants to see a cross-section

Adjusting NUCAPS automatically following forecaster feedback

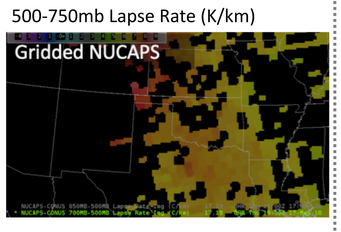

Developers like looking at QC'd data to ensure they "meet requirements"

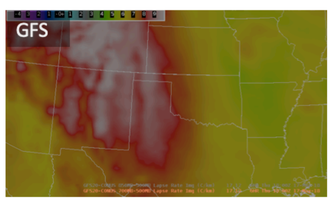

But forecasters prefer to see data filled in, even if the observations have errors.

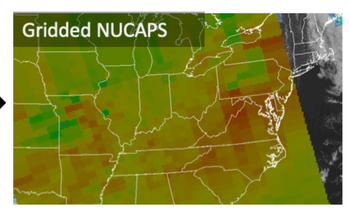

Development of gridded NUCAPS following forecaster feedback.

Surveys should contain a mixture of quantitative and qualitative questions

How often would you use NUCAPS in the future?
60% of HWT 2019 responses: "sometimes", "usually", or "always"

How can NUCAPS products be more useful in the future?
50% of respondents indicated more satellite overpasses would be helpful

Ranked as important/very important:
1. Better boundary layer representation (and by extension, CAPE values)
2. More observations (e.g. having two satellites available in AWIPS)

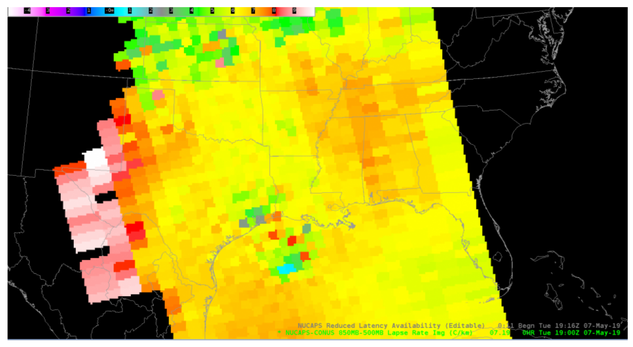

As an operational forecaster, I like to compare model output, real-time obs, and any additional derived data. ***This image from the NUCAPES H85-H5 Lapse Rate can potentially help boost one's confidence in particular synoptic situations.*** For example, suppose you were expecting a dryline to emerge east across W Texas, but guidance indicated otherwise and sfc METARS were unavailable, ***using the NUCAPS Lapse Rate products can help determine the location of the dryline (for this particular setup). In this image, values reflect the drier air advancing east leading to steeper lapse rates***.

-- HWT Forecaster, 2019

Encourage data combination, sophisticated analysis to identify future work

Successes

Phenomena
- Freezing levels
- Supercell development along cold fronts
- CAPE gradient head of MCS tracks
- Captured low level caps
- Dryline convection

Situational Awareness
- Quickly got orientation at the beginning of shift
- Modified soundings and gridded fields provided insight into gradients.

Future Work

Not enough data
- Useful for evaluating mid-level environments but a single LEO satellite availability is too sparse

Usability and missing data within retrieval
- Convection already initiated, too many "data holes" from low quality or missing retrievals

Boundary layer
- Cases where CAPE values, the surface inversion, and drier mixed layer was inconsistent with radiosondes

Strengths, limitations communicated through training

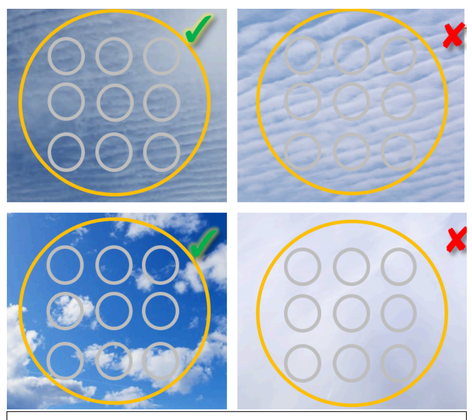

O NUCAPS retrieval footprint
o CrIS spectral measurement area

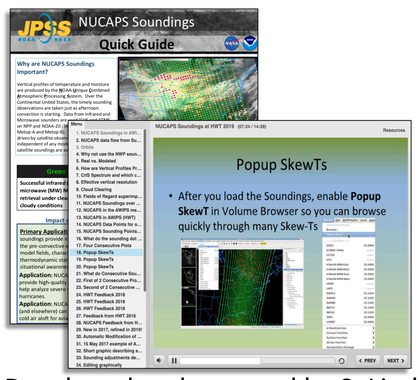

Developed and narrated by S. Lindstrom

Strengths
- Provides soundings between radiosonde launches
- Provides a dense network where conventional observations are lacking
- NUCAPS can make retrievals over *clear and partly cloudy* scenes (top left)

Limitations
- Challenging to retrieve fine boundary layer structure
- NUCAPS fails in precipitating scenes or uniform cloud decks, so **NUCAPS is less helpful once convection initiates**

Training provided via Vlab, online videos, quick guides (bottom left)

Acknowledgements: Work funded by the NOAA Joint Polar Satellite System Proving Ground/Risk Reduction Program, directed by Dr. Mitch Goldberg.

COSMIC-2 Data for Atmospheric Soundings

Erin Lynch[1], Shu-peng Ho[2], Xinjia Zhou[3],Changyong Cao[2]

1: ESSIC/CISESS, University of Maryland, College Park
2: NOAA/NESDIS/STAR
3: GST, Inc.

ABSTRACT

FORMOSAT-7/COSMIC-2 is a joint mission between the United States (NOAA,USAF) and Taiwan (NSPO) to provide operational radio occultation (RO) data. A follow on to the successful FORMSAT-3/ COSMIC mission, COSMIC-2 observations are vital to numerical weather prediction (NWP) and other science applications. In addition to temperature and moisture profiles for the neutral atmosphere, COSMIC-2 also provides total electron content profiles for the ionosphere as well as ionospheric scintillation indices for space weather applications.

The six COSMIC-2 satellites launched on June 24, 2019. Following spacecraft and payload checkout, the RO receivers on-board each satellite have been collecting atmospheric soundings. COSMIC-2 data is processed by UCAR/CDAAC and provided to both NWP centers and science users. After an intensive calibration and validation period, the quality of the data was deemed to be provisional in December 2019. The initial operational capability of the COSMIC-2 neutral atmosphere data was reached in February of 2020.

Figure 1. The launch of COSMIC-2 as part of STP-2 on-board a SpaceX Falcon Heavy, Image credit: NOAA and SpaceX.

BACKGROUND

Radio Occultation (RO) is a limb sounding technique that measures atmospheric profiles by making use of the signals transmitted by Global Navigation Satellite System (GNSS) satellites. These signals are refracted by the Earth's atmosphere by varying angles due to density gradients. An occultation occurs when a GNSS satellite is observed rising or setting behind the disk of the Earth from the perspective of a receiving satellite in low earth orbit (LEO). Receivers on-board the six COSMIC-2 satellites capture the radio signals and record a series of the time delay introduced by the bent path at various altitudes. From the degree of bending, temperature and moisture profiles of the atmosphere can be retrieved.

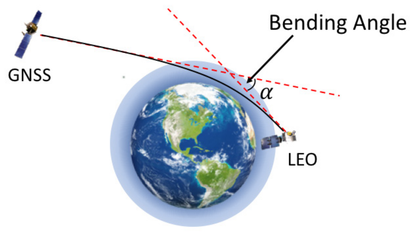

Figure 2. A schematic depicting the geometry of an occultation and the bending angle that is derived.

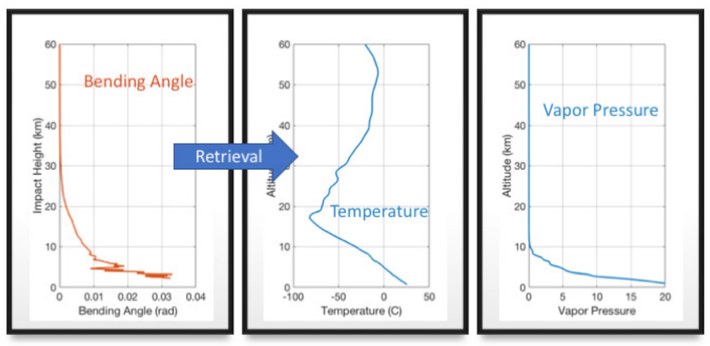

Figure 3. From the bending angle profile, temperature and moisture profiles can be retrieved.

TGRS: NEXT GENERATION RO RECEIVER

The primary COSMIC-2 payload is the Tri-GNSS Radio-occultation System (TGRS) instrument. The TGRS includes a number of technological advancements over the heritage receiver on-board COSMIC-1, including:

- The ability to receive new, modernized GNSS signals from multiple GNSS constellations including GPS and GLONASS;
- The ability to update both software and firmware to improve data quality and acquisition;
- Multiple digital beam steering to simultaneously direct multiple beams for high SNR especially at low and high atmospheric altitudes and maximized for each satellite tracked individually ;
- Multi-lag processing allowing for use of multiple range and Doppler models to more reliably capture rising occultations;
- Time delayed processing that stores RO data so that it can be reprocessed if a better model can be produced;
- Blueshift Algorithm allowing for tracking when SNR is low, improving both lower atmosphere and rising occultations.

COSMIC-2 CONSTELLATION

Figure 4. A schematic of the low inclination orbits of the six COSMIC-2 satellites. Image courtesy of NSPO.

The final COSMIC-2 mission constellation will put the six satellites into low inclination LEO orbits with altitudes of about 550 km. The Walker 6/6/4 constellation will allow for as much uniformity in geographic distribution of occultations as possible. The low inclination orbits result occultations between 45° North and 45° South where cyclogenesis occurs and the improved data collection techniques will help to capture the highly variable moisture structure. Nine ground stations allow for data latency of less than 45 minutes.

The satellites were launched into parking orbits at 720km. Each is lowered one at a time into the mission orbit to allow for proper spacing and phasing. At this time, two of the six satellites are in their mission orbits, and a third is being lowered. The final mission constellation will be realized in February 2021.

References:
1. Weiss, J.P. & Schreiner, W.S. (December 10, 2020) FORMOSAT-7/COSMIC-2 Neutral Atmosphere Provisional Data Release 1. Retreived from https://data.cosmic.ucar.edu/gnss-ro/cosmic2/provisional/F7C2_NA_Provisional_Data_Release_1_Memo.pdf
2. Schreiner, W. S., et al.(2020). COSMIC-2 radio occultationconstellation: First results.GeophysicalResearch Letters,47, e2019GL086841. https://do.rg/10.1029/2019GL086841
3: Ho, Shu-peng, Xinjia Zhou, Stanislav Kireev, Loknath Adhikari, 2019b, NESDIS RO Science Studies and Quality Assurance through the STAR Integrated Cal/Val System: Initial Validation of COSMIC2 Data, IROWG Workshop, https://www.romsaf.org/romsaf-irowg-2019/en/open/1570202501.3acc71ecd45aa34b643a194c5d451c98.pdf/Ho__2019_09_IROWG_ICVS_C2_talk_BenHo.pdf

PROVISIONAL DATA RELEASE

Following an intensive commissioning and calibration/validation period, the COSMIC-2 data were declared provisional on December 10, 2020. The data processed by UCAR/CDAAC is publicly available at the following website:

https://data.cosmic.ucar.edu/gnss-ro/cosmic2/

• > 4000 Occultations Per Day

By receiving signals from both GPS and GLONASS satellites, COSMIC-2 is able to capture upwards of 4000 occultations per day.

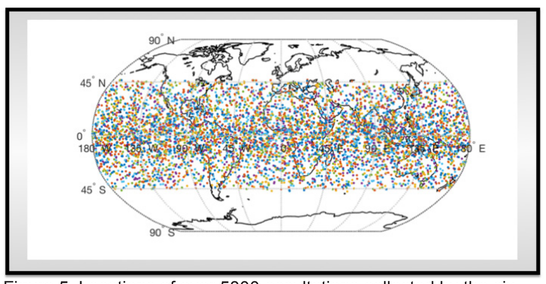

Figure 5. Locations of over 5800 occultations collected by the six COSMIC-2 satellites on Feb. 5, 2019.

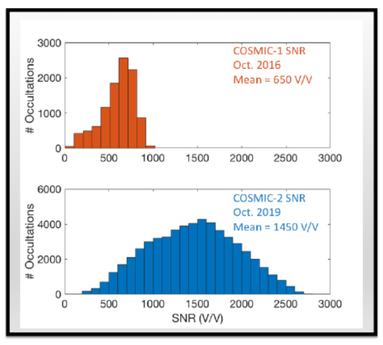

Figure 6. The distributions of the L1 SNR at 80km for occultations collected by COSMIC-1 in October 2016 (top panel) and similarly, for those collected by COSMIC-2 in October 2019 (bottom panel).

• High Signal to Noise Ratio (SNR)

COSMIC-2 has by far the highest SNR of any RO mission. The impacts of SNR on data quality and penetration depth are active areas of study, as are the best ways to utilize the enhanced measurement capability.

• Deep Profile Penetration

Over 80% of COSMIC-2 profiles penetrate below 1.2km. Tropospheric ducting where super-refractivity occurs can be detected (see Schreiner et al. 2020).

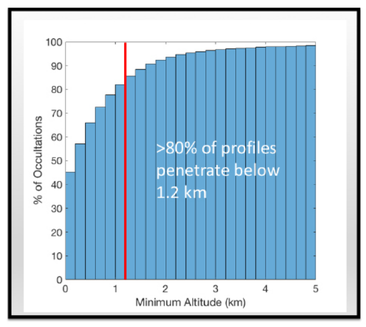

Figure 7. The cumulative distribution of the minimum altitude of occultations from October 2019.

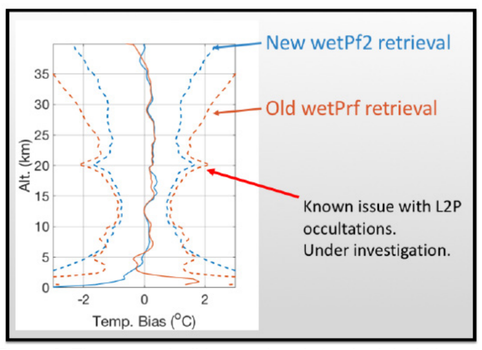

Figure 8. The means (solid curves) and standard deviations (dashed curves) of the old wetPrf retrieved (orange) and new wetPf2 retrieved temperatures compared to ECMWF forecasts.

• New Temperature and Moisture Retrieval Algorithm

The new 1D-VAR retrieval algorithm was implemented by UCAR/CDAAC for the COSMIC-2 data. This retrieval utilizes a Control-Variable Transform formulation and variational Abel transforms for both the observation operator an optimization of the bending angle. The wetPf2 profiles offer higher vertical resolution than the previous wetPrf version.

STAR RO ICVS

STAR has extended the monitoring capabilities of the Integrated Calibration and Validation system (ICVS) to radio occultation data from multiple missions including COSMIC-2. The ICVS is a web-based system that supports instrument performance monitoring, inter-comparisons with other independent measurements, and data assimilation in collaboration with data users. Capabilities for RO include:

- Near real time and long-term monitoring of instrument status and performance;
- Near real time and long-term monitoring of data product quality;
- Anomaly detection and diagnosis;
- Assurance of the integrity of the climate data records;
- Routine comparisons with other satellite observations and retrievals, e.g. MW and IR;
- Routine comparisons of profiles with those from Radiosondes;
- Dynamic web interface with many capabilities;
- Long-term monitoring of RO parameters.

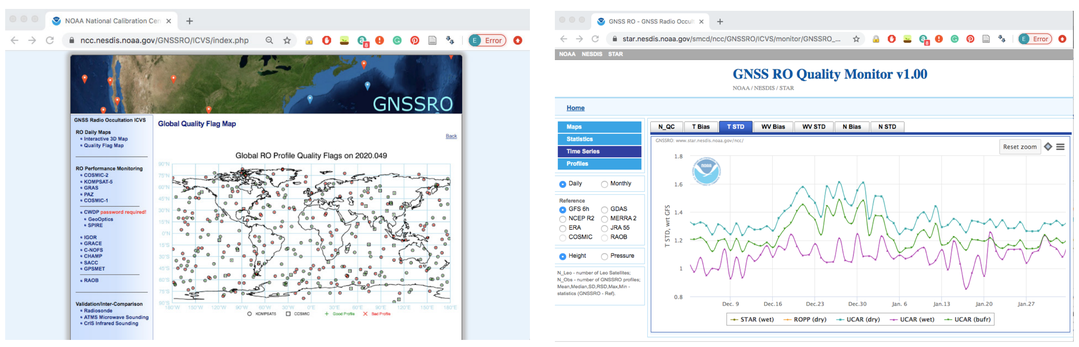

Figure 9. Screen-captures of the STAR RO ICVS website. Many RO missions are monitored, including COSMIC, MetOp GRAS, Commercial Data providers (not public), and COSMIC-2. The right panel shows trending of the standard deviation of temperature compared to GFS forecasts for COSMIC-2.

COSMIC-2 Data have reached Provisional Maturity and are suitable for operational use in Numerical Weather Prediction (NWP) and other science applications.

Howard University Beltsville Campus (HUBC): Involvement, Contribution, and Impact in Atmospheric Sciences Research

Adrian Flores[1], Ricardo Sakai[1], Belay Demoz[2], Everette Joseph[3], Vernon Morris[1], David Whiteman[1], Demetrius Venable[1*]

[1]*Howard University, Washington D.C., USA*

[2]*Joint Center for Earth Systems Technology/University of Maryland, Baltimore County, Baltimore, MD,USA*

[3]*National Center for Atmospheric Research, CO, USA*

1. Introduction:

Howard University, in partnership with NOAA, NASA, and several other federal agencies, has built a rigorous research program in atmospheric sciences at the Howard University Beltsville Campus (HUBC). Atmospheric sciences research at HUBC is helping the nation and the international community to understand and develop innovative strategies to improve weather forecasts, effectively mitigate climate change, and better understand and predict air quality.

2. Site and Instrumentation

HUBC is located approximately 12 miles northeast of downtown Washington, DC, on 110 acres in suburban Maryland (figure 1). The campus is in a suburban/rural setting. HUBC contains minimal development with not more than 5 percent of the land area occupied by building structures, making it an ideal environment for studying a range of surface-atmospheric interaction processes.

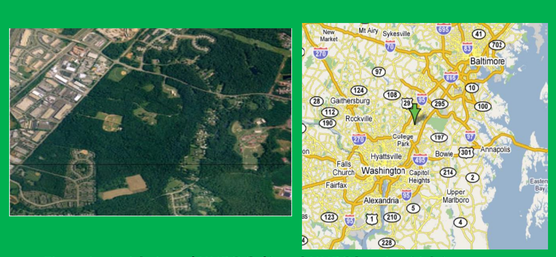

Figure 1: Aerial view of HUBC (left), and HUBC location (right).

A comprehensive set of instruments have been deployed including water vapor Raman lidar, micro wave radiometer (MWR), upper air sounding systems, spectral and broadband radiometers, 31 m flux and meteorological tower, gas analyzers and particle samplers, as well as low-cost sensors (figure 2). These instruments are calibrated to international standards, and their measurements properly archived and disseminated for a variety of scientific research activities and applications.

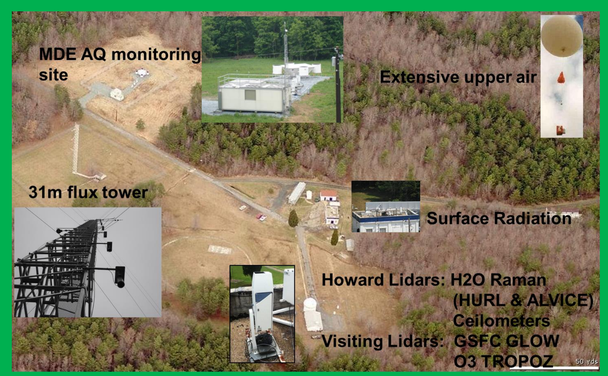

Figure 2: Aerial view with locations of some of the major observing systems at HUBC. Not shown is the main building on the north side of the site that houses ALVICE, Micro-wave Radiometer, laboratories and office space in 13600 Sq. Ft.

3. Air Quality:

Atmospheric pollutants such as ozone and fine particle matter (PM) are recognized as harmful substances to human health. HUBC in partnership with Maryland Department of the Environment (MDE) has been monitoring trace gases and aerosols (PM) since 2004. Since then, HUBC has been launching ozonesondes during high ozone episodes, and it hosts one of the most complete air quality stations in the MDE network (figure 2). Figure 3 shows a case study when HUBC lidar (ceilometer) detected smoke plume from fires originated in Canada, this smoke provoked a widespread high ozone event over the mid-Atlantic on June 11, 2015.

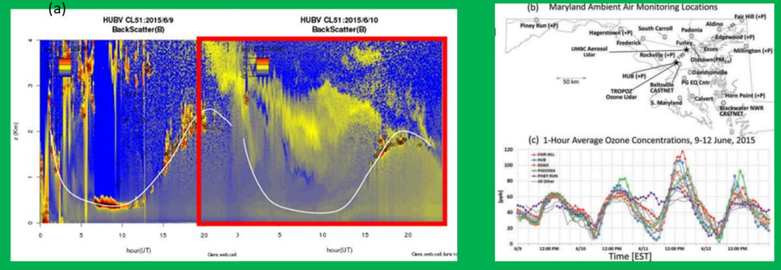

Figure 3: (a) CL51 ceilometer backscatter time series on June 9 and 10, 2015 at HU-Beltsville, MD. The planetary boundary layer height is shown as a white curve. Smoke plume is associated with moderate high backscatter values (bright yellow) on 6/9 20:00 UT till 6/10, 10:00 UT. (b) Location of the Maryland Department of Environment air quality stations, (c) and the hourly ozone concentration observed during the smoke plume event (from Dreessen et al, 2016).

4. Climate: GRUAN Network & Satellite

Established in 2008, under World Meteorological Organization GCOS (Global Climate Observational System) reference upper-air observing network (GRUAN – figure 4a) will provide long-term, high-quality climate data records from the surface, through the troposphere, and into the stratosphere. Howard University is a GRUAN site in collaboration with NWS, NASA, NOAA/JPSS/STAR group, and the only academic intuition in the GRUAN network.

A method has been developed selecting a single satellite retrieval profile using the atmospheric variability of scalars (e.g. water vapor and temperature) determined by in situ ground based remote sensing instruments for site state best estimate (SASBE). Satellite products from NOAA Unique Combined Atmospheric Processing System (NUCAPS) are collocated and compared with HUBC site results (figure 4b). NUCAPS profiles are within a 20% agreement of the radiosonde/HURL for water vapor mixing ratio values, with a dry bias of 3 g/kg in the lower troposphere (figure 4c).

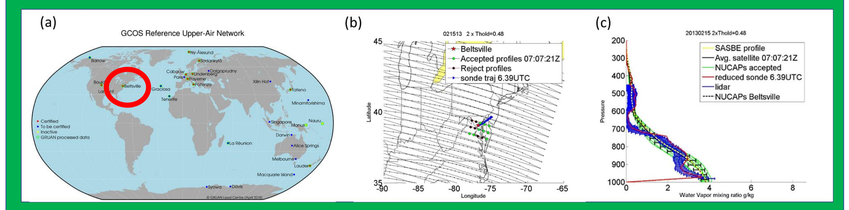

Figure 4: (a) GRUAN network locations. HUBC is highlighted in the red circle. (b) Lines represent the SUOMI NPP satellite trajectories , red and green dots are the profile locations of the NUCAPS products (red rejected profiles, green accepted profiles), blue dots are the radidosonde trajectory. (c) Site Atmospheric State Best Estimate using Raman Lidar (HURL), radiosonde, and NUCAPS products.

5. Weather:

Howard University with conjunction with University Maryland Baltimore County and Morgan State University are developing an upper-air meteorological network for nowcasting (short term weather forecast – 2 to 6 hours).

One motivation was the derecho system that passed through the region on June 29, 2012. This derecho left a path of destruction stretching more than 600 miles from the Upper Midwest to the Mid-Atlantic coast (Figure 5a). This resulted in massive tree damage and power outages leaving nearly 4 million residents without power, extensive damage to transmission lines, power poles, and substations, and left 500,000 without power for nearly a week. For this event, observations from the MWR convey atmospheric destabilization as early as 15 hours in advance of the approaching storm in the Mid-Atlantic (figure 5b). This coupled with record heating at the surface resulted in abnormally high convective instability indices beginning near 15Z (10 am), more than 10 hours in advance of the derecho (10 pm, figure 5c). On the other hand, forecasters were unaware of the exact state of the atmosphere until the analysis of the 00Z radiosonde launch (8 pm LT).

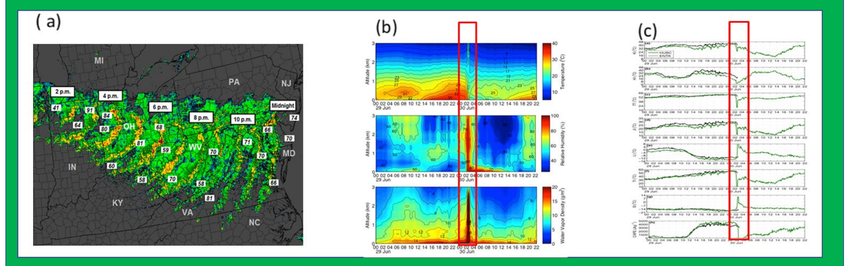

Figure 5:: (a) Radar image composite summary of derecho with highest reported wind gusts (*Furgione*, 2013). (b) MWR contoured observations of (top) temperature, (middle) relative humidity, (bottom) and water vapor density in the lower troposphere during the derecho episode (highlighted in the red rectangle) (c) MWR derived instability indices from top to bottom of KI, HI, TT, JI, LI, TI, SI, and CAPE, derecho passage highlighted in red rectangle.

6. OWLETS-2:

The Ozone Water-Land Environmental Transition Study-2 (OWLETS-2) is a follow-on study to better understand the behavior of ozone and related trace gases across the water land transition zone in the upper portion of the Chesapeake Bay. OWLETS-2 used a unique combination of measurements during summer 2018 (June 6 to July 6) to more fully characterize the behavior of ozone in the Baltimore region. This included two ozone lidar systems, multiple wind and aerosol lidars, ozonesondes, UAVs, research aircraft, and a host of in-situ measurements at the University of Maryland Baltimore County (UMBC), Hart-Miller island (HMI) and HUBC to obtain measurements simultaneously over land and water (Figure 6).

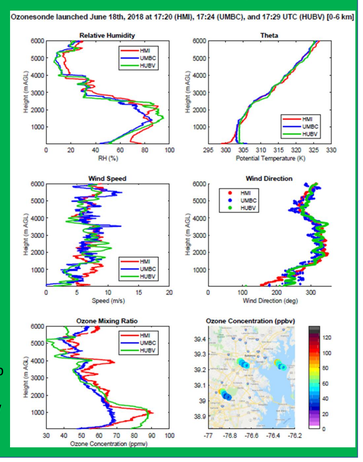

Figure 6 represents the triple coordinated launch for HUBC, UMBC, and HMI on June 18, 2018, at approximately 17:20 UTC with initial wind blowing from the south. There is a deep layer of elevated ozone over water and over HUBC from 500-1500 m. At its peak at around 1000 m, there is over a 20 ppb difference between UMBC and the other two sites. Boundary layer heights over land look to be about 1200-1500 m. Below 300 m, ozone values sharply decrease from 70 ppb to about 50-55 ppb over HMI and UMBC, but not at HUBC.